Study of polarized proton diffraction dissociation in the reaction $p_{\uparrow}p \to p\pi^+\pi^-p$ at 11.75 GeV/c

J. P. Finley,* A. B. Wicklund, M. W. Arenton,† D. S. Ayres, R. Diebold, S. L. Kramer, E. N. May, L. J. Nodulman, and J. R. Sauer‡
Argonne National Laboratory, 9700 So. Cass Ave., Argonne, Illinois 60439
(Received 16 December 1985)

We present angular distributions and, for the first time, single-spin correlations in the diffraction-dissociation reaction $p_{\uparrow}p \to p\pi^+\pi^-p$, for small momentum transfers between the polarized beam and the $(p\pi^+\pi^-)$ system, at 11.75 GeV/c. The only structures seen in our 2×10^6-event sample turn out to be the well-known threshold enhancement in $\Delta\pi$ and the $N(1700)$, which appears to involve both $\Delta\pi$ and $N(1520)\pi$. The production process exhibits a slope-mass correlation and patterns of helicity nonconservation seen in higher-energy diffractive processes. We also see evidence for a complex helicity structure in the spin correlations. We show that the threshold enhancement is unambiguously S wave in character, while the $N(1700)$ appears to be a mix of states. The overall similarities between our data and those at higher energies, together with the rich structures contained in the angular-distribution correlations (we measure 315 joint moments in each mass and t bin), make our data base highly relevant for theoretical analysis of exclusive diffraction.

I. INTRODUCTION

We present results based on a sample of 1 930 000 events of the reaction

$$p_{\uparrow}p \to p\pi^+\pi^-p \tag{1}$$

at 11.75 GeV/c, obtained with the effective-mass spectrometer using the polarized proton beam from the Argonne Zero Gradient Synchrotron (ZGS). Some polarization results are also presented for a smaller sample of 6-GeV/c data.

Diffraction-dissociation (DD) processes such as reaction (1) are probably the only exclusive inelastic reactions that can be studied at ultrahigh collider energies. Moreover, the main features of these DD processes appear to be essentially independent of energy. Thus, it seems plausible that high-statistics data with polarized beams at a relatively low energy can complement the relatively-low-statistics, unpolarized data available thus far from colliding-beam experiments, hence the motivation for this study. The DD processes involving $N \to N\pi$ (Refs. 1–8) and $N \to N\pi\pi$ (Refs. 4, 7, and 9–26) have been studied with $\pi^{\pm}$, $K^{\pm}$, n, p, and $\bar{p}$ probes over a wide range of energies. The systematic features which appear to be common to these reactions at all energies include strong production of an enhancement near threshold, which appears to be predominantly S wave; production of a secondary enhancement around 1.7 GeV which is likely to involve several spin-parity states; a strong slope-mass correlation, and correlation of the t slopes with the angular distributions; a break in the t distributions at low mass around $-t \simeq 0.3$ GeV^2; and marked helicity-flip effects in both s and t channels. Some of these features follow naturally from π-exchange Deck models,[27,28] while others require baryon exchange, absorptive corrections, etc.[29–32] Our data display these features rather clearly.

Since only two enhancements (at threshold and at 1.7 GeV) are prominent in these reactions, it is clear that partial-wave analysis (PWA) is needed to resolve spectroscopic issues. Several such analyses have been performed on the $p\pi^+\pi^-$ system,[21–26] but the statistical accuracy has been rather limited, as compared with analyses of the formation reactions[33–37]

$$\pi N \to \pi\pi N\ . \tag{2}$$

It is clear that the production reactions have not revealed the rich structure of baryon resonances which have been identified in the formation channels, possibly because the Deck-effect backgrounds obscure the resonances in production reactions. With our higher statistics we have carried out spin-parity analysis on the $p\pi^+\pi^-$ system; in particular, we used the polarization information, as distinct from the isobar-model technique, to help determine the partial-wave phases. We remark that the production reactions are a natural place to search for resonances which decouple from πN and from the formation process, such as have been proposed by Isgur, Karl, and Koniuk.[38] It is clear from our data that such resonances, if they are produced in reaction (1), are subtle effects and do not cause clear peaks in the mass spectra. In this paper we do not analyze in detail the high-mass region where these states are expected to lie; we focus instead on the mass region below 1.8 GeV and on the $\Delta\pi$ channel, in order to better understand the dominant features of the process.

We organize our report as follows. Section II summarizes the experiment and the analysis. Section III examines some of the isobar contributions which compete with the $\Delta^{++}\pi^-$ final state. Section IV presents the t dependence of the angular distributions and polarizations, and Sec. V describes the mass dependence and the partial-wave analysis. A summary is given in Sec. VI, and the Appendix documents the relationship between spin correlations and partial-wave amplitudes. Whereas Sec. III relies mainly on raw mass spectra, Secs. IV and V utilize the

acceptance-corrected joint moments of the $\Delta^{++}\pi^-$ final state, and Sec. IV A provides an overview of some properties of these moments.

II. EXPERIMENTAL ASPECTS AND DATA ANALYSIS

A. Experimental features

The effective-mass spectrometer was used to study not only reaction (1), but also the reactions

$$p_\uparrow p \to p\omega p \ , \tag{3}$$

$$p_\uparrow p \to pK^+K^-p \ , \tag{4}$$

$$p_\uparrow p \to \Lambda K^+ p \ , \quad \Lambda \to p\pi^- \ , \tag{5}$$

$$p_\uparrow p \to p\bar{p}pp \ . \tag{6}$$

These experiments are described elsewhere;[39–42] in particular, Ref. 39 describes the apparatus as it was used for the study of reaction (1).

To summarize the salient features, a superconducting-magnet beam line transported both longitudinally and transversely polarized protons ($\sim$60% average polarization) to a 10-in. liquid-hydrogen target. The beam spin was reversed between ZGS spills. Elastic scatters were recorded simultaneously with the inelastic triggers in order to monitor the beam polarization. These measurements were cross calibrated with an upstream polarimeter, which was used to monitor the longitudinal polarization. Because of uncertainties in the analyzing power for pp elastic scattering, we estimate a systematic uncertainty of $\pm 10\%$ in the overall beam polarization used in our measurements.

The spectrometer spark chambers provided full momentum analysis for the three forward tracks p, π^+, and π^-. In addition, a proportional-wire vertex detector provided direction measurements for wide-angle recoil tracks;[43] smaller angle tracks which missed the vertex detector were picked up in the upstream spark chambers, and so the recoil proton angular coverage was essentially 4π for reaction (1). Typical resolutions were $\delta p/p \sim 0.0017p$ (p in GeV/c) and $\delta\theta_{x,z} \sim \pm 0.5$ mrad for forward-track momenta and angles; and ± 20 mrad on the differences between predicted and measured angles for projected tracks in the recoil detector. The recoil detection efficiency depended strongly on the proton range, and effectively vanished for recoil momenta below $\sim$200 MeV/c. A segmented Cherenkov counter[44] was used in the forward-track identification. The trigger did not involve either the vertex detector or the Cherenkov counter, but imposed only a simple multiplicity requirement on the forward tracks, together with a scintillation-counter veto on multiple recoil tracks.

B. Event selection

For our studies of the relatively rare reactions (3)–(6) the $p\pi^+\pi^-p$ final state represented an enormous background. Nevertheless, these final states were identified quite cleanly, using the excellent kinematical resolution of the spectrometer and the Cherenkov and vertex-detector components. For reaction (1), on the other hand, background rejection is not a serious problem. Small backgrounds from reactions (3)–(6), and from

$$p_\uparrow p \to pp\pi^-(X) \tag{7}$$

were identified and removed using a combination of Cherenkov and kinematical information. The missing-mass (M_X) resolution alone (± 0.18 GeV^2) was adequate to reject most of the background associated with multiparticle states of the type

$$pp \to p\pi^+\pi^-(X) \ , \tag{8}$$

especially with the information from the vertex detector and target veto counters, which helped flag multiprong recoils.

The main challenge in event selection was the resolution of the p-π^+ ambiguity. The missing-mass constraint alone did not allow event-by-event separation of the hypotheses

$$pp \to p_1\pi_2^+\pi^-(p) \tag{9}$$

and

$$pp \to \pi_1^+ p_2 \pi^-(p) \ , \tag{10}$$

even though we could use the $M_X{}^2$ distributions to establish statistically the level of misidentification. Both the Cherenkov data and the recoil track measurement allowed an independent determination of the correct hypothesis for each event. The Cherenkov information allowed "unambiguous" track assignments for $\sim$95% of the events, and for the remaining events we simply assigned the proton to be the fastest positive track (identification ambiguities arose when both positive tracks were above Cherenkov threshold, $P_\pi \geq 2.9$ GeV/c, and entered the same Cherenkov quadrant). The recoil-track angle resolved the ambiguity kinematically, since the recoil polar angle is very sensitive to the effective mass of the $p\pi^+\pi^-$ system. Thus we were able to calibrate the Cherenkov identification using the sample of events having a clean recoil track. The vertex-detector identification disagreed with the Cherenkov identification for 1.8% of these events; the pattern of disagreement was consistent with the fact that fast protons (as measured with elastic scatters) fired the Cherenkov counter 1–2 % of the time, presumably through interactions in the window of the pressure vessel. A realistic Monte Carlo simulation, which was used for acceptance corrections, predicted an overall misidentification probability ranging from $\sim$3% for $-t < 0.04$ GeV^2 (where proton range limited the usefulness of the vertex detector) to $\sim$1% for $-t > 0.1$ GeV^2. No attempt was made to correct the cross sections for these effects.

Figure 1 shows the $M_X{}^2$ distributions for low- and high-mass events after applying the vertex detector and Cherenkov information in the event selection. For the final sample we imposed a cutoff, $|M_X{}^2 - M_p{}^2| < 0.6$ GeV^2. We estimate the remaining backgrounds in the event sample to be less than 5%.

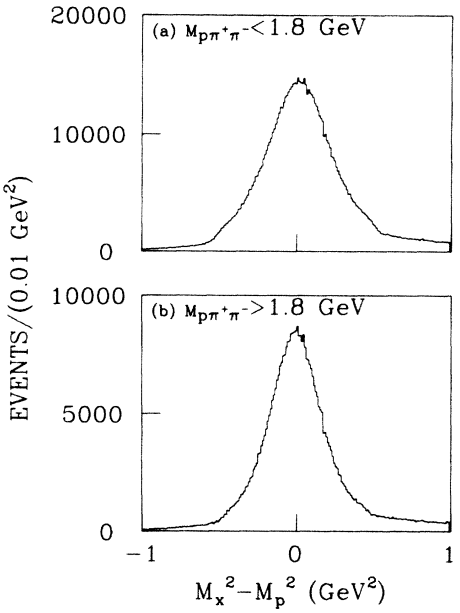

FIG. 1. The missing-mass spectra for $pp\to p\pi^+\pi^-(x)$ for selected events, with (a) $M_{p\pi^+\pi^-}<1.8$ GeV, and (b) $M_{p\pi^+\pi^-}>1.8$ GeV.

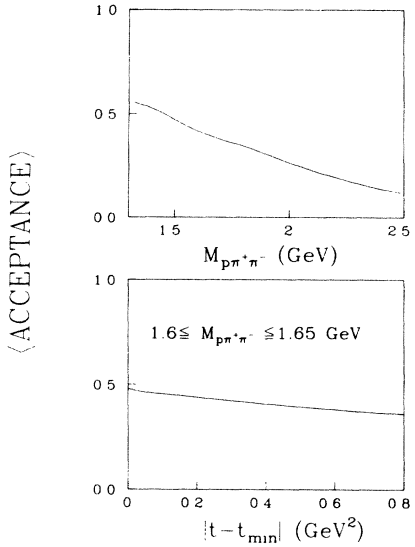

FIG. 2. The Monte Carlo acceptance, cut on $1.15<M_{p\pi^+}<1.30$ GeV and averaged over all decay angles: (a) as a function of $M_{p\pi^+\pi^-}$, averaged over t, and (b) as a function of t for a typical bin, $1.6<M_{p\pi^+\pi^-}<1.65$ GeV.

We remark that for one-third of the data taking the vertex detector was not operational, so that only the Cherenkov identification was available. We did not use this sample in obtaining the spin-averaged cross sections; we used it for polarization measurements since the statistical accuracy of these measurements was such that an $\sim 3\%$ Cherenkov misidentification would have negligible effect.

C. Acceptance corrections

A sample of 2 950 000 Monte Carlo events survived the same event-selection criteria as the real events. Some features of the Monte Carlo acceptance are illustrated in Figs. 2 and 3. Figures 2(a) and 2(b) show the average acceptance as functions of $M_{p\pi^+\pi^-}$ and momentum transfer, respectively, for events in the Δ^{++} band, defined henceforth by the cut $1.15<M_{p\pi^+}<1.30$ GeV. The dependence on the angle variables which characterize the three-body decay is shown on Fig. 3, where we have selected a particular $M_{p\pi^+\pi^-}$ bin from 1.60 to 1.65 GeV, for illustrative purposes. The decay angles are defined in the Appendix; we refer to the direction of the $(p\pi^+)$ momentum in the $(p\pi^+\pi^-)$ rest frame as $\Omega=(\Theta,\Phi)$, and the proton direction in the $(p\pi^+)$ rest frame as $\omega=(\theta,\phi)$. The acceptance is poorest for large $p\pi^+\pi^-$ mass, near $\cos\Theta=+1$; the dependence on other variables seems to be fairly benign.

Our objective in applying acceptance corrections is, of course, to obtain an unbiased description of the process, including the polarization dependence, in the seven-dimensional phase space. With our high statistics it would clearly be desirable to fit the event sample directly with the usual isobar partial-wave expansion, as has been done with spin-averaged data samples;[21–26] such an analysis of our spin-averaged data would allow direct comparison with the other analyses. However, the logistics of including the polarization information in an unbiased fashion are formidable in the partial-wave approach. Consequently, we elected to carry out a straightforward moments expansion of the data. We have binned the moments in the variables $M_{p\pi^+\pi^-}$, $M_{p\pi^+}$, and t; typically we employed fine binning in one variable at a time and coarser binning in the other two.

In principle, with fine enough binning, the moments expansion has the same information content as the isobar

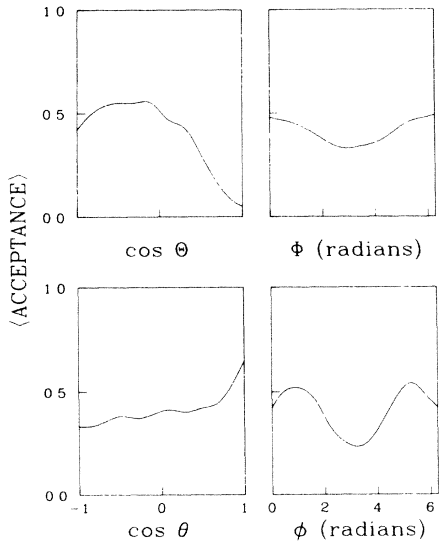

FIG. 3. The Monte Carlo acceptance, cut on $1.15<M_{p\pi^+}<1.30$ GeV, averaged over t, for the bin $1.6<M_{p\pi^+\pi^-}<1.65$ GeV: projected in $\cos\Theta$, Φ, $\cos\theta$, and ϕ.

partial-wave analysis and has the virtue of being essentially model independent and unique. It suffers from the problem that, even with a fairly restricted expansion, we are left to determine 315 moments in each $M_{p\pi^+\pi^-}$-$M_{p\pi^+}$-t bin. By comparison, the published partial-wave analyses for the production experiments[21–26] rely on typically 10–15 complex waves for each $M_{p\pi^+\pi^-}$-t bin. The statistical errors in our moments are, of course, correlated, and these correlations should in principle be retained for subsequent partial-wave fits.

The derivation of the moments expansion in terms of partial-wave production amplitudes is given in the Appendix. The most general parity-conserving description of the seven-fold differential cross section is given by

$$\begin{aligned} d^7\sigma/dt\,dM_{p\pi^+\pi^-}dM_{p\pi^+}d\Omega\,d\omega &= \sum A^L_{nm} d^l_{n0}(\theta)\,\mathrm{Re}[D^{*L}_{mn}(\Phi,\Theta,\phi)] \\ &+ P_\perp \sum B^L_{nm} d^l_{n0}(\theta)\,\mathrm{Re}[D^{*L}_{mn}(\Phi,\Theta,\phi)e^{i\psi}] \\ &+ P_z \sum C^L_{nm} d^l_{n0}(\theta)\,\mathrm{Im}[D^{*L}_{mn}(\Phi,\Theta,\phi)] , \end{aligned} \quad (11)$$

where $P_\perp$ and P_z are the respective transverse and longitudinal polarizations, and ψ is the azimuthal angle between the transverse polarization and the (Basel convention) production normal [Eqs. (A2) and (A34)]. We have restricted our analysis to $M_{p\pi^+} < 1.4$ GeV and $M_{p\pi^+\pi^-} < 2.2$ GeV; the indices in Eq. (11) were restricted to

$$\begin{aligned} &l, |\,n\,| \le 2 , \\ &m = 0,1,2 \quad (A^L_{nm} \text{ and } B^L_{nm}) , \\ &m = 0,1 \quad (C^L_{nm}) . \end{aligned} \quad (12)$$

We retained five terms in the expansion in L, where the minimum L value depends on m and n.

We fitted the moments in two stages, using a different procedure for the spin-averaged and spin-dependent moments. In the first stage, we binned the data in cosΘ since both the expansion and the acceptance are more complex in Θ than in θ, Φ, and ϕ. For each Θ bin we used maximum-likelihood techniques to obtain 63 moment coefficients (24 unpolarized, 27 for $P_\perp$, and 12 for P_Z). For example, for fixed $\theta = \theta_i$ we can write

$$\begin{aligned} d^7\sigma/dM_{p\pi^+\pi^-}dM_{p\pi^+}dt\,d\Omega\,d\omega &= \sum a_{lnm}(\Theta_i) d^l_{n0}(\theta)\cos(n\phi + m\Phi) , \end{aligned} \quad (13)$$

with similar expansions for the $P_\perp$ and P_Z contributions. In the second stage of the analysis, we obtained the desired A, B, and C coefficients by fitting the Θ dependence, e.g.,

$$a_{lnm}(\Theta_i) = \sum_L A^L_{lnm} d^L_{mn}(\Theta_i) , \quad (14)$$

and similarly for the $P_\perp$ and P_Z coefficients.

The Monte Carlo acceptance is needed to obtain the unpolarized a-type coefficients. Once the a and A coefficients are determined, the b and c coefficients can be obtained directly from the data by comparison of spin-up and spin-down event samples. Maximum-likelihood analysis leads to coupled equations for the 24 a_{lnm} coefficients:

$$\begin{aligned} \sum_{\text{events}} \frac{d^l_{n0}(\theta_i)\cos(n\phi_i + m\Phi_i)}{d^7\sigma(\theta_i,\phi_i,\Phi_i)/dx^7} &= F\int \epsilon(x) d^l_{n0}(\theta)\cos(n\phi + m\Phi)dx , \end{aligned} \quad (15)$$

where x denotes the seven-dimensional phase space for the bin, i refers to the ith event, F is the luminosity (events/mb) and σ depends on the a_{lnm} as in Eq. (13). The integral over the efficiency, $\epsilon(x)$, is given by a sum over Monte Carlo events. The error matrix for the a_{lnm} was calculated from Eq. (15) and contains comparable contributions from statistical fluctuations in the data and Monte Carlo samples.

We used the unpolarized A coefficients in the determination of the b_{lnm} and c_{lnm} correlations. Schematically, we can write

$$\sigma(x) = \sigma_0(x) + P\sum_k g_k G_k(x) , \quad (16)$$

where $\sigma_0(x)$ is the unpolarized differential cross section, g_k refers to the b_{lnm} or c_{lnm} coefficients, $G_k(x)$ are the corresponding expansion functions, and P is the value of P_z or $P_\perp$. Specifically, the $G_k(x)$ functions are

$$G_{lnm}(x) = d^l_{n0}(\theta)\cos(n\phi + m\Phi + \psi) \quad (17a)$$

and

$$G_{lnm}(x) = d^l_{n0}(\theta)\sin(n\phi + m\Phi) , \quad (17b)$$

respectively, for $P_\perp$ and P_z, as in Eq. (11). Then the solution for the coefficients, g_j, is obtained in one step from the maximum-likelihood expression

$$\begin{aligned} \sum_{(\uparrow)} - \sum_{(\downarrow)} \left[\frac{PG_k(x_i)}{\sigma_0(x_i)}\right] &= \sum_{(\uparrow)} + \sum_{(\downarrow)} \left[\frac{P^2 G_k(x_i)\sum_j G_j(x) g_j}{\sigma_0(x_i)^2}\right] , \end{aligned} \quad (18)$$

where the sums are over spin-up and spin-down events. The error matrices for the polarized coefficients are dominated by statistical errors on the spin-up and spin-down event samples, and we have ignored the statistical errors on $\sigma_0(x)$ in computing these matrices. In addition, there is an overall uncertainty of ±10% in the value of P, as stated above.

Because the acceptance suffers from some pathologies as noted above, we have checked the unpolarized cross-section expansions for positivity by evaluating the unpolarized expansion over a grid in Θ-Φ-ϕ space. For about 5% of the bins (generally for high mass and cosΘ near +1) negative cross sections were found in a few points in the grid. The angular distributions for these bins were then pulled, consistent with the error matrix, to obtain non-negative cross sections over the full grid. For ~1% of the bins these refits gave poor χ^2's; all of these cases occurred above 1.9 GeV, and these bins were not used in the fits to the A coefficients. Positivity was not imposed on the polarization coefficients, and so it is possible for

the final moments expansion to exhibit, e.g., 110% asymmetries.

We checked the A_{lnm} expansions in each bin by comparing the raw event projections in the angle variables with the predicted distributions given by the cross section and the acceptance. One example is given in Fig. 4. Similarly, the measured a_{lnm} were compared bin by bin with the A^L_{lnm} expansions; Fig. 5 provides an example for the moments with $(lnm)=(000)$ and (001).

Additional overall normalization corrections were needed to account for track-reconstruction inefficiency [(9±6)%], secondary interactions in the hydrogen target and spectrometer [(9±4)%], and hodoscope trigger biases [(4±3)%], etc.; we estimate the overall normalization uncertainties to be ±10%. Equally important, we note that the A^L_{lnm} coefficients are correlated, and so small systematic errors in the (Ω,ω) dependence of the acceptance can distort all the A^L_{lnm}, including the A^0_{000} term which gives the integrated cross section. We integrated the A^0_{000} coefficients over the kinematical range $1.30 < M_{p\pi^+\pi^-} < 2.00$ GeV, $1.15 < M_{p\pi^+} < 1.30$ GeV, and $-t < 0.5$ GeV^2; the integrated cross section, multiplied by a factor of 2 to account for the target-dissociation process, came to 590±59 μb. For comparison, Blobel *et al.*[21] obtained a cross section of 2.0±0.2 mb for reaction (1) at 12 GeV/c; the combined effects of the above cuts would retain 30.7% of their events, that is, 614±61 μb. (They do not quote this cross section; it is our estimate based on their published data.) Thus, within the normalization uncertainties, our cross sections seem to be consistent with those of Blobel *et al.*

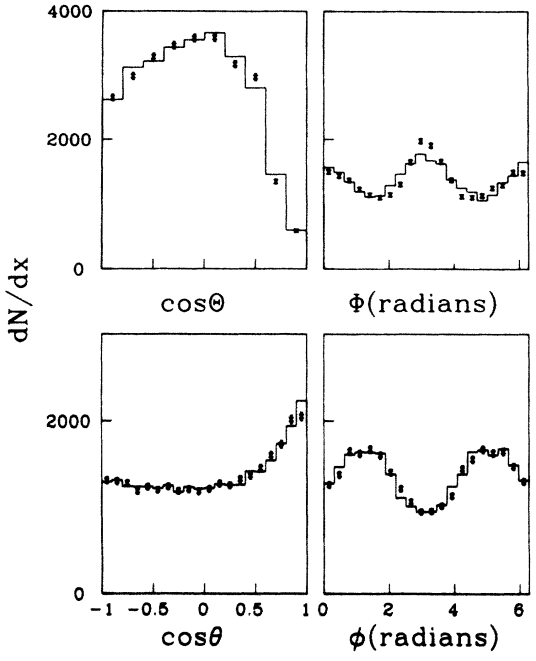

FIG. 4. Comparison of a typical joint-moments fit with the projected distributions in the angle variables cosΘ, Φ, cosθ, and ϕ. The data points are the raw event distributions; the histograms are Monte Carlo event distributions weighted by the cross-section fit. The bin is $1.15 < M_{p\pi^+} < 1.30$ GeV, $0.05 < -t < 0.25$ GeV^2, and $1.50 < M_{p\pi^+\pi^-} < 1.55$ GeV.

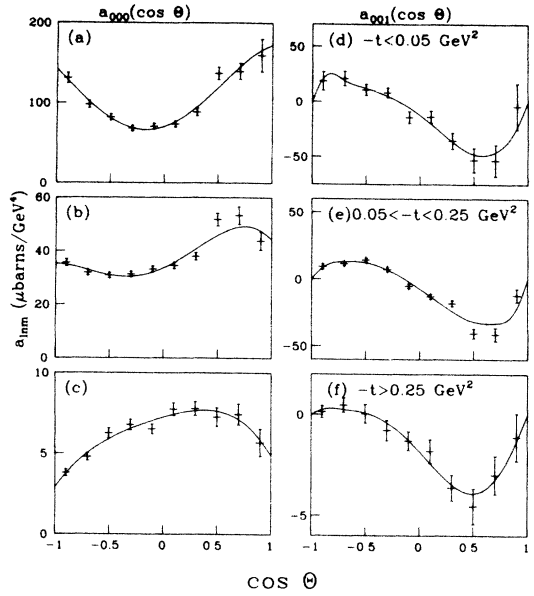

FIG. 5. Comparison of the joint-moment fits (smooth curves) with the moment fits in individual cosΘ bins (data points), for the s-channel moments a_{000} (a)–(c) and a_{001} (d)–(f); the t intervals are $-t < 0.05$ GeV^2 (a), (d), $0.05 < -t < 0.25$ GeV^2 (b), (e), and $-t > 0.25$ GeV^2 (c), (f). The mass bin is given by $1.15 < M_{p\pi^+} < 1.30$ GeV, $1.60 < M_{p\pi^+\pi^-} < 1.65$ GeV.

III. MASS SPECTRA AND ISOBAR CONTRIBUTIONS

In this paper we have restricted the moments analysis to the region $M_{p\pi^+} < 1.4$ GeV, in order to focus on the presumably clean and identifiable process

$$p_\uparrow p \to \Delta^{++}\pi^- p \ . \tag{19}$$

In this section we attempt to survey the degree of non-Δ^{++} contamination caused by other physical processes. We will show that this "contamination" shows some interesting features.

The $(p\pi^+)$ mass spectra for $M_{p\pi^+\pi^-}$ below and above 1.8 GeV are shown in Figs. 6(a) and 6(d). The Δ^{++} cut which we use for most of the moments analysis, $1.15 < M_{p\pi^+} < 1.30$ GeV, contains 56% of all events, and would be expected to include ~80% of the Δ^{++} Breit-Wigner peak depending on $M_{p\pi^+\pi^-}$. Although the Δ^{++} peak is prominent in Fig. 6, there is clear evidence of non-Δ^{++} background, both below and above the Δ^{++} mass.

Figure 7 shows the $(p\pi^+\pi^-)$ mass spectra, for all events and for Δ^{++}-cut events, in three t regions. The spectra show a well-known structure, which we will henceforth refer to as $N(1700)$, centered at 1.7 GeV with full width at half maximum (FWHM) of $\Gamma \sim 0.12$ GeV. The $N(1700)$ is more conspicuous at larger $|t|$, and only ~47% of this peak is associated with the Δ^{++}-cut events. The background spectrum under the $N(1700)$ falls

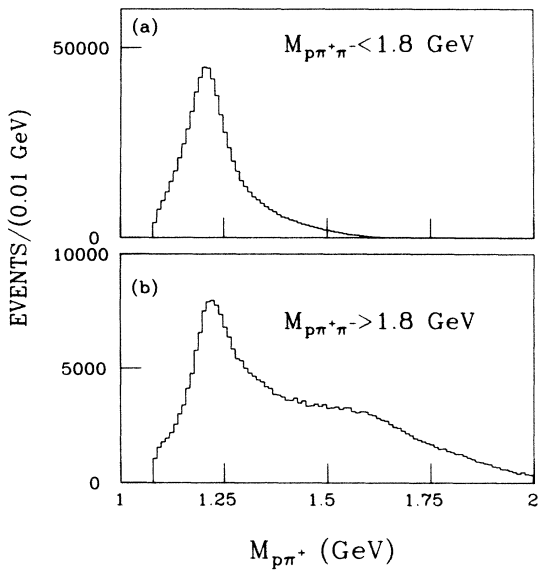

FIG. 6. Raw $M_{p\pi^+}$ spectra, for $-t<0.25$ GeV^2, for the intervals (a) $M_{p\pi^+\pi^-}<1.8$ GeV, and (b) $M_{p\pi^+\pi^-}>1.8$ GeV.

smoothly with mass. This Deck-effect background peaks around 1.45 GeV, depending on t, and is more prominent for the Δ^{++}-cut events.

We remark that in the region around 2 GeV, where missing states are predicted in the model of Isgur, Karl, and Koniuk,[38] the spectra are quite smooth. Our full event sample (Figs. 6–7 are based on two-thirds of the full sample) contains ~10000 events per 10-MeV bin in this region, mostly outside of the Δ^{++} cut—perhaps enough to warrant a more elaborate search than we present here.

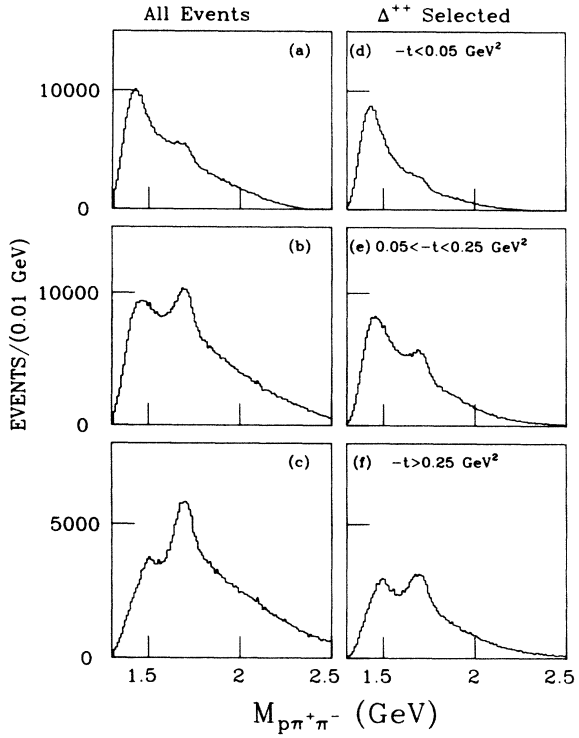

FIG. 7. Raw $M_{p\pi^+\pi^-}$ spectra, for all events (a)–(c) and events with $1.15<M_{p\pi^+}<1.30$ GeV (d)–(f), for the t intervals: (a), (d) $-t<0.05$ GeV^2, (b), (e) $0.05<-t<0.25$ GeV^2, and (c), (f) $-t>0.25$ GeV^2.

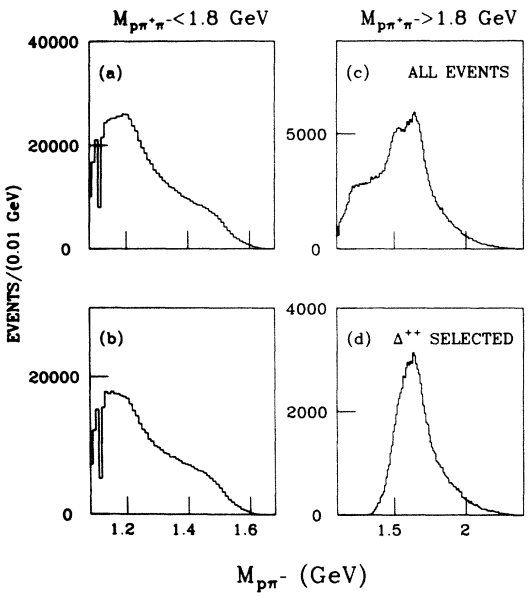

FIG. 8. Raw $M_{p\pi^-}$ spectra for $-t<0.25$ GeV^2, for (a) $M_{p\pi^+\pi^-}<1.8$ GeV, all events, and (b) $M_{p\pi^+\pi^-}<1.8$ GeV with Δ^{++} cut, (c) $M_{p\pi^+\pi^-}>1.8$ GeV, all events, and (d) $M_{p\pi^+\pi^-}>1.8$ GeV with Δ^{++} cut. The dip close to threshold is an artifact of the antiselection on $\Lambda(1115)\to p\pi^-$.

The other isobar combinations are shown in Fig. 8 ($p\pi^-$) and Fig. 9 ($\pi^+\pi^-$). For $M_{p\pi^+\pi^-}<1.8$ GeV, these spectra are fairly smooth. The Δ^0 signal is not prominent; other analyses[21–26] claim consistency with $\Delta^0/\Delta^{++}\simeq\frac{1}{9}$, as expected for $I=\frac{1}{2}$ ($p\pi^+\pi^-$) production. For $M_{p\pi^+\pi^-}>1.8$ GeV, small signals can be seen for Δ^0,

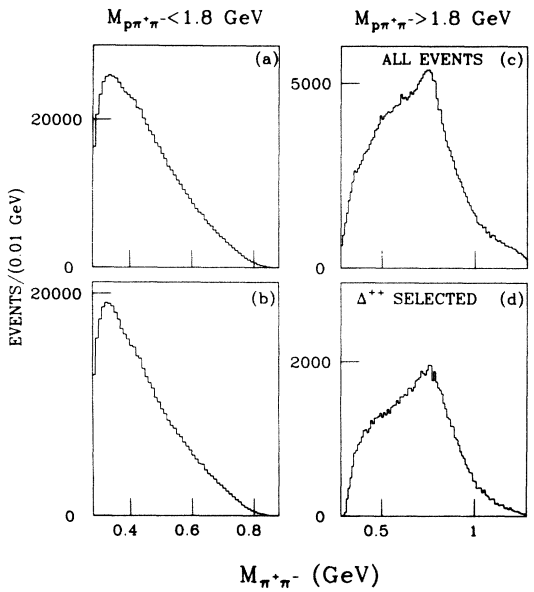

FIG. 9. Raw $M_{\pi^+\pi^-}$ spectra for $-t<0.25$ GeV^2, cut on $M_{p\pi^+\pi^-}$ and $M_{p\pi^+}$ as in Fig. 8.

$N^*(1520)$, and $N^*(1680)$ in Fig. 8(c), and for $\rho^0(770)$ in Figs. 9(c) and 9(d). Of these only the Δ^0 signal is excluded by the Δ^{++} cut [Fig. 9(d)]. Thus, the non-Δ^{++} background includes a mix of Δ^0, N^{*0}, and ρ^0 isobar contributions, and possibly other nonresonant components such as the $(\pi\pi)$ S wave (the ϵ), $p\pi^{\pm}$ S waves, etc. The recoil proton does not appear to pose any major problem; the only evidence we see for isobar formation involving the recoil proton is in the $(\pi^- p_r)$ system (Fig. 10). We have made no cuts to eliminate these effects, and they are in principle included in the Deck-model calculation.

The published partial-wave analyses,[21–26] all eschew the need for $N^{*0}\pi^+$ isobars, and fit their data with $\Delta^{++}\pi^-$, $p\epsilon^0$, and $p\rho^0$ waves. Qualitatively these analyses indicate only small $p\rho^0$ waves; they indicate that most of the cross section is divided between $\Delta^{++}\pi^-$ and $p\epsilon$ waves, roughly 50/50. Our mass spectra are consistent with the observation that $\sim 50\%$ of the events must come from sources other than $\Delta^{++}\pi^-$; however, by a process of elimination we conclude that the $p\epsilon$ contribution may be much smaller than claimed in these other analyses. We remark that the $p\epsilon$ isobar does provide a natural parametrization for the background under the Δ^{++} (cf. Fig. 6). First, the ϵ is broad and featureless, and kinematically the reflection of $p\epsilon$ onto the $M_{p\pi^+}$ spectrum results in a smooth background covering the full kinematic range. Second, for $(\pi^+\pi^-)$ masses so close to threshold [cf. Figs. 9(a) and 9(b)], we would expect S-wave production to dominate the $\pi\pi$ system, irrespective of the actual parent-isobar configuration. However, these same considerations suggest that we cannot isolate the amount of $p\epsilon$ just from, e.g., the mass spectra, but rather we need first to account for other, clearly identifiable isobar contributions.

Assuming that the low-mass threshold enhancement is due to the $\Delta^{++}\pi^-$ Deck effect, illustrated in Fig. 11(a),

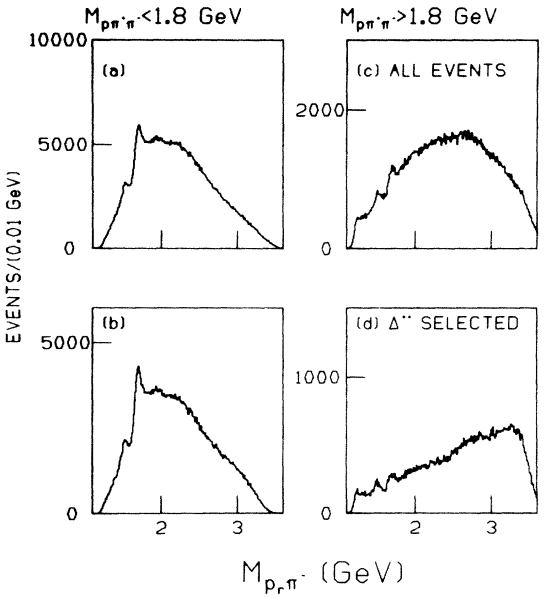

FIG. 10. Raw $M_{p_r\pi^-}$ spectra for $-t<0.25$ GeV^2, cut on $M_{p\pi^+\pi^-}$ and $M_{p\pi^+}$ as in Fig. 8.

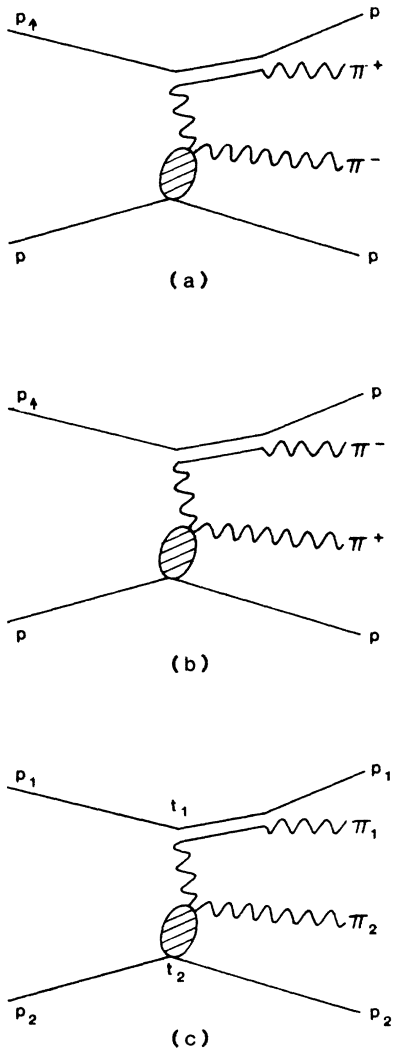

FIG. 11. Pion-exchange Deck diagrams responsible for (a) Δ^{++} isobars and (b) N^{*0} isobars; (c) defines the kinematical variables for the general case.

then for consistency one would expect other $N^{*0}\pi^+$ Deck-effect contributions from π^+ exchange as shown in Fig. 11(b). The relative cross sections for these π^+-exchange Deck effects are given by the Chew-Low formula:[45]

$$\frac{d^3\sigma}{dt_1 dt_2 dM_{p_1\pi_1\pi_2}} \propto (M_{p_1\pi_1})^2 \sigma(\pi_1 p_1 \to \pi_1 p_1) \frac{1}{(t_1 - m_\pi^2)^2} \times (M_{p_2\pi_2})^2 (q_{p_2\pi_2})^2 \frac{d\sigma}{dt_2}(\pi_2 p_2 \to \pi_2 p_2) \,. \tag{20}$$

The kinematics for Eq. (20) are illustrated in Fig. 11(c); $M_{p_1\pi_1}$ refers to the Δ or N^* mass, and it is the contribution from high-mass $\pi_2 p_2$ scattering which causes the traditional Deck-effect enhancement in the low-mass $p_1\pi_1\pi_2$ system. If we ignore the difference between $\pi^+ p$ and $\pi^- p$ scattering at the lower vertex in Fig. 11(c), and also the kinematical correlations which exist between $M_{p_1\pi_1}$ and $M_{p_2\pi_2}$ due to the threshold constraint on $M_{p_1\pi_1\pi_2}$, then the individual isobar contributions would be

roughly proportional to

$$\sigma(N^*) \propto \int dM_{p_1\pi_1}(M_{p_1\pi_1})^2 \sigma(\pi_1 p_1 \to \pi_1 p_1) . \quad (21)$$

Using nominal cross sections and resonance widths, we obtain

$$\sigma(\Delta^{++}):\sigma(\Delta^0):\sigma(N_{1440}):\sigma(N_{1520}):\sigma(N_{1680}) \simeq 1.0:0.11:0.12:0.16:0.26 . \quad (22)$$

Experimentally, we have fitted the raw mass spectra (see below) to obtain the following approximate breakdown for the identifiable isobar contributions; for $-t<0.2$ GeV^2 we find

$$\sigma(\Delta^{++}):\sigma(N_{1520}):\sigma(N_{1680}):\sigma(\rho_{770}):\text{total} \simeq 1.0:0.13:0.15:0.045:1.84 . \quad (23)$$

The ratios in Eq. (23) are not acceptance corrected, and the high-mass isobar contributions would be approximately 40% larger, relative to the Δ^{++} contribution, if the acceptance corrections were included [cf. Fig. 2(a)]. If we ignore the acceptance corrections, and include the Deck-effect estimates for $\sigma(\Delta^0)$ and $\sigma(N_{1440})$ from Eq. (22), then these six contributions would make up $\sim 84\%$ of the total event rate. We cannot obtain meaningful estimates for Δ^0 or N_{1440} production from the raw mass spectra, and we cannot perform acceptance corrections without a full moments analysis or partial-wave analysis. Nonetheless, it appears that "known" sources, expected in a consistent Deck-model description, could account for most of the event rate.

We have elaborated on the possible role of N^*-π^+ isobars, not only because they are ignored in other analyses, but also because of an interesting effect in the $N(1520)\pi^+$ channel. Figure 12 shows the ($M_{p\pi^-}$) spectra in two $M_{p\pi^+\pi^-}$ mass intervals, for $-t$ below and above 0.2 GeV^2. There is a clear $N(1520)$ peak, centered at 1.50 GeV, with a FWHM of $\Gamma \simeq 100$ MeV, for $M_{p\pi^+\pi^-} > 1.7$ GeV; it is present in both t intervals [Figs. 12(a) and 12(b)]. These signals are significantly reduced if the $M_{p\pi^+\pi^-}$ cutoff is increased to 1.9 GeV [Figs. 12(c) and 12(d)]. Thus we conclude that most of the $N(1520)$ signal is produced below 1.9 GeV. The dashed histograms show that effect of the Δ^{++}-band cut. The $N(1520)$ signals are still prominent in the dashed histograms of Figs. 17(a) and 17(b), on top of broad backgrounds which are, for the most part, reflections of genuine $\Delta^{++}\pi^-$ events. For larger $M_{p\pi^+\pi^-}$ [Figs. 12(c) and 12(d)] the Δ^{++}-band cut excludes the $N(1520)$ events.

We fitted all the isobar spectra to forms involving the Breit-Wigner peak plus linear background, with appropriate phase-space factors, using 25-MeV bins in $M_{p\pi^+\pi^-}$. We fixed the isobar masses and widths for these fits to be $=1.23$, 0.12 GeV for Δ^{++}; 1.50, 0.12 GeV for $N(1520)$; 1.68, 0.15 GeV for $N(1680)$; and 0.77, 0.15 GeV for $\rho^0(770)$, respectively. The solid curves in Figs. 12(a) and 12(b) illustrate such a fit for $N(1520)$. Figure 13 shows the excitation curves for these isobar contributions for $-t<0.2$ GeV^2, and Fig. 14 shows the same for $0.2<-t<0.8$ GeV^2; the total event sample is also indicated in each case. We emphasize that these are fits to raw data, with no acceptance corrections. Also these fits probably underestimate the signals below threshold for each particular isobar.

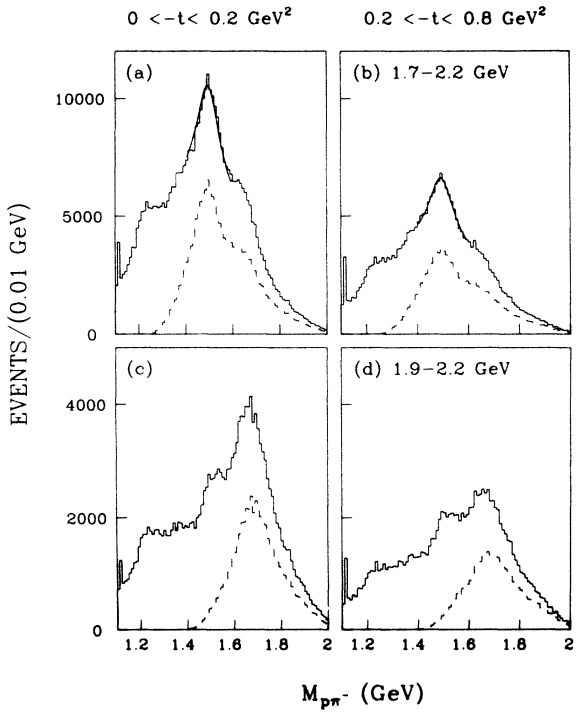

FIG. 12. Raw $M_{p\pi^-}$ spectra for (a) $1.7<M_{p\pi^+\pi^-}<2.2$ GeV and $-t<0.2$ GeV^2, (b) $1.7<M_{p\pi^+\pi^-}<2.2$ GeV and $0.2<-t<0.8$ GeV^2, (c) $1.9<M_{p\pi^+\pi^-}<2.2$ GeV and $-t<0.2$ GeV^2, and (d) $1.9<M_{p\pi^+\pi^-}<2.2$ GeV and $0.2<-t<0.8$ GeV^2. The solid histogram gives all events, and the solid curve in (a) and (b) represent fits to $N(1520)$ plus background over $1.4<M_{p\pi^-}<1.6$ GeV. The dashed histograms show the effect of the Δ^{++} cut.

It can be seen that the $N(1700)$ enhancement in the total event rate coincides with enhancements in both $\Delta^{++}\pi^-$ and $N(1520)\pi^+$, for both momentum-transfer regions. The sharp enhancement above threshold seen in $N(1520)\pi^+$ may well have a more gradual falloff below threshold than our fits indicate. However, as we noted above, most of the $N(1520)\pi^+$ production is confined to the region near threshold. Above ~ 1.6 GeV, these isobar contributions provide a plausible accounting for most of the event rate. Below the $N(1520)\pi^+$ threshold enhancement, there is a clear paucity of events. As noted, we could not extract Δ^0 or $N(1440)$ production signals; also our fits may systematically underestimate the Δ^{++} signals for various reasons. The combined enhancements in $\Delta^{++}\pi^-$ and $N(1520)\pi^+$ are larger than the $N(1700)$ enhancement seen in the total event rate, and so the non-Δ^{++} component below $N(1520)\pi^+$ threshold must somehow synchronize with the $N(1520)\pi^+$ excitation, in order to smooth out the total cross section.

Could the $N(1520)\pi^+$ effect be a kinematical reflection of some other process? Kinematically there are no candi-

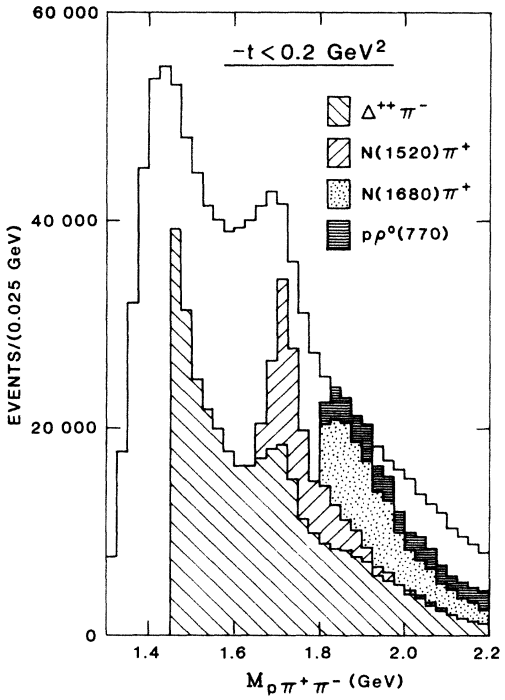

FIG. 13. Spectra of isobar contributions vs $M_{p\pi^+\pi^-}$ for $-t<0.2$ GeV^2. The solid histogram gives the total event sample, and the shaded histograms indicate the respective $\Delta^{++}\pi^-$, $N(1520)\pi^+$, $N(1680)\pi^+$, and $p\rho^0(770)$ event rates obtained from independent fits to isobar Breit-Wigner peak plus background. The histograms are cumulative, and no acceptance corrections have been applied.

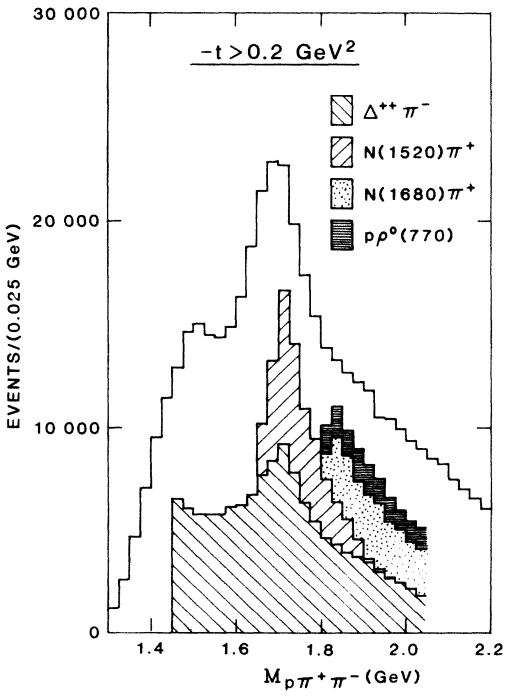

FIG. 14. Spectra of isobar contributions vs $M_{p\pi^+\pi^-}$ for $-t>0.2$ GeV^2, labeled as in Fig. 13.

date processes involving $\pi^+\pi^-$ isobars, or the recoil proton [e.g., $N(1520)\Delta^{++}$ final states]. However, the kinematics are somewhat subtle in that there is a strong correlation between $M_{p\pi^+}$ and $M_{p\pi^-}$; the Dalitz plot is approximately cigar shaped in these variables, and in the mass region of interest we have $M_{p\pi^+}\approx -M_{p\pi^-}+F(M_{p\pi^+\pi^-})$. Thus the Δ^{++} reflects as a comparable-width peak in the $M_{p\pi^-}$ spectrum and conversely the $N(1520)$ reflects as an $\sim$120-MeV wide peak in the $M_{p\pi^+}$ spectrum. The two isobars are conjugate for $M_{p\pi^+\pi^-}\approx 1.8$ GeV (they overlap in either spectrum), and if there were a resonance at 1.8 GeV that decayed into $\Delta^{++}\pi^-$, it would show up in our fits as a comparable peak in $N(1520)\pi^+$. Fortunately the $\Delta^{++}\pi^-$ spectrum is fairly smooth, and there is no peak at 1.8 GeV which could lead to this sort of confusion. The $N(1700)$ enhancement in $\Delta^{++}\pi^-$ is reflected as an enhancement in $M_{p\pi^-}$ around 1.41 GeV, below the $N(1520)$ signal. Thus, there is no plausible reflection effect involving $\Delta^{++}\pi^-$ that could account for the $N(1520)\pi^+$ enhancement seen in Figs. 13 and 14. We conclude that the $N(1520)\pi^+$ peak is probably one component of the $N(1700)$ effect, especially since it does not disappear at larger momentum transfer, where $N(1700)$ is most prominent (Fig. 14).

Other analyses do show modest peaks in the $M_{p\pi^-}$ spectrum around 1.5 GeV.[21,26] It may be worth noting that, close to threshold in the $N^{*0}\pi^+$ mass, the effective mass between the π^+ and the recoil proton is small [$M_{p_r\pi^+}\simeq 1.6$ GeV at $N(1520)\pi^+$ and $N(1680)\pi^+$ thresholds]; thus some of the signal near threshold could be lost in analyses which antiselect low $M_{p_r\pi^+}$ masses. Also we note that the $N(1520)\pi^+$ signal represents only $\sim$7% of our total event sample, and could easily be ignored in lower-statistics experiments.

In any case, the $N(1520)\pi^+$ enhancement constitutes one of the backgrounds in the Δ^{++} band; in the vicinity of the $N(1700)$, this background is concentrated below the Δ^{++} in the $M_{p\pi^+}$ spectrum. To the extent that it is concentrated near threshold in $M_{p\pi^+}$, it might be expected to show up as background S and P waves in the $p\pi^+$ system.

We have used the acceptance-corrected moments to repeat the above analysis on the $\Delta_{++}\pi^-$ system. We fitted the cross sections in each $M_{p\pi^+\pi^-}$ bin as functions of $M_{p\pi^+}$. Figure 15 shows these fits (solid curves), together with the contributions from the Δ^{++} Breit-Wigner peaks (dashed curves) and linear backgrounds modified by phase space (dotted curves). Figure 16 shows the total cross section and the $\Delta^{++}\pi^-$ contribution obtained from the above fits, integrated over the Δ^{++}band cut (1.15—1.30 GeV). The purpose of this analysis was to estimate the amount of non-Δ^{++} background within the Δ^{++} cut. The decomposition in Fig. 16 bears a qualitative similarity to that in Fig. 13. Even with the Δ^{++} band cut, we find that only 69% of the cross section is associated with $\Delta^{++}\pi^-$, for $M_{p\pi^+\pi^-}>1.45$ GeV. (We did not attempt any of these fits for smaller $M_{p\pi^+\pi^-}$ due to the limited kinematical range.)

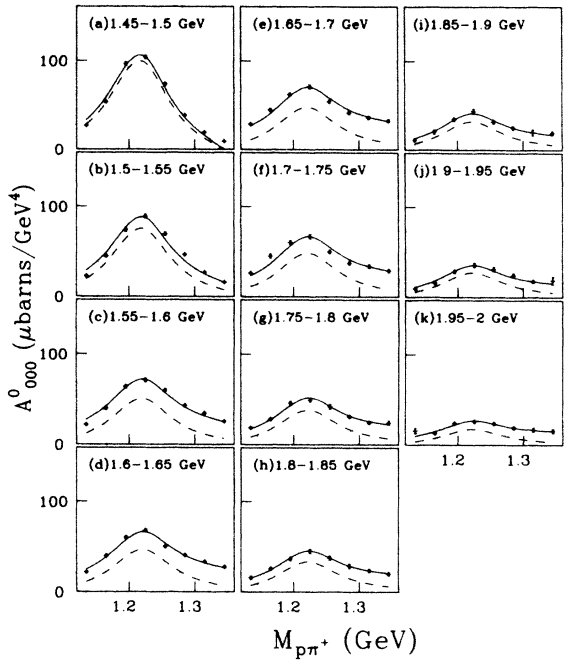

FIG. 15. Acceptance-corrected A^0_{000} distributions, showing the $M_{p\pi^+}$ dependence in eleven $M_{p\pi^+\pi^-}$ bins from 1.45 to 2 GeV, for $-t<0.25$ GeV^2. The solid, dashed, and dotted curves give the total, Δ^{++}, and background contributions, respectively. Note that $A^0_{000}=(1/16\pi^2)d^3\sigma/dt\,dM_{p\pi^+\pi^-}dM_{p\pi^+}$.

We conclude this section with a summary.

(1) With a 400-fold increase in statistics, as compared with the most extensive published analysis of reaction (1)[21,22] we see no new structures in the $M_{p\pi^+\pi^-}$ spectrum, only the $N(1700)$ peak on a Deck-type background.

(2) Without acceptance corrections, we estimate that 54% of the events, overall, are associated with $\Delta^{++}\pi^-$. The partial-wave analyses have attributed most of the remaining events to $p\epsilon$, and we do not doubt that this topology could provide a reasonable parametrization of the non-Δ^{++} background. However, we can identify significant $N^{*0}\pi^+$ isobar contributions, which would be expected in a consistent Deck model. We cannot reliably determine the nature of the non-Δ^{++} background below 1.6 GeV from mass spectra alone. However, including nominal $\Delta^0\pi^+$ and $N(1440)\pi^+$ contributions, one could account plausibly for at least 84% of the total event rate below 2.2 GeV, with no $p\epsilon$ component.

(3) The Δ^{++}-band cut which we use for moments analysis includes an $\sim$30% non-$\Delta^{++}\pi^-$ background.

(4) We find that the $N(1520)\pi^+$ signal peaks sharply at threshold and probably accounts for a substantial share of the $N(1700)$ peak; only $\sim$47% of the $N(1700)$ signal is associated with $\Delta^{++}\pi^-$. The $N(1520)\pi^+$ signal is also prominent at large $-t$, where $N(1700)$ is most conspicuous. We note that the partial-wave analyses[21–26] have found that $N(1700)$ is not pure $J^P=\frac{5}{2}^+$, as might be expected in this mass region, but is a mix of $J=\frac{1}{2}$, $\frac{3}{2}$, and $\frac{5}{2}$ states. The $N(1520)\pi^+$ system is unlikely to have $J^P=\frac{5}{2}^+$ so close to threshold (this would require an overall D wave), and we conjecture that its presence might naturally explain why $\frac{5}{2}^+$ is not the only state observed.

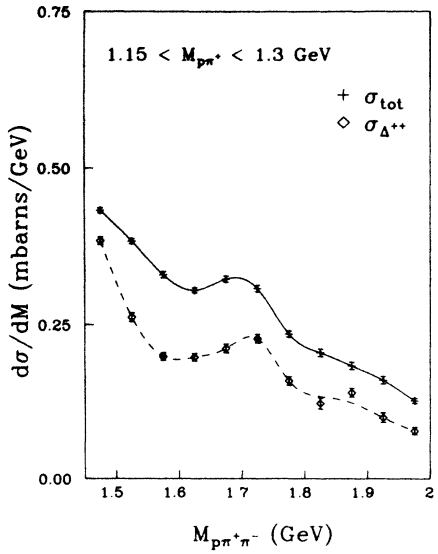

FIG. 16. Differential cross section, $d\sigma/dM$, integrated over the Δ^{++} cut, $1.15<M_{p\pi^+}<1.30$ GeV. Crosses indicate total cross section, and diamonds the $\Delta^{++}\pi^-$ contribution as obtained from the fits illustrated in Fig. 15.

IV. MOMENTUM-TRANSFER DEPENDENCE OF THE JOINT MOMENTS

A. Overview

In this and the following sections, we will examine the behavior of the angular-distribution moments and their interpretation in terms of partial-wave production amplitudes. First we call attention to notational conventions which we will adopt, and to certain properties of the moments which come up repeatedly in the subsequent discussion (see also the Appendix).

(1) We do not attempt to set up a precise nomenclature for the partial waves, because this would require at least seven indices per wave [see Eq. (A12)]; we will use appropriate nomenclature as the discussion demands. We will consistently use $S,P,D,\ldots$ to refer to the orbital momentum between the $(p\pi^+)$ system and the π^- in the $(p\pi^+\pi^-)$ c.m. We will henceforth use s, p, Δ to refer to $j^P=\frac{1}{2}^-$, $\frac{1}{2}^+$, $\frac{3}{2}^+$ $(p\pi^+)$ systems, respectively. We do not consider other isobar configurations since we confine the moments analysis to the Δ^{++} band; backgrounds from $p\epsilon$, $N^*\pi$, etc., are expected to populate s, p, and Δ waves.

(2) The moments A^L_{lnm}, B^L_{lnm}, and C^L_{lnm} with $l=1$ require interferences between s and Δ- or s- and p-wave isobars. Thus, $l=1$ moments help to isolate the effects of non-$\Delta^{++}\pi^-$ waves. The $l=0,2$ moments are expected to be dominated by $\Delta\Delta$ interferences.

(3) The partial-wave contributions to moments having different n values are related; in particular, for A^L_{lnm}, B^L_{lnm}, and C^L_{lnm} we have

$$M^L_{lmn}=(-1)^L\eta\eta' M^L_{l-nm}\ , \tag{24}$$

where η,η' are the parities of the interfering $(p\pi^+\pi^-)$ waves. Thus, it is useful to compare moments which differ only in n.

(4) We will refer to "helicity-conserving" and "helicity-nonconserving" moments. The helicity-conserving moments are A^L_{lnm}, C^L_{lnm} with $m=0$, and B^L_{lnm} with $m=1$. The helicity-nonconserving moments vanish if only helicity-conserving $(\lambda=+\frac{1}{2})$ production amplitudes occur. Because of parity conservation, the beam helicity can be chosen to be $+\frac{1}{2}$ for all amplitudes, so that the helicity-nonconserving amplitudes are those with $\lambda=\frac{3}{2}$, $-\frac{1}{2}$, $-\frac{3}{2}$ for the $(p\pi^+\pi^-)$ system. These conventions apply separately to s- and t-channel descriptions; we denote the respective helicities by λ_s and λ_t.

(5) The helicity-nonconserving spin correlations are familiar in that they involve flip-nonflip interference in the overall production amplitudes. The helicity-conserving spin correlations do not require any overall helicity flip between the beam and the $(p\pi^+\pi^-)$ system. They can be thought of as a reflection of the spin dependence in the virtual process

$$p_t P_e \to p\pi^+\pi^- , \tag{25}$$

where P_e is a helicity=0 exchange, like the Pomeron. These moments require interference of different partial waves in the $(p\pi^+\pi^-)$ system, and are thus sensitive to the spectroscopy, as distinct from the production mechanisms.

B. Slope-mass correlation and the low-mass S wave

We now turn to the t dependence of reaction (1), t being the momentum transfer from the polarized beam to the $(p\pi^+\pi^-)$ system. Recall from Eq. (11) that the unpolarized cross section is expressed as

$$\frac{d^7\sigma}{dt\, dM_{p\pi^+\pi^-} dM_{p\pi^+} d\Omega\, d\omega} = \sum A^L_{lnm} \cos(n\phi + m\Phi) d^l_{n0}(\theta) d^L_{mn}(\Theta) ,$$

with

$$\frac{d^3\sigma}{dt\, dM_{p\pi^+\pi^-} dM_{p\pi^+}} = (4\pi)^2 A^0_{000} . \tag{26}$$

The Δ^{++} decay distribution in (θ,ϕ) proves to be a powerful analyzer of the partial-wave structures.

The t distributions for A^0_{000} are shown in Fig. 17, for 100-MeV bins in $Mp\pi^+\pi^-$. A clear break in the lower-mass t distributions appears around $-t=0.25$ GeV^2, similar to that observed at much higher energies, both for $N\to N\pi$ (Refs. 1, 7, 8) and $p\to p\pi^+\pi^-$ (Ref. 7). We have fitted the t slopes above and below this break, as shown in Fig. 18. Although not shown, our small $-t$ slopes are remarkably close to those reported at $\sqrt{s}=53$ GeV by Goggi *et al.*[7] for reaction (1); the CERN ISR slopes have very similar mass dependence, but are systematically larger by ~ 1.8 GeV^{-2} for all $Mp\pi^+\pi^-$ and both t regions.

The slope-mass correlation and the break structure require revisions to the basic pion-exchange Deck model. Several models[46] have attributed the break structure to crossover zeros in the $\lambda_s=\frac{1}{2}$ waves. They explain the slope-mass correlation by an increase in the $\lambda_s\neq\frac{1}{2}$ cross section with increasing mass, due to the onset of higher L and J waves. Our moments do indicate a crossover zero in the $\lambda_s=\frac{1}{2}$ amplitudes, but do not suggest that the helicity-flip cross section grows significantly with mass (if

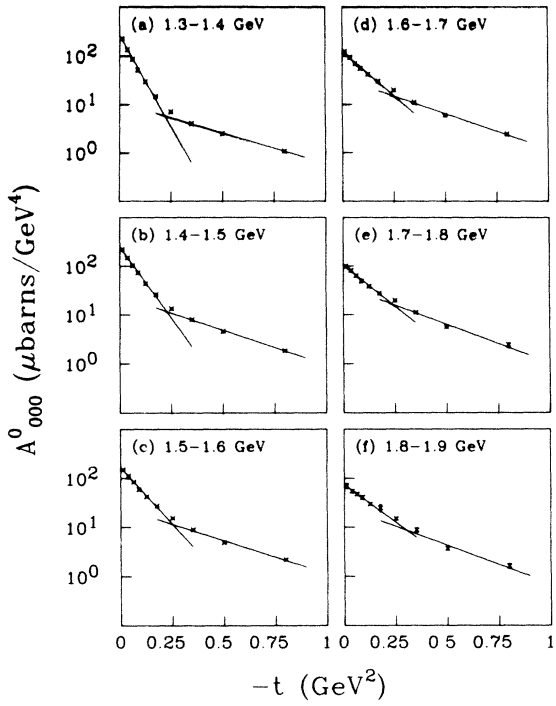

FIG. 17. Forward differential cross-section coefficients, A^0_{000}, for six $M_{p\pi^+\pi^-}$ mass intervals (with Δ^{++} cut applied).

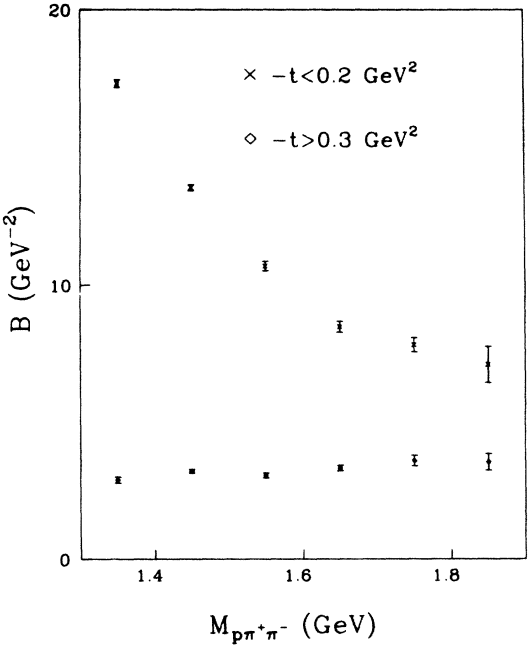

FIG. 18. Slopes fitted to the t distributions of Fig. 17; crosses indicate fits to the region $-t<0.2$ GeV^2, and diamonds the region $0.3<-t<0.8$ GeV^2.

anything, it is larger at low masses). In the framework of the Deck model, Berger and Pirilä[31] have also proposed that the break structure is due to crossovers in the $\lambda_s=\frac{1}{2}$ waves; they attribute the slope-mass correlation to an outward movement of these crossover locations with increasing mass (due to mass dependence in the absorption corrections). In their model, each wave has its own slope-mass correlation, and the break is clearer at low masses because of the dominance of a single wave, namely, the S wave. S-wave dominance for the threshold enhancement is a natural consequence of the pion-exchange Deck amplitude,[28] and appears to be true experimentally in our data and in other studies of $N\to N\pi^6$ and $p\to p\pi^+\pi^-$ (Refs. 21–26) DD processes. Our moments appear to be consistent with the Berger-Pirilä predictions, specifically with a crossover zero in the $\lambda_s=\frac{1}{2}$ S wave which moves out in t with increasing mass. An alternative model, proposed by Cohen-Tannoudji, Santoro, and Souza,[32] attributes the break structure to cancellations between pion-exchange, nucleon-exchange, and nucleon-pole diagrams in the three-component Deck model. This model assumes important resonance contributions in $\frac{1}{2}^+$, $\frac{3}{2}^-$, and $\frac{5}{2}^+$ waves, and naturally enhances the break in the $J^P=\frac{1}{2}^+$ P wave in $\Delta\pi$, having the same J^P as the nucleon pole. Our moments clearly require $J^P=\frac{3}{2}^-$ S-wave dominance for the threshold bump and restrict the $J^P=\frac{1}{2}^+$ contributions to the ~ 10–20% level.

To interpret the angular distribution moments, it is convenient to consider the situation for pure S-wave $J^P=\frac{3}{2}^-$ $\Delta^{++}\pi^-$ production. The resulting moments are quite simple:

$$A^0_{000}=|S^1|^2+|S^{-1}|^2+|S^3|^2+|S^{-3}|^2\,, \tag{27a}$$

$$A^2_{200}=\tfrac{1}{2}A^2_{210}=\tfrac{1}{2}A^2_{220}$$
$$=|S^1|^2+|S^{-1}|^2-|S^3|^2-|S^{-3}|^2\,, \tag{27b}$$

$$A^2_{201}=A^2_{2\pm11}=A^2_{2\pm22}=2.83\,\mathrm{Re}(S^1S^{3*}-S^{-1}S^{-3*})\,, \tag{27c}$$

$$A^2_{202}=A^2_{2\pm12}=A^2_{2\pm22}$$
$$=-2.83\,\mathrm{Re}(S^1S^{-3*}+S^3S^{-1*})\,, \tag{27d}$$

where the subscripts denote helicity. All other A^L_{lnm} vanish. In particular, A^0_{200}, which vanishes for pure S wave, is very sensitive to P- and D-wave content. For example, $A^0_{200}/A^0_{000}=+1$ for pure $J^P=\frac{1}{2}^+$ P wave $\Delta-\pi$.

The data seem to reflect these simple S-wave dominance constraints. Figure 19 shows the $l=2$, $m=0$ (helicity-conserving) moments in the t channel, plotted against t for two mass intervals. First, note that $A^0_{200}\approx 0$, which immediately rules out the possibility that the Deck-effect enhancement is caused by the $N(1440)$ resonance in the $\frac{1}{2}^+$ P wave. Second, note that the relationship between the A^2_{2n0} given by Eq. (27b) is approximately valid, more so for low t and the low-mass region [Figs. 19(b)–19(d)]. The $m=1$ and $m=2$ helicity-nonconserving moments are generally small in the t channel, as shown in Figs. 20 and 21.

In the s channel, the situation appears to be rather dif-

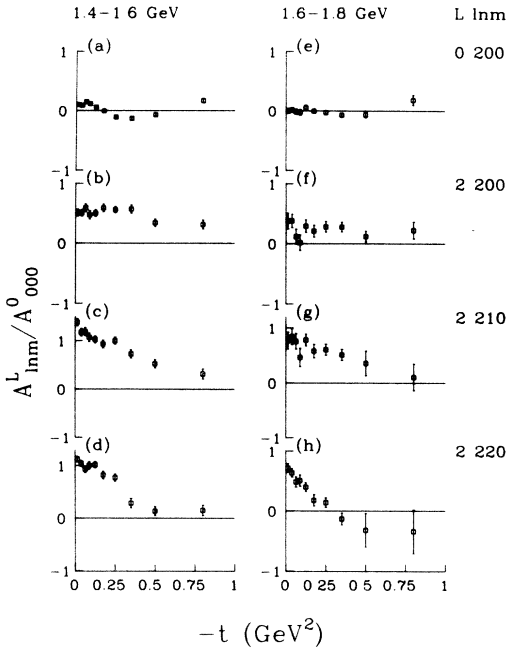

FIG. 19. t channel A^L_{lnm}/A^0_{000} moments with $m=0$ plotted against t for $1.4<M_{p\pi^+\pi^-}<1.6$ GeV (a)–(d), and $1.6<M_{p\pi^+\pi^-}<1.8$ GeV (e)–(h): (a), (e) A^0_{200}; (b), (f) A^2_{200}; (c), (g) A^2_{210}; and (d), (h) A^2_{200}.

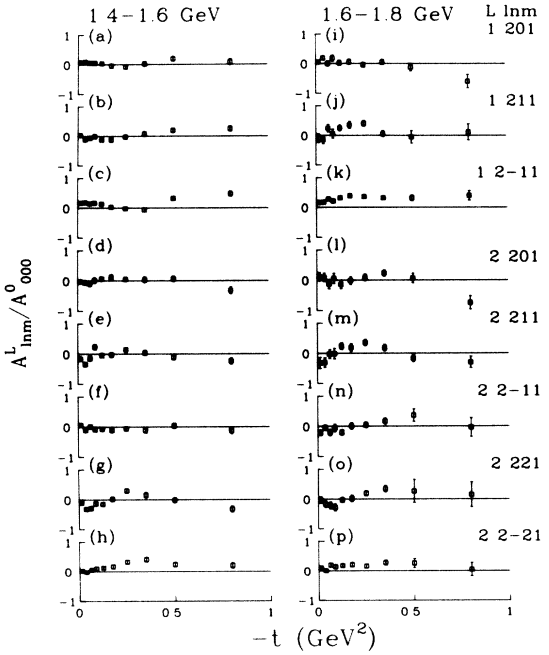

FIG. 20. t-channel A^L_{lnm}/A^0_{000} moments with $m=1$ plotted against t for $1.4<M_{p\pi^+\pi^-}<1.6$ GeV (a)–(h), and $1.6<M_{p\pi^+\pi^-}<1.8$ GeV (i)–(p): (a), (i) A^1_{201}; (b), (j) A^1_{211}; (c), (r) $A^1_{2\text{-}11}$; (d), (l) A^2_{201}; (e), (m) A^2_{211}; (f), (n) $A^2_{2\text{-}11}$; (g), (o) A^2_{221}; and (h), (p) $A^2_{2\text{-}21}$.

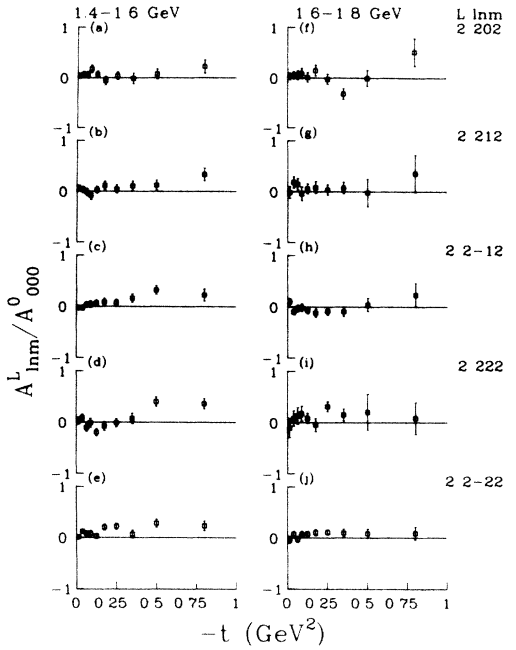

FIG. 21. t-channel A^L_{lnm}/A^0_{000} moments with $m=2$ plotted against t for low-mass (a)–(e) and high-mass (f)–(j) bins: (a), (f) A^2_{202}; (b), (g) A^2_{212}; (c), (h) $A^2_{2\text{-}12}$; (d), (i) A^2_{222}; and (e), (j) $A^2_{2\text{-}22}$.

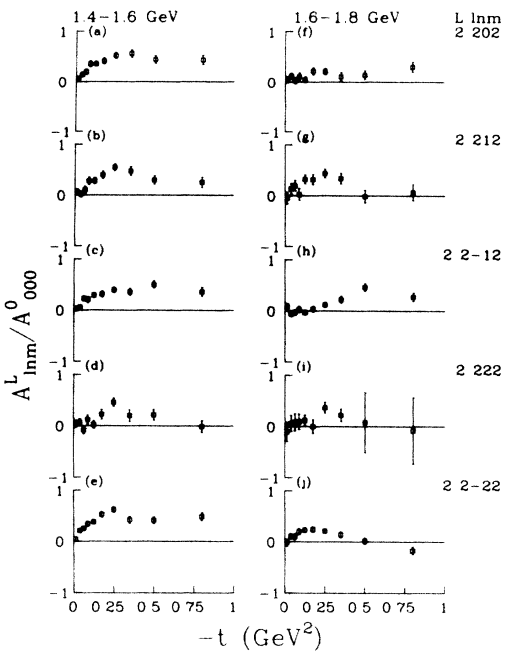

FIG. 23. s-channel A^L_{lnm}/A^0_{000} moments with $m=2$ plotted against t, labeled as in Fig. 21.

ferent. Away from $t=0$, the $m=1$ and $m=2$ helicity-nonconserving moments for $l=2$ are comparable to the $m=0$ terms (see Figs. 22 and 23). In the low-mass region, the $m=1,2$ moments display the regularities predicted by Eqs. (27c) and (27d). First, the $L=1$ moments are generally small [Figs. 22(a)–22(c)]. Second, the $L=2$, $l=2$ moments are approximately independent of n: see Figs. 22(d)–22(h) for comparison of the five $m=1$ moments, and Figs. 23(a)–23(e) for the five $m=2$ moments in the low-mass region. The s-channel $m=0$ moments also display the approximate regularity of Eq. (27b): see Fig. 24. Note that the A^2_{2n0} moments display minima near $-t=0.25$ GeV^2.

Thus, the $L=2$, $l=2$ moments are qualitatively consistent with S-wave dominance, and furthermore, helicity nonconservation is a strong feature of the S-wave contri-

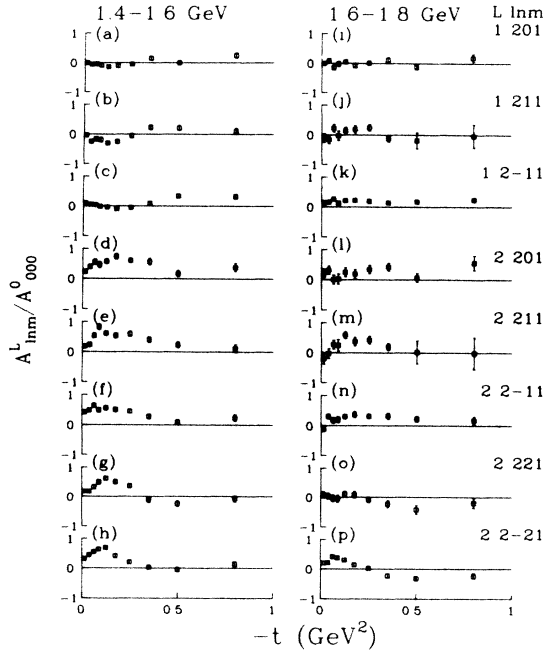

FIG. 22. s-channel A^L_{lnm}/A^0_{000} moments with $m=1$ plotted against t, labeled as in Fig. 20.

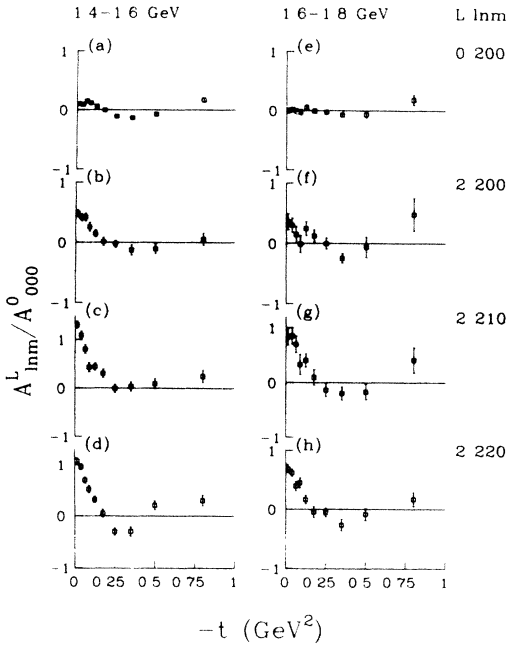

FIG. 24. s-channel A^L_{lnm}/A^0_{000} moments with $m=0$ plotted against t, labeled as in Fig. 19.

butions to the s-channel moments. The moments in Eq. (27) reflect this S wave dominance, and allow us to test the Berger-Pirilä[31] hypothesis by "solving" for the $\lambda_s=\pm\frac{1}{2}$ and $\pm\frac{3}{2}$ S waves, e.g.,

$$|S^1|^2+|S^{-1}|^2=\frac{fA^0_{000}}{2}+\frac{A^2_{210}}{8}+\frac{A^2_{220}}{8}\ , \tag{28a}$$

$$|S^3|^2+|S^{-3}|^2=\frac{fA^0_{000}}{2}-\frac{A^2_{210}}{8}-\frac{A^2_{220}}{8}\ , \tag{28b}$$

where the averaging reduces some small P-wave contributions, and the factor $f\approx 0.65$ takes approximate account of non-S-wave contributions to A^0_{000}, as estimated from the partial-wave analysis. The resulting $\lambda_s=\pm\frac{1}{2}$ S-wave intensity, expressed as a function of the total S-wave cross section, is plotted against t in Fig. 25(a), for $1.3<M<1.5$ GeV; it displays a clear minimum near $-t=0.25$ GeV^2, coincident with the break in $d\sigma/dt$. The simplest interpretation of Fig. 25(a) is that S^1, which must dominate at $t=0$ due to angular-momentum conservation, vanishes at the dip location, leaving S^{-1} and $S^{\pm 3}$ to fill in the cross section. This causes a break in $d\sigma/dt$ and a dip in the $\lambda_s=\pm\frac{1}{2}$ fraction. It is easy to show from consideration of the crossing relations, that this behavior is consistent with $\lambda_t=\frac{1}{2}$ dominance; Fig. 25(b) shows the $\lambda_t=\pm\frac{1}{2}$ fraction deduced from Eq. (28), and this appears to be quite large over the full t range. Repeating this exercise in finer mass bins, we find that the dip location in the $\lambda_s=\pm\frac{1}{2}$ fraction moves from ~ 0.22 GeV^2 to ~ 0.36 GeV^2 over the mass range 1350 to 1700 MeV. This is not inconsistent with the behavior of the break in $d\sigma/dt$ in Fig. 17. For comparison, Berger and Pirilä computed an outward movement from 0.29 GeV^2 to 0.43 GeV^2 for $N\to N\pi$ DD over the mass range 1100 to 1500 MeV.

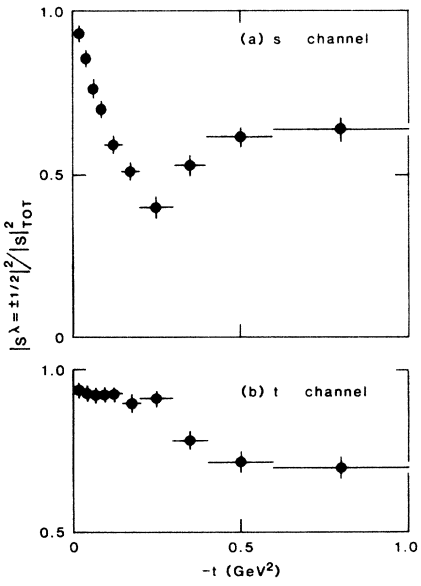

FIG. 25. Helicity $\pm\frac{1}{2}$ S-wave fractions, relative to total S-wave cross section, estimated as in Eq. (28), for (a) s channel and (b) t channel, for $1.3<M_{p\pi^+\pi^-}<1.5$ GeV.

C. Evidence for non-S-wave effects and helicity nonconservation

Pure S-wave production is, of course, only an approximation, and the moments indicate both the presence of $P,D,\ldots$ waves in addition to the $\Delta\pi$ S wave, and also non-S-wave contributions to helicity nonconservation. The various $l=0$ moments would all vanish (except A^0_{000}), if only S wave were present. These are shown in the t-channel frame, for two mass intervals, in Fig. 26. Note that in the low-mass region, the $m=2$ moments (which involve products of helicity-flip or double-flip amplitudes) are small [Figs. 26(e) and 26(h)], while the $m=1$ moments are comparable to the $m=0$ moments. Our partial-wave fits suggest that the t-channel helicity-flip amplitudes are small and do not contribute much in quadrature, as evidenced by the $m=2$ moments. In the s channel (Fig. 27), helicity conservation is again a much worse approximation; here the $m=2$ moments [Figs. 27(e), 27(h), 27(m), and 27(p)] are comparable with the $m=0$ moments, and the $m=1$ moments tend to be quite large.

The $l=0$ moments shown in Figs. 26 and 27 have the convenient property that they integrate over the Δ^{++} decay distribution, and hence give the projected distributions in Φ. Because all the t-channel $m=1$ moments are positive [Figs. 26(b), 26(d), and 26(g)] in the low-mass region, $\Phi_t=180°$ is favored over $\Phi_t=0°$ for forward decays ($\cos\Theta_t>0$). For backward decays, the large contribution from A^2_{001} [Fig. 26(d)] changes sign, due to the properties of the d functions in Eq. (26), and consequently the Φ_t distribution must become flatter in the $\cos\Theta_t<0$ hemisphere. These same regularities are seen in $N\to N\pi$ disso-

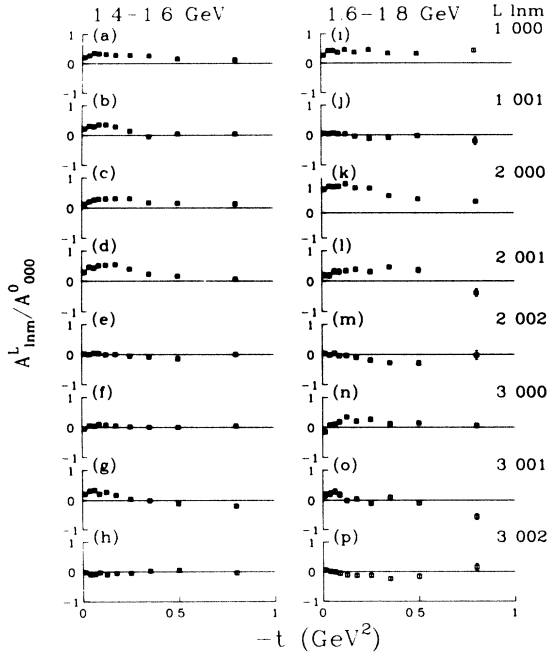

FIG. 26. t-channel A^L_{lnm}/A^0_{000} moments with $l=0$, plotted against t, for low-mass (a)—(h) and high-mass (i)—(p) bins: (a), (i) A^1_{000}; (b), (j) A^1_{001}; (c), (k) A^2_{000}; (d), (l) A^2_{001}; (e), (m) A^2_{002}; (f), (n) A^3_{000}; (g), (o) A^3_{001}; (h), (p) A^3_{002}.

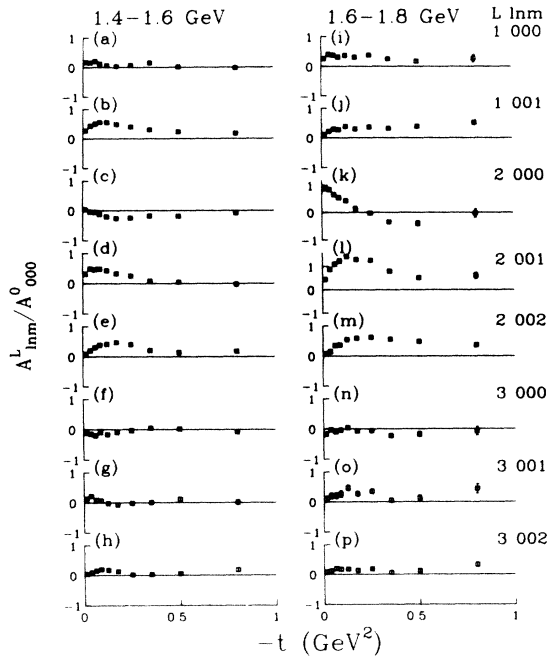

FIG. 27. s-channel A^L_{lnm}/A^0_{000} moments with $l=0$ plotted against t, labeled as in Fig. 26.

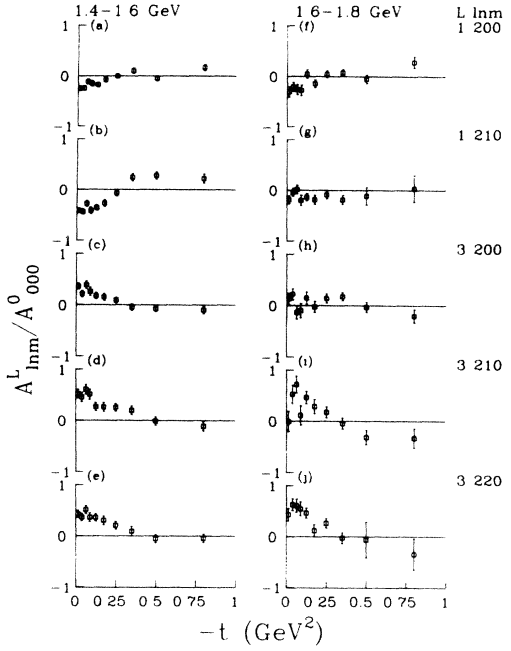

FIG. 28. t-channel A^L_{lnm}/A^0_{000} moments with $l=2$, $m=0$, plotted against t, for low-mass (a)–(e) and high-mass (f)–(j) bins: (a), (f) A^1_{200}; (b), (g) A^1_{210}; (c), (h) A^3_{200}; (d), (i) A^3_{210}; (e), (j) A^3_{220}.

ciation data,[1–3,7,8] and in $p\to p\pi^+\pi^-$ at $\sqrt{s}=53$ GeV.[7] Note that the $m=1$ t channel moments persist for high-L values, $L=3$ [Fig. 26(g)] and $L=4$ (not shown). This feature is evident in the data of Biel *et al.*,[2] on $n\to p\pi^-$, and corresponds to the fact that the Φ_t dependence is strongest very close to $\cos\Theta_t\approx+1$, as shown also by the isocline analysis of reaction (1) by Goggi *et al.*[7] The Φ_s projections, as evidenced by the $m=1$ moments in Fig. 27, should be qualitatively similar to those for Φ_t, albeit more pronounced.

These qualitative features of the projected Φ dependence have been explained as kinematical reflections of pion- and nucleon-exchange Deck amplitudes,[28–30] and Biel *et al.*[2] have presented quantitative comparisons with these predictions for $n\to p\pi^-$ dissociation. In the pion-exchange Deck model, the Φ_t projection reflects the dependence on the $(p_r\pi^-)$ mass in the Chew-Low formula, Eq. (20); the Φ_s projection reflects the pion propagator in Eq. (20). Both kinematical effects favor $\Phi_{s,t}=180°$ over $\Phi_{s,t}=0°$. Nucleon exchange (presumably important for $\cos\Theta<0$), would have analogous features, but would favor $\Phi=0°$. Given the complexity in L of the $l=0$ moments, it could be argued that the Deck model offers a more economical description of the data than would a partial-wave representation.

For completeness, we show the t dependence of the remaining $l=2$ moments in Fig. 28 (t channel) and Fig. 29 (s channel), for $m=0$ and odd L. These moments are qualitatively consistent with the pattern expected for S-P interference terms; with only helicity-conserving S and P waves in $p\pi^\pm\pi^-$ the moments expansion is such that we would have $A^1_{210}=\sqrt{3}A^1_{200}$ [cf. Figs. 28(a) and 28(b)], and we would obtain like signs for the A^3_{200}, A^3_{210}, and A^3_{220} moments [Figs. 28(c)–28(e)] irrespective of the mix of P waves involved ($\frac{1}{2}^+$, $\frac{3}{2}^+$, and $\frac{5}{2}^+$ are allowed).

D. Helicity-nonconserving spin correlations

In Sec. V we will discuss the helicity-conserving spin-correlation moments, in connection with the partial-wave

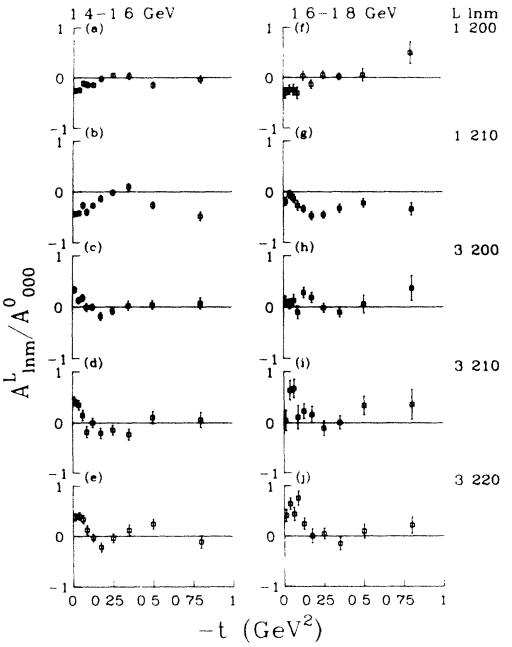

FIG. 29. s-channel A^L_{lnm}/A^0_{000} moments with $l=2$, $m=0$, plotted against t, labeled as in Fig. 28.

analysis. In this section we review the t-channel helicity-nonconserving correlations. We remark that, whereas the helicity nonconservation (i.e., Φ dependence) in the unpolarized cross section may have a simple kinematical interpretation in the Deck model, helicity nonconservation in the polarized observables requires the flip and nonflip amplitudes to be out of phase. This is clearly not a kinematical effect, and would not occur in a pure pion-exchange model without new features such as Reggeization or absorption.

Figure 30 shows the $l=0$ t-channel transverse polarizations, including the overall production asymmetry, B^0_{000} [Figs. 30(a) and 30(e)], in two mass intervals. The production asymmetry is small ($\sim\pm 15\%$), comparable to that seen in elastic scattering at these energies. Figure 31 shows the $l=0$, $m=1$ helicity-nonconserving longitudinal spin correlations. If only S waves were present, all of the correlations in Figs. 30 and 31 would vanish except B^0_{000}, given by

$$B^0_{000} = -2\,\mathrm{Im}(S^{1*}S^{-1} - S^{3*}S^{-3})\,. \tag{29}$$

The observed moments require S-P and P-P interferences of order 20%.

The $l=2$ spin correlations for $1.4 < M_{p\pi^+\pi^-} < 1.6$ GeV are shown in Figs. 32–34. Again, if only S waves were present, all the $L=1$ B terms (Fig. 32) and $L=1$ C terms [Figs. 34(a)–34(c)] would vanish; this may not be a bad approximation. The $L=2$ B coefficients would have the property that all the $m=0$ moments [Figs. 33(a)–33(e)] would be identical, and also all of the $m=2$ moments [Figs. 33(f)–33(j)] would be identical, again not a disastrous approximation. The $L=2$ C coefficients [Figs. 34(d)–34(h)] would also be identical for pure S wave, but this does not appear to be true.

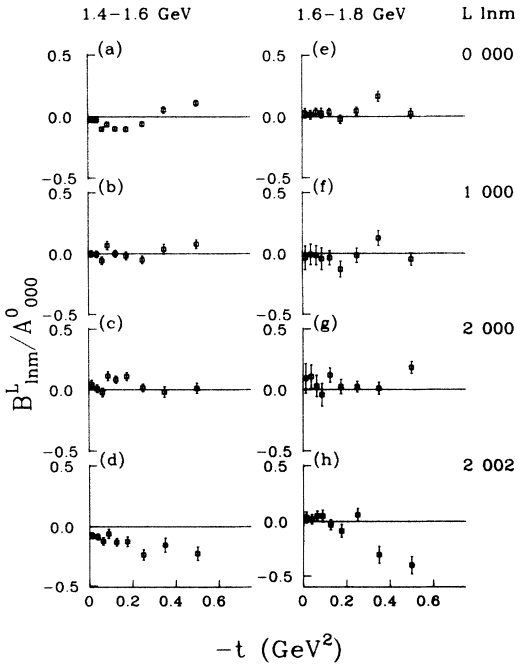

FIG. 30. Transverse-polarization moments B^L_{lnm}/A^0_{000} with $l=0$ and $m=0,2$ plotted against t, for low-mass (a)–(d) and high-mass (e)–(h) bins: (a), (e) B^0_{000}; (b), (f) B^1_{000}; (c), (g) B^2_{000}; and (d), (h) B^2_{002}.

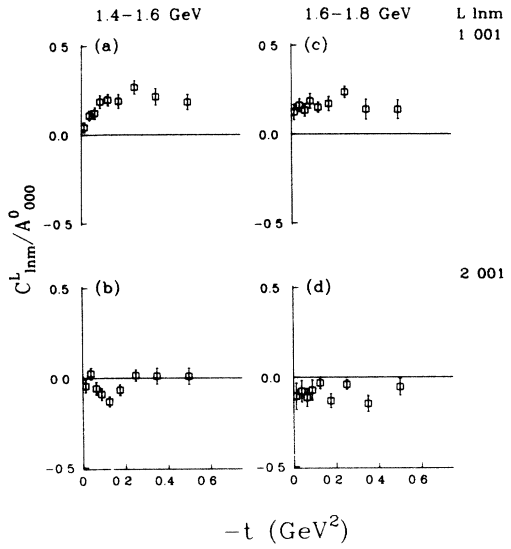

FIG. 31. Longitudinal-polarization moments with $m=1$, plotted against t, for low-mass (a), (b) and high-mass (c), (d) bins: (a), (c) C^1_{001}; and (b), (d) C^2_{001}.

As discussed in Sec. IV A, the $l=1$ moments require interference between waves with differing j^P for the $(p\pi^+)$ system, e.g., s-Δ interference. Such interferences are expected in the Deck process of Fig. 11(a), which would give rise to polarizations as in $\pi^+ p$ elastic scattering. Such effects are seen clearly in the charge-exchange reaction, $p_\uparrow p \to p\pi^+ n$.[47] Of course there can be other sources of s-isobar production, such as $p\epsilon$ and $N^*\pi^+$ isobars. In any case, the Δ^{++} Breit-Wigner phase can, in principle, cause large polarization effects in consort with these back-

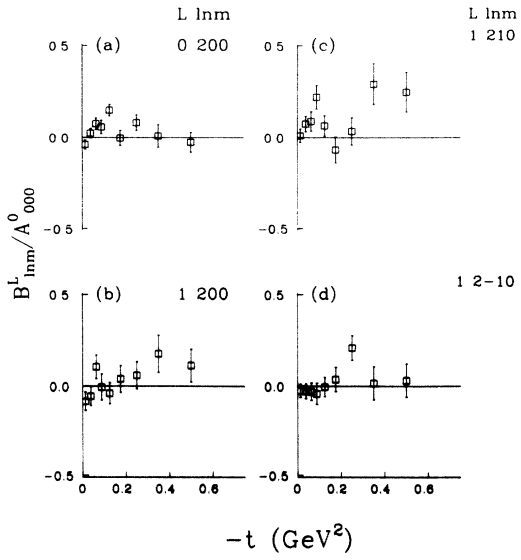

FIG. 32. Transverse-polarization moments with $L=1$, $l=2$, $m=0$, plotted against $-t$, for low-mass (a), (b), and high-mass (c), (d) bins: (a), (c) B^1_{210}, and (b), (d) B^1_{2-10}.

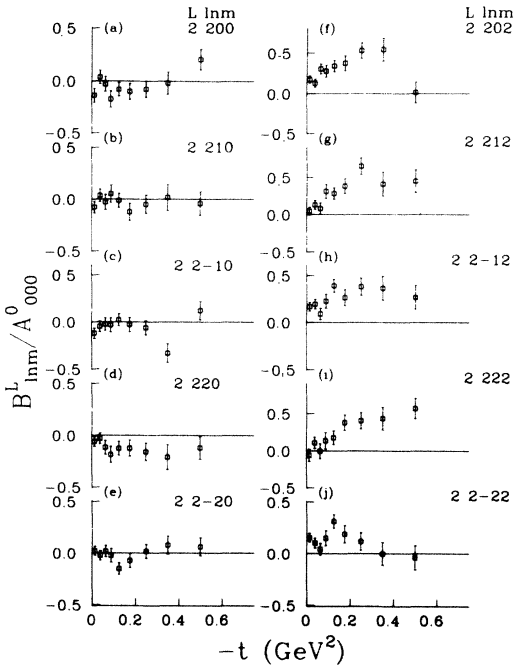

FIG. 33. Transverse-polarization moments with $L=2$, $l=2$, $m=0,2$ plotted against t, for $1.4 < M_{p\pi^+\pi^-} < 1.6$ GeV.

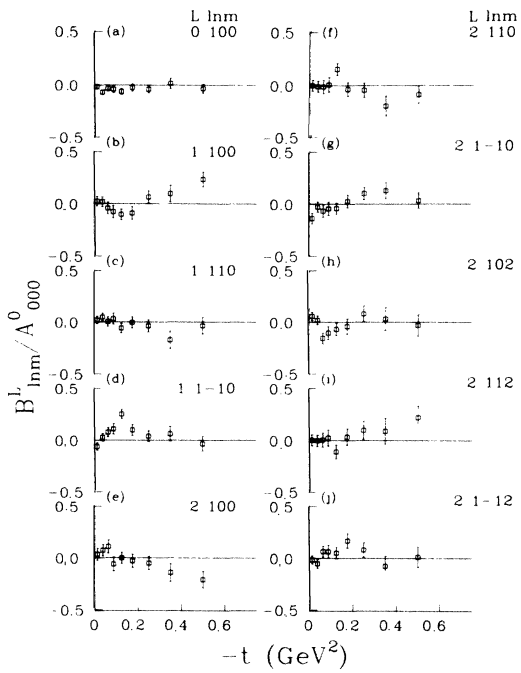

FIG. 35. Transverse-polarization moments with $l=1$, $m=0,2$, plotted against t, for $1.4 < M_{p\pi^+\pi^-} < 1.6$ GeV.

ground $p\pi^+$ s waves. The helicity-nonconserving $l=1$ spin correlations are shown in Figs. 35 (B^L_{lnm}) and 36 (C^L_{lnm}). Some large asymmetries are seen, especially in the C coefficients [Figs. 36(d) and 36(e)].

E. The $N(1700)$ enhancement

We have used the corrected mass spectra in three t intervals (Fig. 37) to extract the t dependence for the $N(1700)$ signal, cut on the Δ^{++} band:

$$\frac{d\sigma}{dt}(N(1700))_{\Delta^{++}\text{cut}} = (156\pm16)e^{4.0\pm0.5t}\ \mu\text{b/GeV}^2 \ . \tag{30}$$

Using in addition the raw spectra of Figs. 7, 13, and 14, we can estimate the $p\pi^+\pi^-$ and $\Delta^{++}\pi^-$ mode cross sections:

$$\sigma(N(1700)\to p\pi^+\pi^-) = 83\pm12\ \mu\text{b} \ , \tag{31a}$$

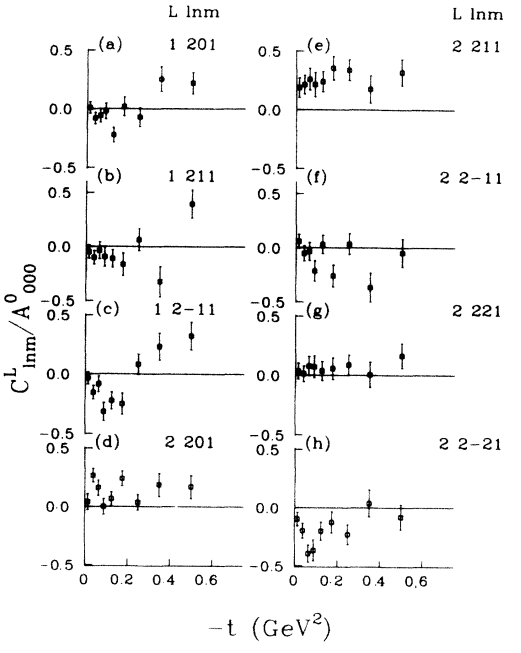

FIG. 34. Longitudinal polarization moments with $l=2$, $m=1$, plotted against t, for $1.4 < M_{p\pi^+\pi^-} < 1.6$ GeV.

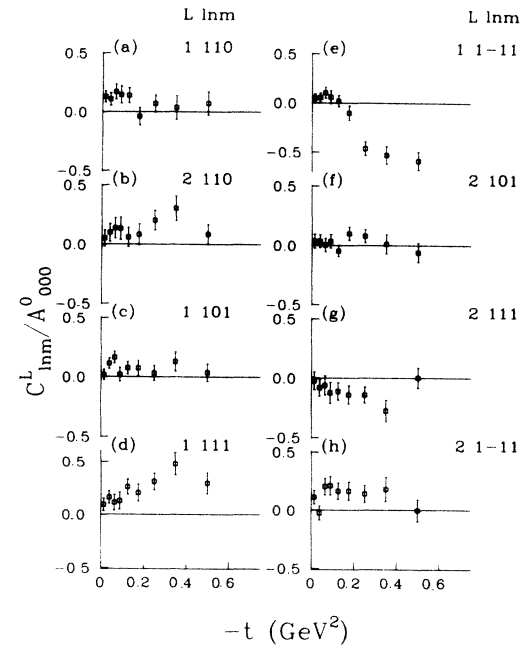

FIG. 36. Longitudinal-polarization moments with $l=1$, $m=0,1$, plotted against t, for $1.4 < M_{p\pi^+\pi^-} < 1.6$ GeV.

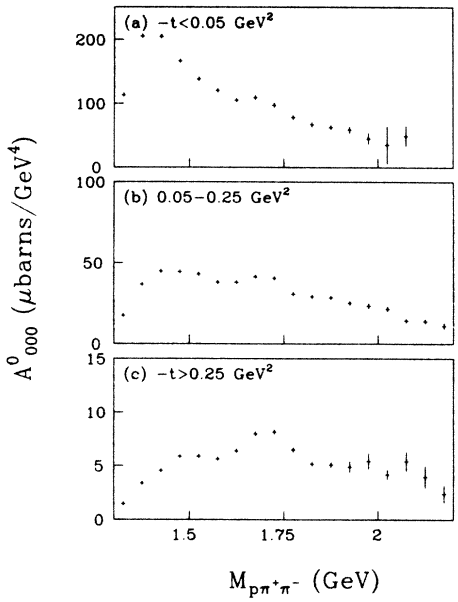

FIG. 37. A^0_{000} cross-section coefficient plotted against $M_{p\pi^+\pi^-}$ for three t intervals: (a) $-t<0.05$ GeV^2, (b) $0.05<-t<0.25$ GeV^2, and (c) $-t>0.25$ GeV^2. Note that $A^0_{000}=(1/16\pi^2)d^3\sigma/dt\,dM_{p\pi^+\pi^-}dM_{p\pi^+}$.

$$\sigma(N(1700)\to\Delta^{++}\pi^-)=39\pm6\ \mu\text{b}\ . \tag{31b}$$

(The $\Delta^{++}\pi^-$ cross section happens to be equal to the Δ^{++}-cut cross section; the Δ^{++}-cut cross section excludes part of the $\Delta^{++}\pi^-$ mode but includes non-Δ^{++} background.) The above estimates, which include a factor of 2 for target dissociation in both (30) and (31), are based on a linear-background subtraction for the signal in $1.60<M_{p\pi^+\pi^-}<1.80$ GeV; the background was obtained from a cross-section average outside of this cut. This definition is reasonable, given the shape of the mass spectra in Fig. 37, but tends to underestimate the signal as compared with a Breit-Wigner form plus background fit.

Missing-mass experiments[48,49] have confirmed that the differential cross section for

$$pp\to p[N(1700)\to\text{all}] \tag{32}$$

is a single exponential for $-t<1$ GeV^2, consistent with our exclusive data. Averaged between 9.9 and 15.1 GeV/c, the data of Edelstein *et al.*[48] give

$$\frac{d\sigma}{dt}(N(1700)\to\text{all})=(3540\pm300)e^{4.45\pm0.17t}\ \mu\text{b/GeV}^2\ , \tag{33}$$

so that the t slopes in (30) and (33) are consistent [(33) includes beam and target dissociation.] If we postulate that the $N(1700)$ represents a single $I=\frac{1}{2}$ state, then (31) and (33) together give $[N(1700)\to\Delta\pi]/[N(1700)\to\text{all}]=0.10\pm0.02$. This branching ratio is consistent with the properties of the $\frac{5}{2}^+$ $F15$ resonance ($\Delta\pi/\text{all}\approx0.12$), but altogether inconsistent with the $\frac{5}{2}^-$ $D15$ state ($\Delta\pi/\text{all}\approx0.55$).[50] We note that our partial-wave analysis (PWA) admits very little $\frac{5}{2}^-$ production in the $N(1700)$ region.

Webb *et al.*[15] reported cross sections for reaction (1) at $\sqrt{s}=45$ GeV (1080 GeV/c):

$$\frac{d\sigma}{dt}((1700)\to p\pi^+\pi^-)=(1197\pm378)e^{6.3\pm0.4t}\ \mu\text{b/GeV}^2\ . \tag{34}$$

Their $N(1700)$ cross section is larger than ours, 190 ± 60 μb compared with 83 ± 12 μb, but was obtained by fitting the entire production cross section for reaction (1) to $N(1520)$ plus $N(1700)$. If we estimate the $\sqrt{s}=45$ $N(1700)$ signal in the same manner as for our own data, we obtain $\sigma(N1700\to p\pi^+\pi^-)=47\pm15$ μb. Comparison of the slopes at 11.75 and 1080 GeV/c yields $\alpha'_{\text{eff}}=0.25\pm0.08$ GeV^{-2}, consistent with the estimate given by Edelstein *et al.*,[48] for the range 9.9–29 GeV/c, namely, $\alpha'_{\text{eff}}=0.38\pm0.17$ GeV^{-2}. Using our estimate of the ISR signal cross section, we further obtain $\alpha_{\text{eff}}(t=0)=0.98\pm0.09$ GeV^{-2}. Taken together, these data are consistent with a common origin for the $N(1700)$ bump seen in various experiments, and suggest a Pomeron-type production mechanism.

F. Summary

In this section we have examined the t dependence of the cross section and angular distribution moments. The slope-mass correlation and the cross section break near $-t=0.25$ GeV^2 are similar to what is seen in higher energy DD processes, both for $N\to N\pi$ and $p\to p\pi^+\pi^-$. Using the Δ^{++} decay as an analyzer (the $l=2$ moments), we showed that the moments are consistent with S-wave dominance at low masses, and that the cross-section break coincides with a strong minimum in the s-channel helicity$=\pm\frac{1}{2}$ S-wave cross section, consistent with the peripheral model proposed by Berger and Pirilä.[31] We pointed out that the moments are inconsistent with a dominant $\frac{1}{2}^+$ mode for the low-mass enhancement. We showed that the pattern of helicity nonconservation in the unpolarized cross section is similar to what is observed in $N\to N\pi$ and $p\to p\pi^+\pi^-$ at higher energies, and what is expected qualitatively within the Deck model. We showed that helicity conservation is a better approximation in the t channel, especially for those moments which have pure S-wave contributions; there are, however, helicity-nonconserving t-channel contributions involving S-P, P-P, and P-D interferences. We observed that the overall pattern of helicity nonconservation, as manifested by the spin correlations, is somewhat complex, and requires flip-nonflip interferences in S-S, S-P, and P-P combinations and between non-Δ^{++} and Δ^{++} waves. Finally we noted that the t dependence for $N(1700)$ production is quite similar in the $p\pi^+\pi^-$ and the inclusive decay modes, and that the energy dependence is Pomeron-type; finally, the decay branching ratios appear consistent with $\frac{5}{2}^+$ but not $\frac{5}{2}^-$.

V. PARTIAL-WAVE ANALYSIS

A. Assumptions

We have performed spin-parity analysis on the t-channel moments in the Δ^{++} band in 50-MeV $M_{p\pi^+\pi^-}$

bins, for the two t intervals, $-t<0.25$ GeV^2 and $0.25<-t<0.80$ GeV^2 (small t and large t). We included all $\Delta^{++}\pi^-$ waves with $L=0$, 1, 2, and $\lambda=\frac{3}{2},\frac{1}{2},-\frac{1}{2}$ in the t channel [Δ^{++} in this context means a $J^P=\frac{3}{2}^+$ ($p\pi^+$) system]. We included non-Δ^{++} background waves with $J^P=\frac{1}{2}^{\pm}$ in the ($p\pi^+$) subsystem, with $L=0$, 1 and $\lambda=\frac{3}{2},\frac{1}{2},-\frac{1}{2}$. We assumed pure natural-parity exchange and ignored possible incoherence effects involving the target-recoil proton helicities; in the notation of the Appendix, we retained N^{λ}_{++} production amplitudes. Table I lists the expressions for the helicity-conserving moments in terms of these amplitudes; for illustrative purposes we have shown only the $\lambda=\frac{1}{2}$ $\Delta^{++}\pi^-$ contributions, but more extensive tables are available from the authors. As explained in the Appendix, unnatural-parity exchange amplitudes do not interfere with the natural-parity waves; their observables would have formally the same structure as given by Table I, except for an overall sign reversal on all transverse-polarization B^L_{lnm} coefficients. At some level, there should be an unnatural-parity contribution from π^0 exchange, involving off-shell $\pi^0 p_\uparrow\to\pi^+\pi^- p$, and this is in principle calculable;[51] one would anticipate a $<10\%$ effect from this source. We have tried to check for this kind of effect by looking for energy dependence in the transverse polarizations, using our sample of 6-GeV/c data; the energy dependence appears to be small, as discussed below. In any case, the gross similarities between the ISR data and ours, both for the Deck background and the $N(1700)$ production, suggest that natural-parity exchange is dominant. We remark that in their analysis of reaction (1), Idschok *et al.*[22] made similar assumptions—namely, spin coherence at the recoil-proton vertex and pure naturality exchange (these assumptions are trivially correct for analyses using $\pi^{\pm}p$ and $K^{\pm}p$ data[23–26]). Some analyses have made further assumptions (cf. Refs. 21 and 22) such as exact helicity conservation and the Gribov-Morrison (GM) rule, $J^P=\frac{1}{2}^+,\frac{3}{2}^-,\frac{5}{2}^+,\ldots$. Parenthetically, we regard any successes of the GM rule as accidental; it is inconsistent with S-wave dominance in $N\to N\pi$ DD,[6] and should not be taken as a starting point in the partial-wave analysis (PWA).

B. Mass dependence of the unpolarized moments

Next we examine the mass dependence of the moments to identify features which dictate the partial-wave solutions and which might reveal more about the nature of the $N(1700)$. Since the latter is much more prominent at large t, we emphasize differences between the moments spectra in the two t bins. As discussed above, the even-L, $l=2$ moments are especially sensitive to the relative S- and P-wave intensities. These t channel moments are shown in Fig. 38 for the two t intervals, together with the partial-wave fits. We can read off the relative amount of S wave, since (cf. Sec. IV B)

$$2a^2_{200}=A^2_{210}=A^2_{220}=2A^0_{000}\ , \tag{35}$$

for pure $\lambda_t=\frac{1}{2}$ S wave. Inspection of Figs. 38(c)–38(e) suggests that the S-wave intensity ranges from $\sim 65\%$ near threshold to $\sim 40\%$ in the $N(1700)$ region. For the large-t bin, the S-wave intensity appears systematically lower [Figs. 38(h)–38(j)] and there are major deviations from Eq. (35) in the $N(1700)$ region, where $A^2_{210}\neq A^2_{220}$.

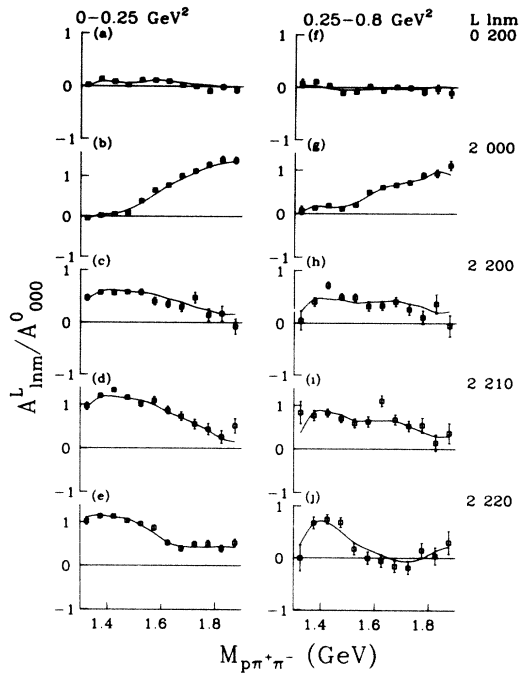

FIG. 38. t channel A^L_{lnm}/A^0_{000} with L even, $m=0$, plotted against mass for small-t (a)–(e) and large-t (f)–(j) bins: (a), (f) A^0_{200}; (b), (g) A^2_{000}; (c), (h) A^2_{200}; (d), (i) A^2_{210}; and (e), (j) A^2_{220}. The curves show the partial-wave fits, which have been joined bin to bin for clarity.

We consider these moments in succession. First, A^0_{200} [Figs. 38(a) and 38(f)] is close to zero for both t bins and all masses. Ignoring S-D interferences, we have

$$A^0_{200}=|P_1|^2-0.80|P_3|^2+0.20|P_5|^2\ , \tag{36}$$

where $P_{1,3,5}$ refer to the $J^P=\frac{1}{2}^+$, $\frac{3}{2}^+$, and $\frac{5}{2}^+$, $\lambda_t=\frac{1}{2}$ P-wave $\Delta^{++}\pi^-$ amplitudes (see Table I). Thus, if $N(1700)$, which makes up $\sim 35\%$ of the cross section at its maximum in the large-t bin, were a pure state, it could not be P_1 or P_3. It could be an equal mix of P_1 and P_3, or it could be pure P_5 or pure S_3 [the contribution of $|P_5|^2$ to A^0_{200}/A^0_{000} would be only ~ 0.08 at the $N(1700)$ maximum]. Recall that we used the same information in Sec. IV B to dispose of P_1 as the main source of the threshold enhancement.

The moment A^2_{000} [Figs. 38(b) and 38(g)] also has no S-wave contribution. It is small around the threshold enhancement, and rises monotonically above 1.5 GeV. The ratio A^2_{000}/A^0_{000} is systematically smaller in the large-t bin; it is $\sim 64\%$ of the small-t value, around $N(1700)$. Neglecting S-D interference, we have

$$A^2_{000}=0.80|P_5|^2-0.80|P_3|^2-0.89P^*_1P_3 +1.20P^*_3P_5-2.68P^*_1P_5\ . \tag{37}$$

Again, suppose the $N(1700)$ were a pure state making up $\sim 35\%$ of the cross section at its maximum at large t versus 20% at small t, and suppose the P-wave interfer-

TABLE I. Joint moments A^L_{lnm}, B^L_{lnm}, C^L_{lnm} in terms of helicity-conserving S-, P-, and D-wave $\Delta^{++}\pi^-$ production amplitudes. The notation for the amplitude products, $a_i^* a_j$, is an abbreviation for $\mathrm{Re}(a_k^* a_j)$ for the A^L_{lnm} moments, and $\mathrm{Im}(a_i^* a_j)$ or the B^L_{lnm} and C^L_{lnm} moments. The B^L_{lnm} are given for natural-parity exchange; for unnatural-parity exchange contributions, the B^L_{lnm} have opposite sign. The partial-wave notation denotes the L and J values; for example, $S3$ denotes the $\frac{3}{2}^-$ S wave, $P1$ the $\frac{1}{2}^+$ P wave, etc. The moments in the left-hand column are obtained by summing over the partial-wave products weighted by the indicated coefficients.

A^0_{000}	1.00	$(P1^*P1)$	1.00	$(D1^*D1)$	1.00	$(S3^*S3)$
	1.00	$(P3^*P3)$	1.00	$(D3^*D3)$	1.00	$(P5^*P5)$
	1.00	$(D5^*D5)$	1.00	$(D7^*D7)$		
A^0_{200}	1.00	$(P1^*P1)$	1.00	$(D1^*D1)$	−0.80	$(P3^*P3)$
	−2.00	$(S3^*D3)$	0.20	$(P5^*P5)$	−0.71	$(D5^*D5)$
	0.29	$(D7^*D7)$				
A^1_{000}	2.00	$(P1^*D1)$	−2.00	$(P1^*S3)$	−0.89	$(D1^*P3)$
	0.89	$(S3^*P3)$	2.00	$(P1^*D3)$	0.72	$(P3^*D3)$
	2.68	$(S3^*P5)$	−0.54	$(D3^*P5)$	2.46	$(P3^*D5)$
	0.35	$(P5^*D5)$	2.87	$(P5^*D7)$		
A^1_{200}	2.00	$(P1^*D1)$	−2.00	$(P1^*S3)$	−0.89	$(D1^*P3)$
	−0.72	$(S3^*P3)$	2.00	$(P1^*D3)$	−0.89	$(P3^*D4)$
	0.54	$(S3^*P5)$	−2.68	$(D3^*P5)$	−1.75	$(P3^*D5)$
	−0.25	$(P5^*D5)$	0.82	$(P5^*D7)$		
A^1_{210}	−3.46	$(P1^*S3)$	−4.65	$(D1^*P3)$	−1.24	$(S3^*P3)$
	−3.46	$(P1^*D3)$	0.62	$(P3^*D3)$	0.93	$(S3^*P5)$
	−2.79	$(D3^*P5)$	0.61	$(P3^*D5)$	−0.93	$(P5^*D5)$
	0.71	$(P5^*D7)$				
A^2_{000}	−2.00	$(D1^*S3)$	−0.89	$(P1^*P3)$	−0.80	$(P3^*P3)$
	2.00	$(D1^*D3)$	−2.00	$(S3^*D3)$	−2.68	$(P1^*P5)$
	1.20	$(P3^*P5)$	0.80	$(P5^*P5)$	−1.31	$(D1^*D5)$
	1.31	$(S3^*D5)$	0.93	$(D3^*D5)$	0.41	$(D5^*D5)$
	3.21	$(S3^*D7)$	−0.92	$(D3^*D7)$	0.60	$(D5^*D7)$
	1.02	$(D7^*D7)$				
A^2_{200}	−2.00	$(D1^*S3)$	1.00	$(S3^*S3)$	−0.89	$(P1^*P3)$
	1.00	$(P3^*P3)$	2.00	$(D1^*D3)$	1.00	$(D3^*D3)$
	−2.68	$(P1^*P5)$	−0.86	$(P3^*P5)$	0.57	$(P5^*P5)$
	−1.31	$(D1^*D5)$	−0.94	$(S3^*D5)$	−1.31	$(D3^*D5)$
	−0.08	$(D5^*D5)$	0.92	$(S3^*D7)$	−3.21	$(D3^*D7)$
	−0.40	$(D5^*D7)$	0.51	$(D7^*D7)$		
A^2_{210}	−2.00	$(D1^*S3)$	2.00	$(S3^*S3)$	−2.68	$(P1^*P3)$
	1.20	$(P3^*P3)$	−2.00	$(D1^*D3)$	−2.00	$(D3^*D3)$
	−3.58	$(P1^*P5)$	−1.66	$(P3^*P5)$	1.37	$(P5^*P5)$
	−5.24	$(D1^*D5)$	−0.94	$(S3^*D5)$	−0.19	$(D3^*D5)$
	0.98	$(D5^*D5)$	0.92	$(S3^*D7)$	−3.67	$(D3^*D7)$
	−1.27	$(D5^*D7)$	1.02	$(D7^*D7)$		
A^2_{220}	4.00	$(D1^*S3)$	2.00	$(S3^*S3)$	−5.37	$(P1^*P3)$
	−1.20	$(P3^*P3)$	4.00	$(D1^*D3)$	−2.00	$(D3^*D3)$
	1.79	$(P1^*P5)$	−1.49	$(P3^*P5)$	2.06	$(P5^*P5)$
	−2.62	$(D1^*D5)$	1.87	$(S3^*D5)$	−1.12	$(D3^*D5)$
	−1.47	$(D5^*D5)$	−1.83	$(S3^*D7)$	0.46	$(D3^*D7)$
	−1.13	$(D5^*D7)$	2.04	$(D7^*D7)$		
A^3_{000}	−1.61	$(P3^*D3)$	−2.68	$(D1^*P5)$	−2.15	$(D3^*P5)$
	−1.31	$(P1^*D5)$	−1.87	$(P3^*D5)$	1.41	$(P5^*D5)$
	−3.21	$(P1^*D7)$	1.43	$(P3^*D7)$	1.43	$(P5^*D7)$

TABLE I. (*Continued*).

A^3_{200}	1.61	$(S3^*P3)$	−2.68	$(D1^*P5)$	2.15	$(S3^*P5)$
	−1.31	$(P1^*D5)$	2.34	$(P3^*D5)$	−0.78	$(P5^*D5)$
	−3.21	$(P1^*D7)$	−0.96	$(P3^*D7)$	1.43	$(P5^*D7)$
A^3_{210}	3.04	$(S3^*P3)$	−1.52	$(P3^*D3)$	−2.53	$(D1^*P5)$
	4.05	$(S3^*P5)$	0.51	$(D3^*P5)$	−3.70	$(P1^*D5)$
	2.65	$(P3^*D5)$	−0.88	$(P5^*D5)$	−3.78	$(P1^*D7)$
	−2.03	$(P3^*D7)$	3.04	$(P5^*D7)$		
A^3_{220}	2.40	$(S3^*P3)$	−4.80	$(P3^*D3)$	4.00	$(D1^*P5)$
	3.20	$(S3^*P5)$	1.60	$(D3^*P5)$	−5.86	$(P1^*D5)$
	−2.09	$(P3^*D5)$	0.70	$(P5^*D5)$	2.39	$(P1^*D7)$
	−2.14	$(P3^*D7)$	3.21	$(P5^*D7)$		
A^4_{000}	−2.24	$(D3^*D5)$	−0.98	$(D5^*D5)$	−3.21	$(D1^*D7)$
	−2.29	$(D3^*D7)$	1.50	$(D5^*D7)$	0.55	$(D7^*D7)$
A^4_{200}	2.06	$(P3^*P5)$	1.03	$(P5^*P5)$	2.24	$(S3^*D5)$
	1.22	$(D5^*D5)$	−3.21	$(D1^*D7)$	2.29	$(S3^*D7)$
	−0.68	$(D5^*D7)$	0.80	$(D7^*D7)$		
A^4_{210}	3.76	$(P3^*P5)$	1.88	$(P5^*P5)$	4.10	$(S3^*D5)$
	−2.05	$(D3^*D5)$	1.34	$(D5^*D5)$	−2.93	$(D1^*D7)$
	4.18	$(S3^*D7)$	0.84	$(D3^*D7)$	−0.92	$(D5^*D7)$
	1.65	$(D7^*D7)$				
A^4_{220}	2.66	$(P3^*P5)$	1.33	$(P5^*P5)$	2.90	$(S3^*D5)$
	−5.80	$(D3^*D5)$	−0.95	$(D5^*D5)$	4.14	$(D1^*D7)$
	2.96	$(S3^*D7)$	2.37	$(D3^*D7)$	0.04	$(D5^*D7)$
	1.55	$(D7^*D7)$				
B^1_{001}	2.83	$(P1^*D1)$	1.41	$(P1^*S3)$	−0.63	$(D1^*P3)$
	2.53	$(S3^*P3)$	−1.41	$(P1^*D3)$	−2.02	$(P3^*D3)$
	−1.90	$(S3^*P5)$	0.38	$(D3^*P5)$	1.74	$(P3^*D5)$
	1.49	$(P5^*D5)$	−2.03	$(P5^*D7)$		
B^1_{2-11}	1.22	$(P1^*S3)$	1.22	$(D1^*S3)$	−1.64	$(P1^*P3)$
	−1.64	$(D1^*P3)$	−1.75	$(S3^*P3)$	1.22	$(P1^*D3)$
	1.22	$(D1^*D3)$	1.96	$(S3^*D3)$	−0.88	$(P3^*D3)$
	−0.33	$(S3^*P5)$	−0.73	$P3^*P5)$	0.99	$(D3^*P5)$
	1.12	$(S3^*D5)$	0.22	$(P3^*D5)$	−0.80	$(D3^*D5)$
	−1.97	$(P5^*D5)$	−0.25	$(P5^*D7)$	−0.86	$(D5^*D7)$
B^1_{201}	2.83	$(P1^*D1)$	1.41	$(P1^*S3)$	−0.63	$(D1^*P3)$
	−2.02	$(S3^*P3)$	−1.41	$(P1^*D3)$	2.53	$(P3^*D3)$
	−0.38	$(S3^*P5)$	1.90	$(D3^*P5)$	−1.24	$(P3^*D5)$
	−1.06	$(P5^*D5)$	−0.58	$(P5^*D7)$		
B^1_{211}	1.22	$(P1^*S3)$	−1.22	$(D1^*S3)$	1.64	$(P1^*P3)$
	−1.64	$(D1^*P3)$	−1.75	$(S3^*P3)$	1.22	$(P1^*D3)$
	−1.22	$(D1^*D3)$	−1.96	$(S3^*D3)$	−0.88	$(P3^*D3)$
	−0.33	$(S3^*P5)$	0.73	$(P3^*P5)$	0.99	$(D3^*P5)$
	−1.12	$(S3^*D5)$	0.22	$(P3^*D5)$	0.80	$(D3^*D5)$
	−1.97	$(P5^*D5)$	−0.25	$(P5^*D7)$	0.86	$(D5^*D7)$
B^2_{001}	2.45	$(D1^*S3)$	−1.10	$(P1^*P3)$	−2.45	$(D1^*D3)$
	2.19	$(P1^*P5)$	−2.45	$(P3^*P5)$	−1.07	$(D1^*D5)$
	2.67	$(S3^*D5)$	1.91	$(D3^*D5)$	−2.62	$(S3^*D7)$
	0.75	$(D3^*D7)$	−1.71	$(D5^*D7)$		

TABLE I. (*Continued*).

B^2_{2-21}	2.45	$(P1^*S3)$	−2.45	$(D1^*S3)$	−3.29	$(P1^*P3)$
	3.29	$(D1^*P3)$	2.45	$(P1^*D3)$	−2.45	$(D1^*D3)$
	−0.73	$(P1^*P5)$	0.73	$(D1^*P5)$	−1.83	$(S3^*P5)$
	1.52	$(P3^*P5)$	0.26	$(D3^*P5)$	1.07	$(P1^*D5)$
	−1.07	$(D1^*D5)$	1.91	$(S3^*D5)$	−1.20	$(P3^*D5)$
	−1.15	$(D3^*D5)$	0.75	$(S3^*D7)$	−0.59	$(P3^*D7)$
	−0.19	$(D3^*D7)$	−1.76	$(P5^*D7)$	1.62	$(D5^*D7)$
B^2_{2-11}	1.22	$(P1^*S3)$	1.22	$(D1^*S3)$	−1.64	$(P1^*P3)$
	−1.64	$(D1^*P3)$	1.22	$(P1^*D3)$	1.22	$(D1^*D3)$
	1.46	$(P1^*P5)$	1.46	$(D1^*P5)$	−0.91	$(S3^*P5)$
	1.69	$(P3^*P5)$	−1.43	$(D3^*P5)$	−2.14	$(P1^*D5)$
	−2.14	$(D1^*D5)$	−0.95	$(S3^*D5)$	0.60	$(P3^*D5)$
	−0.19	$(D3^*D5)$	−0.37	$(S3^*D7)$	−1.17	$(P3^*D7)$
	1.50	$(D3^*D7)$	−0.59	$(P5^*D7)$	1.81	$(D5^*D7)$
B^2_{201}	2.45	$(D1^*S3)$	−1.10	$(P1^*P3)$	−2.45	$(D1^*D3)$
	2.19	$(P1^*P5)$	1.75	$(P3^*P5)$	−1.07	$(D1^*D5)$
	−1.91	$(S3^*D5)$	−2.67	$(D3^*D5)$	−0.75	$(S3^*D7)$
	2.62	$(D3^*D7)$	1.14	$(D5^*D7)$		
B^2_{211}	−1.22	$(P1^*S3)$	1.22	$(D1^*S3)$	−1.64	$(P1^*P3)$
	1.64	$(D1^*P3)$	−1.22	$(P1^*D3)$	1.22	$(D1^*D3)$
	1.46	$(P1^*P5)$	−1.46	$(D1^*P5)$	0.91	$(S3^*P5)$
	1.69	$(P3^*P5)$	1.43	$(D3^*P5)$	2.14	$(P1^*D5)$
	−2.14	$(D1^*D5)$	−0.95	$(S3^*D5)$	−0.60	$(P3^*D5)$
	−0.19	$(D3^*D5)$	−0.37	$(S3^*D7)$	1.17	$(P3^*D7)$
	1.50	$(D3^*D7)$	0.59	$(P5^*D7)$	1.81	$(D5^*D7)$
B^2_{221}	−2.45	$(P1^*S3)$	−2.45	$(D1^*S3)$	−3.29	$(P1^*P3)$
	−3.29	$(D1^*P3)$	−2.45	$(P1^*D3)$	−2.45	$(D1^*D3)$
	−0.73	$(P1^*P5)$	−0.73	$(D1^*P5)$	1.83	$(S3^*P5)$
	1.52	$(P3^*P5)$	−0.26	$(D3^*P5)$	−1.07	$(P1^*D5)$
	−1.07	$(D1^*D5)$	1.91	$(S3^*D5)$	1.20	$(P3^*D5)$
	−1.15	$(D3^*D5)$	0.75	$(S3^*D7)$	0.59	$(P3^*D7)$
	−0.19	$(D3^*D7)$	1.76	$(P5^*D7)$	1.62	$(D5^*D7)$
B^3_{001}	1.86	$(P3^*D3)$	3.10	$(D1^*P5)$	0.62	$(D3^*P5)$
	−1.51	$(P1^*D5)$	−0.54	$(P3^*D5)$	2.43	$(P5^*D5)$
	2.78	$(P1^*D7)$	−2.48	$(P3^*D7)$	−0.41	$(P5^*D7)$
B^3_{2-21}	1.39	$(S3^*P3)$	−3.10	$(S3^*D3)$	2.77	$(P3^*D3)$
	2.31	$(P1^*P5)$	−2.31	$(D1^*P5)$	−0.46	$(S3^*P5)$
	0.52	$(P3^*P5)$	−0.23	$(D3^*P5)$	−3.38	$(P1^*D5)$
	3.38	$(D1^*D5)$	0.34	$(S3^*D5)$	−0.30	$(P3^*D5)$
	0.60	$(P5^*D5)$	−1.04	$(P1^*D7)$	1.04	$(D1^*D7)$
	−2.07	$(S3^*D7)$	1.85	$(P3^*D7)$	−0.46	$(P5^*D7)$
	0.53	$(D5^*D7)$				
B^3_{2-11}	1.75	$(S3^*P3)$	−1.96	$(S3^*D3)$	0.88	$(P3^*D3)$
	1.46	$(P1^*P5)$	1.46	$(D1^*P5)$	−0.58	$(S3^*P5)$
	0.33	$(P3^*P5)$	−0.07	$(D3^*P5)$	−2.14	$(P1^*D5)$
	−2.14	$(D1^*D5)$	0.21	$(S3^*D5)$	0.38	$(P3^*D5)$
	−0.53	$(D3^*D5)$	−0.77	$(P5^*D5)$	1.64	$(P1^*D7)$
	1.64	$(D1^*D7)$	−1.31	$(S3^*D7)$	1.76	$(P3^*D7)$
	−1.31	$(D3^*D7)$	−0.44	$(P5^*D7)$	0.17	$(D5^*D7)$
B^3_{201}	1.86	$(S3^*P3)$	3.10	$(D1^*P5)$	−0.62	$(S3^*P5)$
	−1.51	$(P1^*D5)$	0.68	$(P3^*D5)$	−1.35	$(P5^*D5)$
	2.78	$(P1^*D7)$	1.66	$(P3^*D7)$	−0.41	$(P5^*D7)$

TABLE I. (*Continued*).

B^3_{211}	1.75	$(S3^*P3)$	1.96	$(S3^*D3)$	0.88	$(P3^*D3)$
	−1.46	$(P1^*P5)$	1.46	$(D1^*P5)$	−0.58	$(S3^*P5)$
	−0.33	$(P3^*P5)$	−0.07	$(D3^*P5)$	−2.14	$(P1^*D5)$
	2.14	$(D1^*D5)$	−0.21	$(S3^*D5)$	0.38	$(P3^*D5)$
	0.53	$(D3^*D5)$	−0.77	$(P5^*D5)$	1.64	$(P1^*D7)$
	−1.64	$(D1^*D7)$	1.31	$(S3^*D7)$	1.76	$(P3^*D7)$
	1.31	$(D3^*D7)$	−0.44	$(P5^*D7)$	−0.17	$(D5^*D7)$
B^3_{221}	1.39	$(S3^*P3)$	3.10	$(S3^*D3)$	2.77	$(P3^*D3)$
	−2.31	$(P1^*P5)$	−2.31	$(D1^*P5)$	−0.46	$(S3^*P5)$
	−0.52	$(P3^*P5)$	−0.23	$(D3^*P5)$	−3.38	$(P1^*D5)$
	−3.38	$(D1^*D5)$	−0.34	$(S3^*D5)$	−0.30	$(P3^*D5)$
	0.60	$(P5^*D5)$	−1.04	$(P1^*D7)$	−1.04	$(D1^*D7)$
	2.07	$(S3^*D7)$	1.85	$(P3^*D7)$	−0.46	$(P5^*D7)$
	−0.53	$(D5^*D7)$				
B^4_{001}	−2.41	$(D3^*D5)$	3.59	$(D1^*D7)$	1.02	$(D3^*D7)$
	−2.35	$(D5^*D7)$				
B^4_{2-21}	−1.48	$(P3^*P5)$	3.32	$(D3^*P5)$	1.62	$(S3^*D5)$
	−3.24	$(D3^*D5)$	2.31	$(P1^*D7)$	−2.31	$(D1^*D7)$
	−0.66	$(S3^*D7)$	0.83	$(P3^*D7)$	−0.53	$(D3^*D7)$
	−0.62	$(P5^*D7)$	−0.03	$(D5^*D7)$		
B^4_{2-11}	−2.10	$(P3^*P5)$	2.35	$(D3^*P5)$	2.29	$(S3^*D5)$
	−1.15	$(D3^*D5)$	1.64	$(P1^*D7)$	1.64	$(D1^*D7)$
	−0.94	$(S3^*D7)$	0.59	$(P3^*D7)$	−0.19	$(D3^*D7)$
	−0.44	$(P5^*D7)$	0.72	$(D5^*D7)$		
B^4_{201}	−2.30	$(P3^*P5)$	2.51	$(S3^*D5)$	3.59	$(D1^*D7)$
	−1.02	$(S3^*D7)$	1.07	$(D5^*D7)$		
B^4_{211}	−2.10	$(P3^*P5)$	−2.35	$(D3^*P5)$	2.29	$(S3^*D5)$
	−1.15	$(D3^*D5)$	−1.64	$(P1^*D7)$	1.64	$(D1^*D7)$
	−0.94	$(S3^*D7)$	−0.59	$(P3^*D7)$	−0.19	$(D3^*D7)$
	0.44	$(P5^*D7)$	0.72	$(D5^*D7)$		
B^4_{221}	−1.48	$(P3^*P5)$	−3.32	$(D3^*P5)$	1.62	$(S3^*D5)$
	−3.24	$(D3^*D5)$	−2.31	$(P1^*D7)$	−2.31	$(D1^*D7)$
	−0.66	$(S3^*D7)$	−0.83	$(P3^*D7)$	−0.53	$(D3^*D7)$
	0.62	$(P5^*D7)$	−0.03	$(D5^*D7)$		
C^1_{210}	−3.46	$(D1^*S3)$	−4.65	$(P1^*P3)$	−3.46	$(D1^*D3)$
	−1.39	$(S3^*D3)$	2.08	$(P3^*P5)$	3.17	$(S3^*D5)$
	−2.27	$(D3^*D5)$	2.42	$(D5^*D7)$		
C^2_{210}	−2.00	$(P1^*S3)$	−2.68	$(D1^*P3)$	1.79	$(S3^*P3)$
	−2.00	$(P1^*D3)$	3.58	$(P3^*D3)$	−3.58	$(D1^*P5)$
	0.89	$(S3^*P5)$	1.41	$(D3^*P5)$	−5.24	$(P1^*D5)$
	0.59	$(P3^*D5)$	1.34	$(P5^*D5)$	2.87	$(P3^*D7)$
	0.41	$(P5^*D7)$				
C^2_{220}	−4.00	$(P1^*S3)$	5.37	$(D1^*P3)$	3.58	$(S3^*P3)$
	−4.00	$(P1^*D3)$	1.79	$(P3^*D3)$	−1.79	$(D1^*P5)$
	1.79	$(S3^*P5)$	−0.26	$(D3^*P5)$	2.62	$(P1^*D5)$
	−1.17	$(P3^*D5)$	4.02	$(P5^*D5)$	1.43	$(P3^*D7)$
	1.23	$(P5^*D7)$				
C^1_{210}	3.39	$(S3^*D3)$	−2.53	$(P1^*P5)$	−2.26	$(P3^*P5)$
	−3.70	$(D1^*D5)$	1.48	$(S3^*D5)$	−3.70	$(D3^*D5)$
	−3.78	$(D1^*D7)$	1.51	$(S3^*D7)$	1.51	$(D3^*D7)$
	−1.15	$(D5^*D7)$				

TABLE I. (*Continued*).

C^3_{220}	5.37	$(S3^*D3)$	−4.00	$(P1^*P5)$	−3.58	$(P3^*P5)$
	5.86	$(D1^*D5)$	2.34	$(S3^*D5)$	−2.39	$(D1^*D7)$
	2.39	$(S3^*D7)$	−3.65	$(D5^*D7)$		
C^4_{210}	−4.20	$(D3^*P5)$	1.83	$(P5^*D5)$	−2.93	$(P1^*D7)$
	−2.62	$(P3^*D7)$	0.56	$(P5^*D7)$		
C^4_{220}	−5.94	$(D3^*P5)$	2.59	$(P5^*D5)$	−4.14	$(P1^*D7)$
	−3.70	$(P3^*D7)$	0.79	$P5^*D7)$		

ences in Eq. (37) were constant with t. Then any enhancement in $|S_3|^2$, $|P_1|^2$, $|P_3|^2$, or $|P_5|^2$ would cause a reduction in A^2_{000}/A^0_{000} at large t as compared with small t. The reduction would be most dramatic for pure $|P_3|^2$ ($\sim 67\%$); it would be $\sim 81\%$ for pure $|S_3|^2$ or $|P_1|^2$ and $\sim 95\%$ for $|P_5|^2$. The observed reduction, $\sim 64\%$, does not favor P_5. As we show next, if we take account of the P-wave interferences, it becomes even harder to accommodate an enhancement in $|P_5|^2$ at large t.

Finally, the A^2_{210} and A^2_{220} moments [Figs. 38(d), 38(e), 38(i), and 38(j)] show clear structure which may be related to $N(1700)$. The difference between these moments isolates a combination of P-wave terms:

$$A^2_{210}-A^2_{220}=-5.37P^*_1P_5-0.70|P_5|^2+2.40|P_3|^2 -0.25P^*_3P_5+2.68P^*_1P_3 \ . \quad (38)$$

Figure 39 shows this difference, absolutely normalized, for the two t regions. In the large-t bin [Fig. 39(b)], there is a broad peak in this difference moment just below the $N(1700)$ region. This structure, like the overall $N(1700)$ production cross section, is much less pronounced in the small-t bin [Fig. 39(a)]. For the large-t bin, the partial-wave analysis indicates that the difference is dominated by the $P^*_1P_5$ interference term, which has the largest coefficient in Eq. (38). The behavior of the difference moment suggests that P_1 and P_5 are relatively real in the vicinity of $N(1700)$; if P_5 were a Breit-Wigner form and P_1 a real background, the $P^*_1P_5$ interference would oscillate about zero. This difference is the clearest evidence in the data for structure related to $N(1700)$, and we note that any large $P^*_1P_5$ interference structure would also contribute positively to A^2_{000} [Eq. (37)]; therefore, with $P^*_1P_5$ removed, the relative diminution of A^2_{000} at large t in the $N(1700)$ region would be even more pronounced, and this would argue against a pure P_5 interpretation of $N(1700)$. As a result, the partial-wave fits tend to find more S_3 and less P_5 at large t, in the $N(1700)$ region.

The odd-L moments (Figs. 40 and 41) display a peak-dip structure in the region 1.45–1.70 GeV; especially for the low-t bin [Figs. 40(a) and 40(b)]. Other experiments seem to see similar effects in the odd moments,[7,25,26] but none have argued for any specific interpretation, nor do our partial-wave solutions indicate any dramatic amplitude structures that would explain these wiggles. However, our solutions are such that P_1 and P_5 are $\sim 90°$ out of phase with the dominant S_3 wave, and consequently a

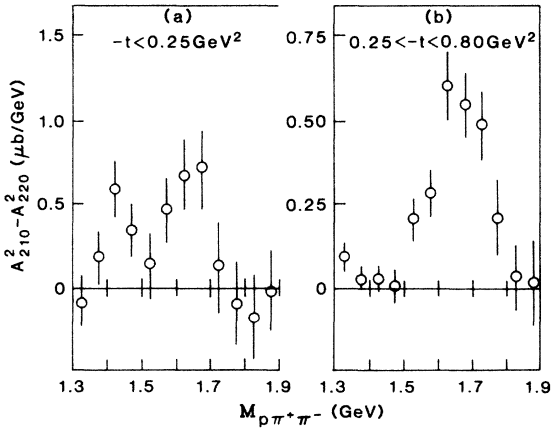

FIG. 39. Normalized cross-section difference given by t channel $A^2_{210}-A^2_{220}$ for (a) small-t and (b) large-t bins, plotted against mass. Note that we have integrated over $M_{p\pi^+}$ and t; e.g., $A^0_{000}=(1/16\pi^2)d\sigma/dM_{p\pi^+\pi^-}$ in this normalization.

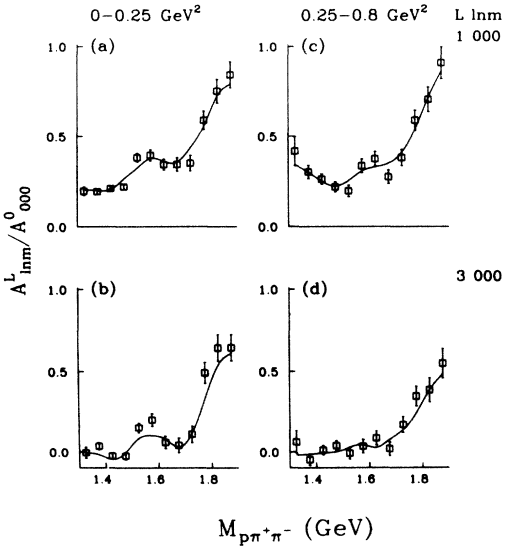

FIG. 40. t-channel A^L_{lnm}/A^0_{000} moments with odd L, $l=0$, plotted against mass for small-t (a), (b) and large-t (c), (d) bins: (a), (c) A^1_{000}; and (b), (d) A^3_{000}. The curves indicate the partial-wave fits.

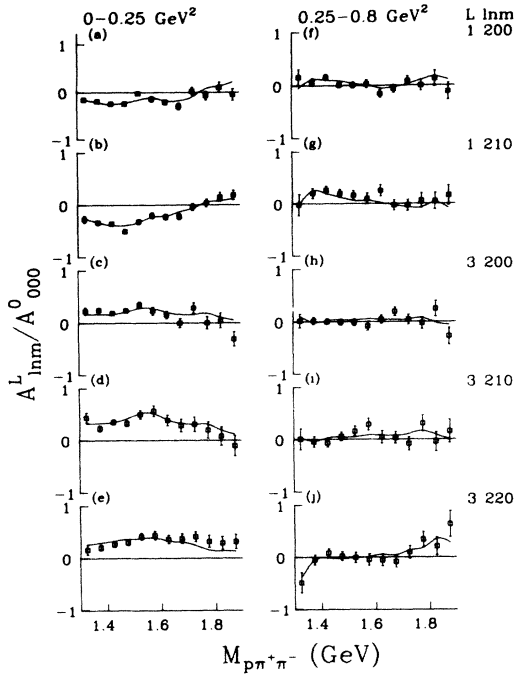

FIG. 41. t-channel A^L_{lnm}/A^0_{000} moments with odd L, $l=2$ plotted against mass for small-t (a)–(e) and large-t (f)–(j) bins: (a), (f) A^1_{200}; (b), (g) A^1_{210}; (c), (h) A^3_{200}; (d), (i) A^3_{210}; and (e), (j) A^3_{220}. The curves indicate the partial-wave fits.

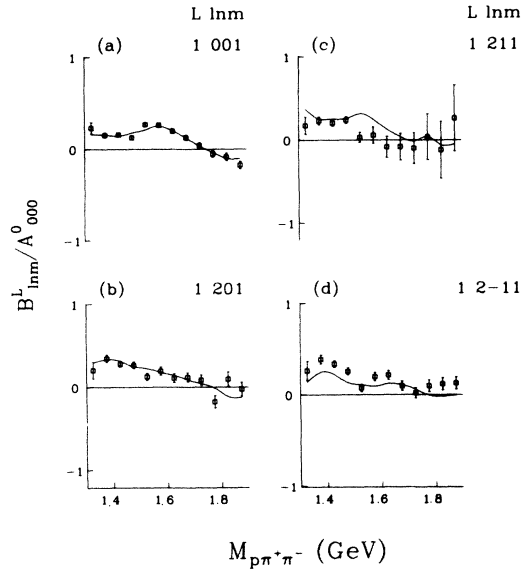

FIG. 42. t-channel B^L_{lnm}/A^0_{000} transverse-polarization moments with $L=1$, $m=1$ plotted against mass for $-t<0.25$ GeV^2. The curves indicate the partial-wave fits.

very small modulation of the S-wave phase can induce large effects in the S-P interferences, which contribute to $L=1$ and $L=3$, $l=2$ moments. The structure in A^3_{000} [Fig. 40(b)] would require P-D interference. Having inspected the moments and the coefficients in Table I, we speculate that a very small $N^*(1520)\to\Delta^{++}\pi^-$ wave, about 2% of the total cross section, with comparable S- and D-wave decay amplitudes, could mimic the effects seen in the odd moments. However, our partial-wave solutions provide no clear evidence on this. We remark that the $N^*(1520)\to\Delta^{++}\pi^-$ should, in fact, exhibit comparable S- and D-wave decays,[50] but in our partial-wave analysis, only the $\frac{3}{2}^-$ S wave is seen; we speculate, therefore, that $N^*(1520)$ resonance production may in fact occur at the almost undetectable level suggested by the odd-moment structures in our data.

C. Mass dependence of the polarized observables

The P waves in our solution turn out to be strongly out of phase with the $\frac{3}{2}^-$ S wave, in part because of the nature of the polarization moments. For the low-t bin, we show the $L=1,2$ helicity-conserving asymmetries in Figs. 42–44. We proceed to list the S-P interference contributions to the $l=0,2$ helicity-conserving moments, together with the average values seen in the low-mass region. For the $L=1$ transverse moments of Fig. 42, we have

$$B^1_{001}(\approx+0.25)=1.41P^*_1S_3-2.53P^*_3S_3+1.90P^*_5S_3\ , \tag{39a}$$

$$B^1_{201}(\approx+0.30)=1.41P^*_1S_3+2.02P^*_3S_3+0.38P^*_5S_3\ , \tag{39b}$$

$$B^1_{211}(\approx+0.30)=1.22P^*_1S_3+1.75P^*_3S_3+0.33P^*_5S_3\ , \tag{39c}$$

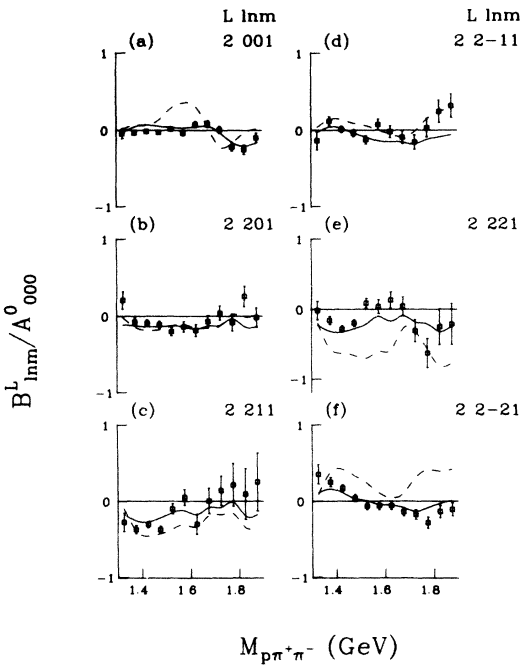

FIG. 43. t-channel B^L_{lnm}/A^0_{000} transverse-polarization moments with $L=2$, $m=1$, plotted against mass, for $-t<0.25$ GeV^2. The solid curves indicate the partial-wave fits. The dashed curve shows the effect of modifying the P_5 wave found in the fit to be pure Breit-Wigner peak with $M_r=1.68$ GeV, $\Gamma=0.15$ GeV.

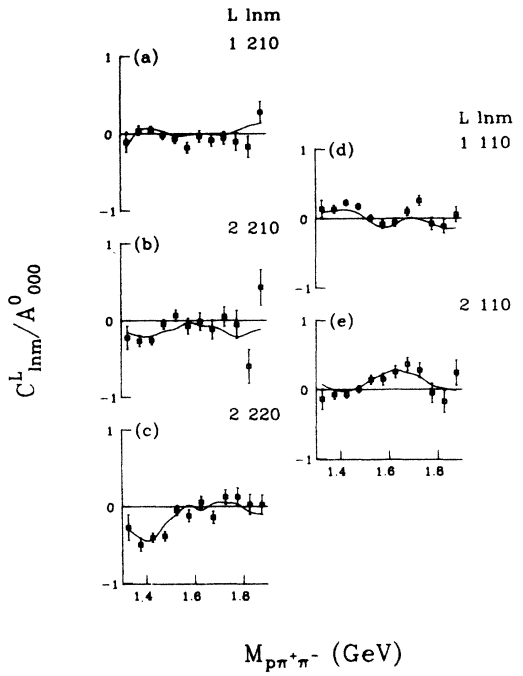

FIG. 44. t-channel C^L_{lnm}/A^0_{000} longitudinal-polarization moments with $m=0$ plotted against mass for $-t<0.25$ GeV^2. The curves indicate the partial-wave fits.

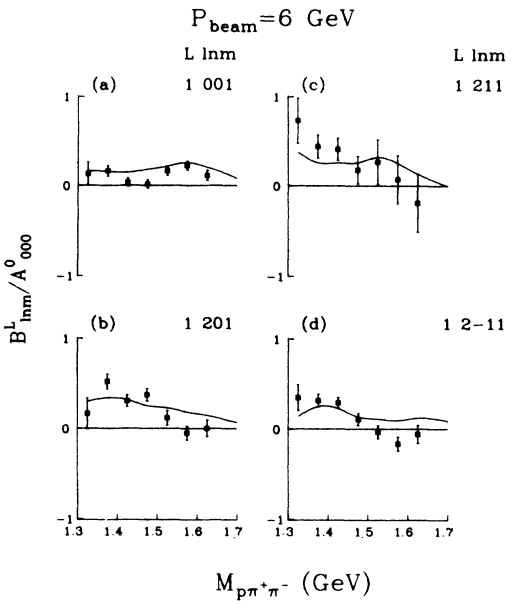

FIG. 45. t-channel B^L_{lnm}/A^0_{000} transverse-polarization moments with $L=1$, plotted against mass, for $-t<0.25$ GeV^2, at 6 GeV/c. The curves are the 11.75 GeV/c partial-wave fits.

$$B^1_{2\text{-}11}(\approx+0.40)=1.22P^*_1S_3+1.75P^*_3S_3+0.33P^*_5S_3\ , \tag{39d}$$

where the measured values are indicated in parentheses. For the $L=2$ transverse moments of Fig. 43, we have

$$B^2_{001}(\approx 0)=0\ , \tag{39e}$$

$$B^2_{201}(\approx -0.10)=0\ , \tag{39f}$$

$$B^2_{2\text{-}21}(\approx+0.30)=2.45P^*_1S_3+1.83P^*_5S_3\ , \tag{39g}$$

$$B^2_{221}(\approx -0.30)=-2.45P^*_1S_3-1.83P^*_5S_3\ , \tag{39h}$$

$$B^2_{2\text{-}11}(\approx 0)=1.22P^*_1S_3+0.91P^*_5S_3\ , \tag{39i}$$

$$B^2_{211}(\approx -0.30)=-1.22P^*_1S_3-0.91P^*_5S_3\ . \tag{39j}$$

For the longitudinal moments (Fig. 44), we have

$$C^1_{210}(\approx 0)=0\ , \tag{39k}$$

$$C^2_{210}(\approx -0.30)=-2P^*_1S_3-1.79P^*_3S_3-0.89P^*_5S_3\ , \tag{39l}$$

$$C^2_{210}(\approx -0.50)=-4P^*_1S_3-3.58P^*_3S_3-1.79P^*_5S_3\ , \tag{39m}$$

Comparison of B^1_{001} and B^1_{201} [Eqs. (39a) and (39b)] indicates that P_3 cannot play a major role in the asymmetries. Except perhaps for $B^2_{2\text{-}11}$, these 13 moments are all qualitatively consistent, in sign at least, with having only the $P^*_1S_3$ contribution. If instead we considered only the $P^*_5S_3$ term, then the signs of the moments would be consistent, but the observed B^1_{2n1} moments [Eqs. (39b)—(39d)] would be too large. Clearly, some admixtures of P_1 and P_5 contributions could describe the low-mass region. We remark that if pure unnatural-parity exchange waves were present, then the relative signs of the B^L_{lnm} and C^L_{lnm} would be reversed, and it would be impossible to explain even the qualitative features of the low-mass data with these P waves.

The partial-wave fits in Figs. 43—45 show some systematic discrepancies. To test the sensitivity of the fits, we altered the solution for the P_5 wave, modifying it to have a simple Breit-Wigner behavior, with phase and magnitude coincident with the true solution at 1.7 GeV. The effect on the $L=2$ moments is shown by the dashed curves in Fig. 43; of course, the unpolarized moments would also be sensitive to such a modification. Regarding the question of sensitivity, we remark that many of the polarizations appear to be consistent with zero. This does not mean that they have no information content. With a different mix of waves, the individual asymmetries could be much larger; for example, C^2_{220} in Fig. 44(c) is quantum-mechanically bounded by $|C^2_{220}|\leq 2$.

An older sample of transversely polarized 6-GeV/c data,[52] together with a small sample of longitudinally polarized 6-GeV/c data from this experiment, was analyzed in order to search for possible energy dependence in the transverse moments, which might be indicative of unnatural-parity-exchange backgrounds. We used the methods described in Sec. II, except that the A^L_{lnm} coefficients, which are needed for the polarized-moments analysis, were taken from the 11.75-GeV/c data; the 6-GeV/c acceptance was too limited to permit a full moments analysis of the unpolarized cross sections. The resulting spin correlations are qualitatively consistent with the raw asymmetries reported in Ref. 52. As an example, the $L=1$ B coefficients are shown in Fig. 45, compared with the results of the 11.75-GeV/c partial-wave analysis.

The agreement is qualitatively satisfactory, indicating no major change in the production naturality between 6 and 12 GeV/c.

D. Behavior of the $l=1$ moments

As noted in Sec. IV D, the Breit-Wigner phase difference between Δ^{++} and non-Δ^{++} waves might be expected, *a priori*, to cause significant asymmetries in the $l=1$ moments. The helicity-conserving $l=1$ spin correlations are shown in Figs. 44(d) and 44(e) (longitudinal) and Fig. 46 (transverse) for the low-t bin, together with the partial-wave fits. For completeness, we show the unpolarized helicity-conserving $l=1$ moments, in both t bins, in Fig. 47. We remark that some of the A^L_{1n0} moments are surprisingly large; if the only source of $p\pi^+$ s wave were the off-shell scattering contribution from the Deck diagram of Fig. 11(a), the s-Δ interference in A^L_{1n0} would integrate to zero over the $M_{p\pi^+}$ mass cut. This suggests that the $p\pi^+$ s-wave production comes from other sources, such as $N^*\pi$ or $p\epsilon$ isobar production.

E. Dependence of the moments on $M_{p\pi^+}$

Before examining the partial-wave solutions, we need to consider possible complications which might arise due to our averaging over a finite $M_{p\pi^+}$ band, $1.15 < M_{p\pi^+} < 1.30$ GeV. Although this averaging should pose no problem for the (dominant) Δ-Δ interference contributions, it can influence our interpretation of the non-Δ^{++} contribution. In principle, one can learn more about the isobar composition by fitting simultaneously in $M_{p\pi^+}$ as is done (schematically) in the PWA's of Refs. 21–26.

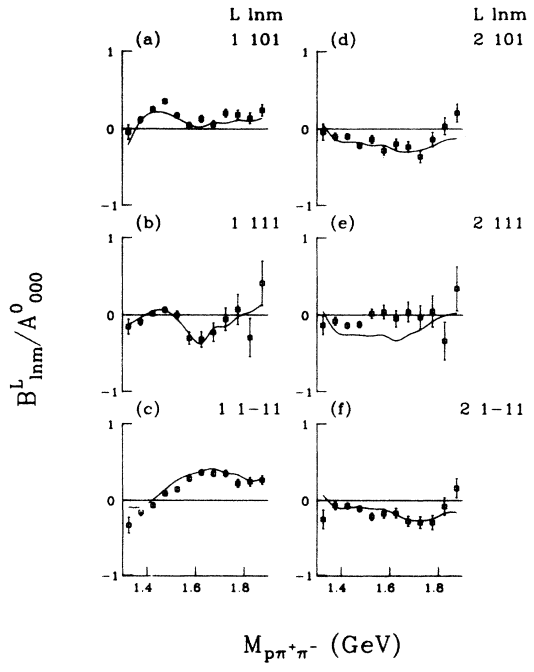

FIG. 46. t-channel B^L_{lnm}/A^0_{000} transverse-polarization moments with $l=1$, plotted against mass, for $-t<0.25$ GeV^2. The curves show the partial-wave fits.

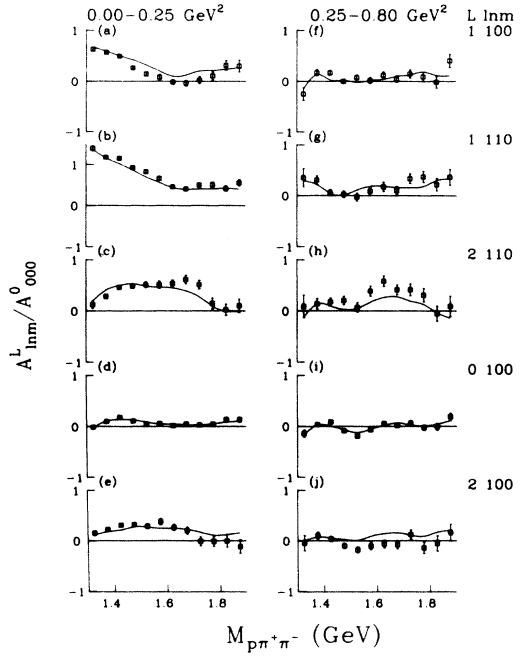

FIG. 47. t-channel A^L_{lnm}/A^0_{000} moments with $l=1$ plotted against mass for small-t (a)–(e) and large-t (f)–(j) bins: (a), (f), A^1_{100}; (b), (g) A^1_{110}; (c), (h) A^2_{110}; (d), (i) A^0_{100}; (e), (j) A^2_{100}. The curves show the partial-wave fits.

As explained in the Appendix, any non-$\Delta^{++}\pi^-$ isobar can be projected into a sum of $s,p,\Delta,\ldots$ waves, each with calculable $M_{p\pi^+}$ dependence. In simple cases, like the $p\epsilon$ isobars, these projections turn out to have smooth $M_{p\pi^+}$ dependence, and could be approximated as constants over the $1.15 < M_{p\pi^+} < 1.30$-GeV mass interval. In that case, and assuming that A^0_{000} is dominated by $|\Delta|^2$ contributions, the interferences between background waves (W_i) and Δ^{++} waves (W_Δ) have the following $M_{p\pi^+}$ dependence:

$$\frac{A^L_{lnm}}{A^0_{000}} \approx \frac{\mathrm{Re}W_i}{|W_\Delta|}\frac{M_{p\pi^+}-M_\Delta}{\Gamma_\Delta/2} + \frac{\mathrm{Im}W_i}{|W_\Delta|}\,, \tag{40a}$$

$$\frac{B,C^L_{lnm}}{A^0_{000}} \approx \frac{-\mathrm{Im}W_i}{|W_\Delta|}\frac{M_{p\pi^+}-M_\Delta}{\Gamma_\Delta/2} + \frac{\mathrm{Re}W_i}{|W_\Delta|}\,. \tag{40b}$$

For illustrative purposes, we have taken W_Δ to have the mass dependence and phase of the Δ^{++} Breit-Wigner peak. The joint moments, averaged over $M_{p\pi^+}$, pick out the second terms in Eqs. (40a) and (40b). It is easy to show that the dependence of Eq. (40) can be taken into account in these averaged moments, provided that we include a coherence factor of ~ 0.75 for all interference terms involving non-Δ^{++} with Δ^{++} waves; we have done this for all s-Δ and p-Δ interferences in our fits.

The first terms in Eqs. (40a) and (40b) oscillate about M_Δ, and it is this characteristic behavior that would in principle allow determination of the phases of W_i from the $M_{p\pi^+}$ dependence; this is, of course, essential for PWA in the absence of polarization data. Accordingly,

we have examined our data for evidence of such oscillatory behavior. We show the first few helicity-conserving moments for small t and for two $M_{p\pi^+\pi^-}$ intervals as functions of $M_{p\pi^+}$ in Figs. 48—50. None of the moments can be said to be constant in $M_{p\pi^+}$. On the other hand, none of the $l=0,2$ moments (which allow Δ-Δ contributions) exhibit zeros at the Δ^{++} mass, except perhaps the $L=1$ moments in Figs. 49(a), 49(b), 49(f), and 49(g). By contrast, all the $l=1$ moments (Fig. 50), except A^1_{110} [Fig. 50(c)], exhibit crossover zeros, or at least strong oscillations, near M_Δ. This is as expected, since the $l=1$ moments are presumably dominated by s-Δ interference.

The curves in Figs. 48—50 are based on the following ansatz, which can be applied sensibly only to Δ-Δ interference terms. Aside from a common dependence on the Δ^{++} Breit-Wigner peak, suppose that the only variation of the partial waves with $M_{p\pi^+}$ and $M_{p\pi^+\pi^-}$ arises through their dependence on the kinematical variable Q_Δ, the $(p\pi^+)$ momentum in the $(p\pi^+\pi^-)$ c.m. This would not be the case if the waves had Breit-Wigner dependence on $M_{p\pi^+\pi^-}$; it would be the case for the Deck diagrams, to a good approximation. Given only a Q_Δ dependence, the moments which increase with $M_{p\pi^+}$ would decrease with $M_{p\pi^+\pi^-}$, and vice versa. We fitted the $M_{p\pi^+\pi^-}$ moments spectra to polynomials in Q_Δ (taking a nominal Δ^{++} mass for $M_{p\pi^+}$), and then used this Q_Δ dependence to predict the dependence on $M_{p\pi^+}$ shown in Figs. 48—50. These curves fail utterly for the $l=1$ moments which exhibit crossover zeros (Fig. 50), and that is as expected. For the Δ-Δ interference moments of Figs. 48 and 49, they generally predict the sense of the $M_{p\pi^+}$ variations correctly.

This is certainly a simplistic analysis, but it illustrates a subtle problem. We could interpret the $M_{p\pi^+}$ dependence in terms of a mix of isobars, and this would be *a priori* correct for the $l=1$ moments, which do not allow Δ-Δ in-

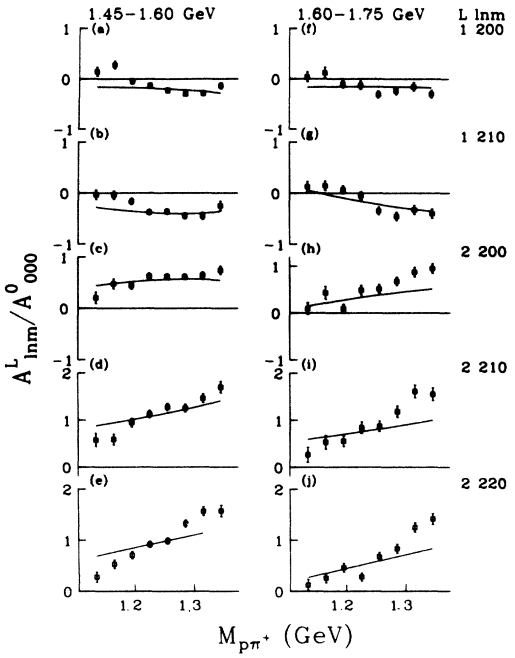

FIG. 49. t-channel A^L_{lnm}/A^0_{000} moments with $l=2$ for $-t<0.25$ GeV^2 plotted against $M_{p\pi^+}$ for $1.45<M_{p\pi^+\pi^-}<1.60$ GeV (a)—(e) and $1.60<M_{p\pi^+\pi^-}<1.75$ GeV (f)—(j): (a), (f) A^1_{200}; (b), (g) A^1_{210}; (c), (h) A^2_{200}; (d), (i) A^2_{210}; and (e), (j) A^2_{220}.

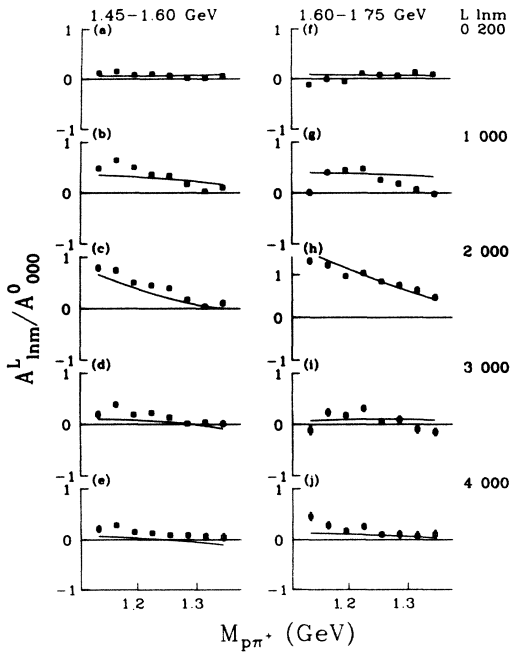

FIG. 48. t-channel A^L_{lnm}/A^0_{000} moments with $l=0$ for $-t<0.25$ GeV^2 plotted against $M_{p\pi^+}$ for two $M_{p\pi^+\pi^-}$ intervals -1.45 to 1.60 GeV (a)—(e), and 1.60 to 1.75 GeV (f)—(j): (a), (f) A^0_{200}; (b), (g) A^1_{000}; (c), (h) A^2_{000}; (d), (i) A^3_{000}; and (e), (j) A^4_{000}.

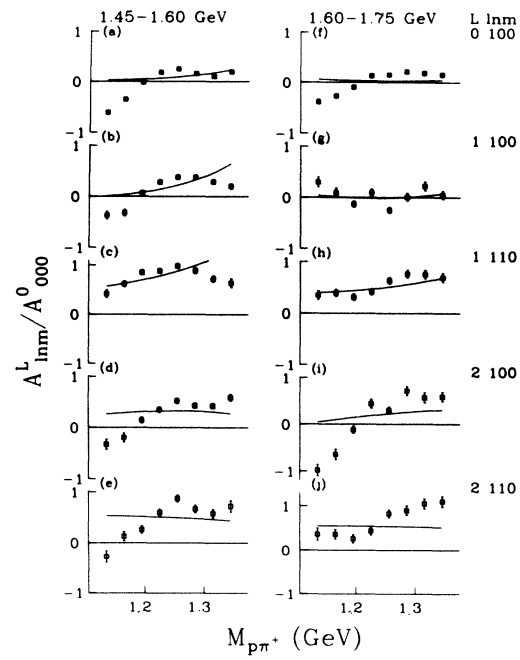

FIG. 50. t-channel A^L_{lnm}/A^0_{000} moments with $l=1$ for $-t<0.25$ GeV^2; plotted against $M_{p\pi^+}$, for $1.45<M_{p\pi^+\pi^-}<1.60$ GeV (a)—(e), and $1.60<M_{p\pi^+\pi^-}<1.75$ GeV (f)—(j); (a), (f) A^0_{100}; (b), (g) A^1_{100}; (c), (h) A^1_{110}, (d), (i) A^2_{100}, and (e), (j) A^2_{110}.

terference. However, there is clearly some ambiguity in deciding how the Δ-Δ interferences themselves should depend on $M_{p\pi^+}$, and therefore it may be problematic to obtain the isobar contributions from the $M_{p\pi^+}$ dependence, as is done (schematically) in the usual PWA. Our fitting procedure, using the $M_{p\pi^+}$-averaged moments, should be reasonably accurate as long as the $M_{p\pi^+}$ dependences of the Δ-Δ interference moments are not too pathological; however, it is slightly biased in that the coherence factor of 0.75 is not included for Δ-Δ interference moments, where one of the Δ ($J^P=\frac{3}{2}^+$) waves is in fact a reflection of a background isobar.

F. Partial-wave fits

We tried a total of 36 waves ($\lambda_t=\frac{3}{2},\frac{1}{2},-\frac{1}{2}$, with $L=0,1,2$ for $\Delta\pi$ waves and $L=0,1$ for $j^P=\frac{1}{2}^{\pm}$ $p\pi^+$ isobars) in our fits, in combinations of ≤ 25 waves at a time. Some waves were consistent with noise and were eliminated, but most of the small waves ($<2\%$ of the total cross section) exhibited continuous phase behavior. The larger waves, having $>2\%$ of the total cross section, were fairly stable against inclusion or exclusion of the smaller waves in the fits. The intensities and relative phases of the eight largest $\lambda_t=\frac{1}{2}$ waves, from representative solutions, are shown in Figs. 51 and 52. We remark that, motivated by the $N(1700)$ bump, we searched for radically different solutions (i.e., with Breit-Wigner phases, and with large helicity-flip components) without notable success. The waves shown in Fig. 51 together make up $\sim 95\%$ of the cross section in the $N(1700)$ region.

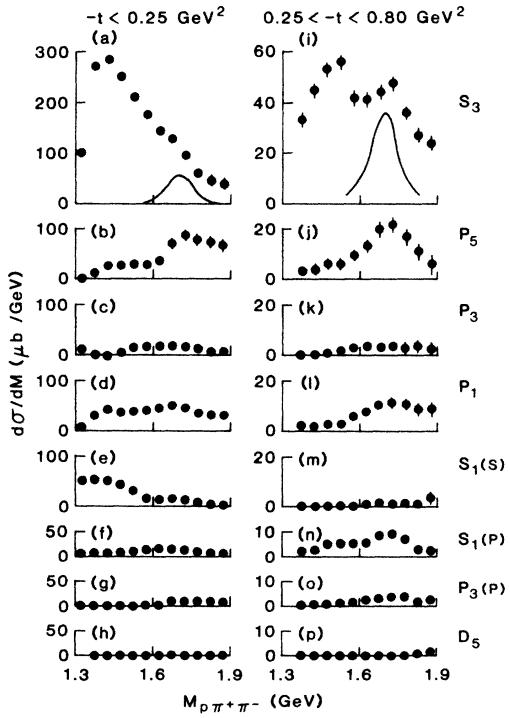

FIG. 51. Intensities of the larger helicity-nonflip waves for small t (a)—(h) and large t (i)—(p), plotted against $M_{p\pi^+\pi^-}$.

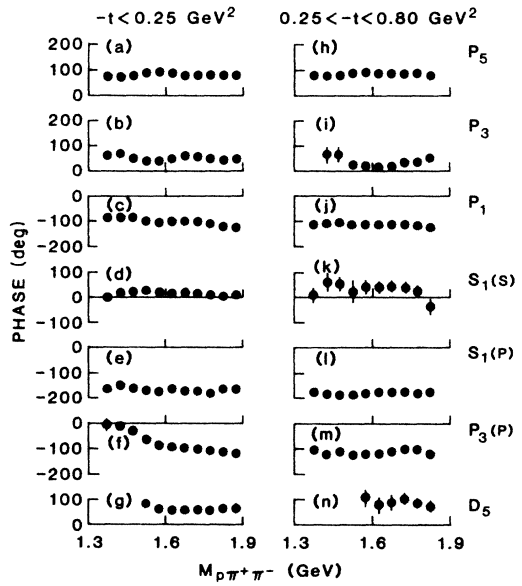

FIG. 52. Relative phases of the larger helicity-nonflip waves for small t (a)—(g) and large t (h)—(n); S_3 was chosen as a 0° reference wave.

Where the waves are large, they show little phase variation with respect to S_3, which we chose as a reference. Qualitatively, the relative phases of the larger waves over a broad range can be given as $-90°$ (P_1), $+45°$ (P_3), $+90°$ (P_5), $0°$ ($S_1(s)$), $180°$ ($S_1(p)$), and $-120°$ ($P_3(p)$), for both t regions. [Nomenclature: As before, S_3, $P_1,\ldots$, etc., refer to Δ waves with quantum numbers L_{2J}; $S_1(s)$ refers to $\frac{1}{2}^+$ overall S wave for the $p\pi^+$-π^- system with $p\pi^+$ s-wave isobar, etc.] The D waves are very small, except perhaps for D_5 at low t, which makes up $\sim 1.5\%$ of the cross section near the $\frac{5}{2}^-$ resonance.

None of the published partial-wave analyses indicate any significant phase variations,[21–26] nothing such as one could expect if the $N(1700)$ were a single J^P state with Breit-Wigner phase. As we have emphasized, our experiment differs from other investigations in that the polarization data have been used for the partial-wave phase determination, rather than the isobar technique. The only direct comparison which we can make on the phases for reaction (1) is with Blobel *et al.*[21] For the $\Delta^{++}\pi^-$ isobars, Blobel *et al.* reported the phases of P_1 relative to S_3 to be $-80°$ to $-130°$ for masses of 1.35—1.60 GeV; and for P_5 relative to P_1 to be $+140°$ to $+180°$ for masses 1.60—1.85 GeV; our phases are fairly consistent with these, namely, $\sim -90°$ for P_1 relative to S_3 and $+190°$ for P_5 relative to P_1 in the indicated mass regions (Blobel *et al.* did not include P_3 in their fits). Considering the rather different approaches, one would be surprised to see any better quantitative agreement between the two experiments.

The other analyses all reported large cross sections for $\frac{3}{2}^-$, $\frac{1}{2}^+$, and $\frac{5}{2}^+$, more or less as we do. In particular, although there is no clear consensus as to the source of the $N(1700)$ bump, all analyses reported more than one wave to be important in the bump region. (For good over-

views of the other analyses, consult Refs. 26 and 53.) We have estimated the size of the $N(1700)$ enhancement from the mass spectra (Fig. 37), and have indicated in Fig. 51 the corresponding intensity pattern by the solid curves, in order to see whether all of the $N(1700)$ bump could possibly be attributed to a single partial wave. For small t, it could be reasonably tucked into the P_5 or S_3 distributions. For large t, the P_5 cross section is too small to account for the whole bump, but S_3 could (barely) absorb all of it. The intensity patterns seem to indicate that other waves contribute to the bump, such as P_1. We conclude that because $N(1700)$ is a large effect, only S_3 is large enough to account for all the effects at all t values. In view of the phase behavior, it appears unlikely that $N(1700)$ can be interpreted as a Breit-Wigner resonance in a single wave.

We note that the solutions indicate that the large $\Delta^{++}\pi^-$ waves are not relatively real, as one might naively expect for the Deck processes of Fig. 11(a). Moreover, one would expect the non-Δ^{++} waves to be $\sim 90°$ out of phase with the $\Delta^{++}\pi^-$ waves if they were simply caused by the $J^P=\frac{1}{2}^{\pm}$ π^+p waves in virtual π^+p scattering, as in Fig. 11(a); instead, we find that the larger waves, $S_1(s)$ and $S_1(p)$ are essentially real relative to S_3. We note that Ascoli, Jones, Weinstein, and Wyld[54] reported a quantitative partial-wave analysis of the Deck amplitudes for $(3\pi)^{\pm}$ production, and found that phase differences of $\pm 90°$ could be expected for the various partial waves, provided that the pion-exchange Regge phase was included. Presumably, this quantitative behavior would carry over to reaction (1).

Finally, we might suppose that the isobar content of the $N(1700)$, which we examined in Sec. III, would be reflected in the partial-wave solutions. The threshold enhancement which appears in $N(1520)\pi^+$ should overlap with the Δ^{++} band, although about half of the sharp peak at ~ 1700 MeV in Figs. 13 and 14 would be lost due to the cut on $M_{p\pi^+}$ at 1.15 GeV. If this enhancement were a Deck effect [Fig. 11(b)], then we might expect it to be mainly S wave, e.g., $J^P=\frac{3}{2}^+$, but the $\frac{3}{2}^+$ cross sections which we observe are small and rather nondescript; P_3 is smooth and makes up 5—10% of the cross section; $P_3(p)$ does seem to turn on above 1600 MeV, but is only $\sim 5\%$ of the cross section in both t bins. An alternative possibility is that the $N(1520)\pi^+$ signal is due to a P-wave resonance, for example, $J^P=\frac{3}{2}^-$ or $\frac{5}{2}^-$. In this scenario, the true resonance phase advance in the $N(1520)\pi^+$ wave could easily be washed out in interference terms involving $\Delta^{++}\pi^-$ waves, by the kinematical correlations between $M_{p\pi^+}$ and $M_{p\pi^-}$.[55] Although $N(1520)\pi^+$ has been observed in $\frac{5}{2}^-$ $D_{15}(1675)$ decay,[36] it is clear that $\frac{5}{2}^-$ cannot account for the $N(1700)$ bump in our data; also, there is no clear evidence from formation experiments for $N(1520)\pi^+$ coupling to a $\frac{3}{2}^-$ resonance. Thus, the partial-wave solutions do not indicate any obvious role for the $N(1520)\pi^+$ threshold enhancement. Further, since $\sim 70\%$ of the $N(1700)$ signal in the Δ^{++}-cut sample is associated with genuine $\Delta^{++}\pi^-$ isobar production (cf. Fig. 16), we are still left with no explanation for the lack of phase variation in the $\Delta^{++}\pi^-$ waves.

VI. SUMMARY

We have presented angular distribution and polarization data for reaction (1) at 11.75 GeV/c, based on a 2×10^6 events sample. The $p\pi^+\pi^-$ mass spectrum displays no structure other than a bump, $N(1700)$, on top of a smooth, Deck-type background which peaks at low mass. In addition to $\Delta^{++}\pi^-$ isobars, we find clear signals for $N(1520)$-π^+, $N(1680)$-π^+, and $\rho^0(770)$-p final states in the $p\pi^+\pi^-$ system. The magnitude of the N^*-π^+ signals is roughly consistent with what one would expect from the pion-exchange Deck effect. In particular, the $N(1520)$-π^+ signal seems to peak sharply at threshold and therefore could be a component in the $N(1700)$ bump; only about half of the $N(1700)$ intensity can be attributed to $\Delta^{++}\pi^-$. We noted that an $N(1520)$-π^+ wave close to threshold is unlikely to have $J^P=\frac{5}{2}^+$, and so such a component might explain why the $N(1700)$ does not appear as a pure $\frac{5}{2}^+$ wave in the partial wave analyses.[21—26] In our partial-wave analysis, we imposed a Δ^{++} cut to enhance $\Delta^{++}\pi^-$ waves; in any case, the partial-wave analysis did not indicate any clear signal for likely reflections of the $N(1520)$-π^+ enhancement.

We have presented cross sections and angular distributions as functions of momentum transfer for the $\Delta^{++}\pi^-$ final state, defined by a Δ^{++} cut, $1.15<M_{p\pi^+}<1.30$ GeV. The t distributions show a slope-mass correlation and a break at $-t=0.25$ GeV^2, similar to those observed in much higher-energy DD processes.[3,7,8] We showed that the angular distribution moments, in particular A^L_{lnm} with $L=2$, $l=2$, could be used to establish directly the dominance of S-wave production at threshold and the absence of significant $J^P=\frac{1}{2}^+$ excitation. These moments suggest that the break in the t distribution coincides with a minimum in the production of s-channel helicity $=+\frac{1}{2}$ S wave, consistent with the absorbed Deck model of Berger and Pirilä.[31] The crossing relations are such that the S wave is mainly helicity conserving ($\lambda_t=\frac{1}{2}$) in the t channel.

We showed that the pattern of Φ dependence requires some helicity flip in both s and t channels for S, P, and D waves; the pattern of helicity nonconservation, evidenced by the Φ_s and Φ_t dependence of the moments, is qualitatively similar to that seen in higher energy $N\pi$ and $p\pi^+\pi^-$ DD processes,[1,7] and to that predicted by the Deck model.[28—32] Specifically, the Φ dependence is stronger in the s channel than in the t channel, and $\Phi=180°$ is favored over $\Phi=0°$ in both channels for forward $N^*\to\Delta^{++}\pi^-$ decays; the backward decays are flatter in Φ, perhaps due to nucleon-exchange deck contributions.[2,29,30]

We showed that the polarization asymmetry, integrated over all $p\pi^+\pi^-$ decay angles is small, around -15% in the low-mass region. In addition, we determined a large number of spin correlations which are sensitive to helicity-nonconservation in the production process; they turn out to be generally small but nonzero.

We performed a spin-parity analysis of the t-channel moments in two momentum-transfer intervals, as functions of $M_{p\pi^+\pi^-}$. We showed that there exist small structures in the odd moments which might indicate

$N^*(1520)\to\Delta^{++}\pi^-$ at the few percent level, and larger structures in the even moments that indicate P-wave interferences in the $N(1700)$ region. We noted that the helicity-conserving polarization asymmetries are dominated by S-P interferences, which require the $\frac{1}{2}^+$ and $\frac{5}{2}^+$ P waves to be $\sim 90°$ out of phase with the $\frac{3}{2}^-$ S wave. We obtained similar asymmetries from an analysis of a smaller 6-GeV/c sample, indicating that the assumption of natural-parity exchange production is consistent with the energy dependence. We did not include $N^*\pi^+$, $p\epsilon$, or $p\rho^0$ isobars directly in the spin-parity analysis, but showed that the $M_{p\pi^+}$ dependence of the moments is at least qualitatively consistent with predominantly Δ-Δ-type interference for the even moments, and non-Δ-Δ interference in the $l=1$ moments, as expected.

In the partial-wave solutions, the $J^P=\frac{3}{2}^-$ $\Delta^{++}\pi^-$ S wave was the largest contribution, and the $J^P=\frac{1}{2}^+$, $\frac{3}{2}^+$, and $\frac{5}{2}$ $\Delta^{++}\pi^-$ P waves are next in importance. The D waves and t-channel helicity-flip waves were small everywhere. In addition, there were important contributions from $J^P=\frac{1}{2}^\pm$ waves involving the non-Δ^{++}, $J^P=\frac{1}{2}^\pm$ $p\pi^+$ isobars. The integrated $J^P=\frac{1}{2}^+$ cross section in the threshold region ranges from $\sim 20\%$ of the total at low t to $\sim 5\%$ at large t, indicating that production of $N(1440)\to p\pi^+\pi^-$ is not a dominant effect. Similarly, the absence of appreciable intensity for $J^P=\frac{3}{2}^-$ D wave, at the few percent level, argues against significant $N(1520)\to\Delta\pi$ production.

For the larger waves, we found no evidence for relative phase variations, either near threshold or in the $N(1700)$ region. Our phases are qualitatively consistent with the Δ-π phases reported by Blobel *et al.*[21] The $N(1700)$ intensity seems to be shared between several waves, e.g., $\frac{3}{2}^-$, $\frac{1}{2}^+$, and $\frac{5}{2}^+$, and in the large-t region where $N(1700)$ is most prominent, its cross section exceeds the $J^P=\frac{5}{2}^+$ intensity by a factor of 2. There is little indication of $J^P=\frac{5}{2}^-$ production. In principle, the threshold enhancement in $N(1520)\pi^+$ could be explained in terms of production of the $D_{15}(1675)$ resonance, since that is observed to have a significant $N(1520)\pi$ decay probability,[36] but we see no evidence for this in the partial-wave solutions. We noted that the $N(1700)$, which we observe in $p\pi^+\pi^-$, has a very similar t dependence to that observed in missing-mass experiments; if it is the $p\pi^+\pi^-$ decay mode of the same object, then the $\Delta\pi$ cross section which we observe for $N(1700)$ would be consistent with the assignment $F_{15}(1680)$, but not $D_{15}(1675)$. It is somewhat peculiar that the $N(1700)\to p\pi^+\pi^-$ production can have the same t dependence and energy dependence as the inclusive process, if the $N(1700)$ is in fact a mixture of different J^P states, presumably from different production mechanisms.

Naturally, we were distressed at our failure to detect clear Breit-Wigner behavior for such a prominent, resonancelike object, given the powerful handles provided by high statistics and polarization data. Identification of the nature of $N(1700)$ would seem to be a prerequisite for the more difficult job of finding new baryonic resonances in $p\pi\pi$ production. Nevertheless, given the apparent energy independence of the main features of the DD processes, we anticipate that the detailed angular distribution and polarization moments obtained in this experiment should help in more sophisticated model building.

ACKNOWLEDGMENTS

We acknowledge the technical assistance of I. Ambats, J. Dawson, L. Filips, and E. Walschon. We thank R. Ely, C. Klindworth, R. Rivetna, and S. Watson for help with the online computers and the data processing. We thank the ZGS staff for the smooth operation of the accelerator. We acknowledge the participation of D. Cohen, N. Lockyer, C. E. W. Ward, and P. Zemany in the early phases of the experiment. This work was supported by the U.S. Department of Energy under Contract No. W-31-109-Eng-38.

APPENDIX: FORMALISM

This appendix outlines the relations between amplitudes and spin observables. Our discussion parallels that of Ref. 38. See Refs. 37 and 56 for discussion of formalism used for the formation reactions (2).

We begin by specifying coordinate frames and kinematic angles. We use subscripts b, t, r, and N to denote the beam, target, and recoil proton, and the $(p\pi^+\pi^-)$ system, respectively; we use p, π^+, and π^- subscripts to denote the N dissociation products. We can define production-helicity amplitudes for the quasi-two-body reaction

$$A^{\lambda_N\lambda_b}_{\lambda_r\lambda_t}(p_bp_t\to(p\pi^+\pi^-)_Np_r)\ , \tag{A1}$$

where the spin state of each particle, $|J,J_z=\lambda_i\rangle$ refers to specific coordinate axes in the particle's rest frame. The y axis is common to all four particles and is the Basel-convention production normal

$$\hat{\mathbf{y}}=\hat{\mathbf{p}}_b\times\hat{\mathbf{p}}_N\ . \tag{A2}$$

The (x,z) axes are specific to each particle and are different for s- and t-channel frames, e.g., (x_s,z_s) and (x_t,z_t). Since our experiment averages over target and recoil proton spins, we need to specify only the beam and the N-system coordinate frames.

First consider the beam particle, with polarization vector $\mathbf{P}$. We can define

$$P_z^{(s)}=\mathbf{P}\cdot(-\hat{\mathbf{p}}_t)\ , \tag{A3a}$$

$$P_y^{(s)}=P_y^{(t)}=\mathbf{P}\cdot\hat{\mathbf{y}}\ , \tag{A3b}$$

$$P_x^{(s)}=\mathbf{P}\cdot[\hat{\mathbf{y}}\times(-\hat{\mathbf{p}}_t)]\ , \tag{A3c}$$

$$P_z^{(t)}=\mathbf{P}\cdot(-\hat{\mathbf{p}}_N)\ , \tag{A3d}$$

$$P_x^{(t)}=\mathbf{P}\cdot[\hat{\mathbf{y}}\times(-\hat{\mathbf{p}}_N)]\ , \tag{A3e}$$

where $\mathbf{p}_t$ and $\mathbf{p}_N$ are evaluated in the b rest frame (RF). The relation between s- and t-channel polarizations is given explicitly by

$$\begin{bmatrix}P_x\\P_z\end{bmatrix}_t=\begin{bmatrix}\cos\chi_b & \sin\chi_b\\-\sin\chi_b & \cos\chi_b\end{bmatrix}\begin{bmatrix}P_x\\P_z\end{bmatrix}_s\ , \tag{A4}$$

where χ_b is a positive angle; $\chi_b\to 0$ for $t\to t_{\min}$, and $\chi_b\sim 45°$ for moderate momentum transfers. The s-channel $P_x^{(s)}$ and $P_z^{(s)}$ correlations are measured with in-

dependent data sets; these must be combined to obtain $P_x^{(t)}$ and $P_z^{(t)}$ correlations.

The s- and t-channel frames for the $(p\pi^+\pi^-)$ systems are well known. The parent N has $|J,J_z=\lambda_N\rangle$ quantized in a frame given by the common y axis of (A2), and

$$\hat{\mathbf{z}}_s=-\hat{\mathbf{p}}_r\ , \tag{A5a}$$

$$\hat{\mathbf{z}}_t=+\hat{\mathbf{p}}_b\ , \tag{A5b}$$

$$\hat{\mathbf{x}}_{s,t}=\hat{\mathbf{y}}\times\hat{\mathbf{z}}_{s,t}\ , \tag{A5c}$$

where $\hat{\mathbf{p}}_r$ and $\hat{\mathbf{p}}_b$ are evaluated in the N RF. To define the decay angles, consider a final coordinate frame based on the three-body decay plane:

$$\hat{\mathbf{z}}'=\hat{\mathbf{p}}_{p\pi^+}\ , \tag{A6a}$$

$$\hat{\mathbf{y}}'=\hat{\mathbf{p}}_{p\pi^+}\times\hat{\mathbf{p}}_p\ , \tag{A6b}$$

$$\hat{\mathbf{x}}'=\hat{\mathbf{y}}'\times\hat{\mathbf{z}}'\ . \tag{A6c}$$

Then the angles (Φ_s,Θ_s,ϕ_s) and (Φ_t,Θ_t,ϕ_t) are the Euler angles that rotate the production frames, (x_s,y,z_s) or (x_t,y,z_t) to the (x',y',z') frame. We define them explicitly as follows:

$$\cos\Theta_{s,t}=\hat{\mathbf{p}}_{p\pi^+}\cdot\hat{\mathbf{z}}_{s,t}\ , \tag{A7a}$$

$$\sin\Theta_{s,t}\sin\Phi_{s,t}=\hat{\mathbf{p}}_{p\pi^+}\cdot\hat{\mathbf{y}}\ , \tag{A7b}$$

$$\sin\Theta_{s,t}\cos\Phi_{s,t}=\hat{\mathbf{p}}_{p\pi^+}\cdot\hat{\mathbf{x}}_{s,t}\ , \tag{A7c}$$

with $\hat{\mathbf{p}}_{p\pi^+}$ evaluated in the $(p\pi^+\pi^-)$ RF. The $(p\pi^+)\to p\pi^+$ polar decay angle is given by

$$\cos\theta=\hat{\mathbf{p}}_p\cdot\hat{\mathbf{z}}'\ , \tag{A8}$$

evaluated in the $(p\pi^+)$ RF [to avoid confusion, take $\hat{\mathbf{z}}'=-\hat{\mathbf{p}}_{\pi^-}$ in the $(p\pi^+)$ RF]. The angle θ is independent of s- and t-channel conventions, and can be thought of as a final rotation about $\hat{\mathbf{y}}'$, which takes $\hat{\mathbf{z}}'\to\hat{\mathbf{p}}_p$. The angle $\phi_{s,t}$ can be defined by

$$\sin\theta\sin\phi_{s,t}=\hat{\mathbf{p}}_p\cdot(\hat{\mathbf{z}}_{s,t}\times\hat{\mathbf{z}}')\ , \tag{A9a}$$

$$\sin\theta\cos\phi_{s,t}=\hat{\mathbf{p}}_p\cdot(\hat{\mathbf{z}}_{s,t}\times\hat{\mathbf{z}}')\times\hat{\mathbf{z}}'\ , \tag{A9b}$$

with all vectors evaluated in the $(p\pi^+)$ RF. The initial $\mathbf{z}_t$ axis can be obtained by a clockwise rotation of $\mathbf{z}_s$ around $\hat{\mathbf{y}}$ by an angle χ_N; for modest t values $\chi_N\sim 90°$, while for $t\to t_{\min}$, $\chi_N\to 0°$. Consequently, in any realization of the rotation group, the s- and t-channel Euler angles are related by

$$R(0,-\chi_N,0)R(\Phi_t,\Theta_t,\phi_t)=R(\Phi_s,\Theta_s,\phi_s)\ . \tag{A10}$$

(The order of rotations begins at the left, the positive angles refer to counterclockwise rotations.) In the following discussions, we will refer to the Euler angles generically as (Φ,Θ,ϕ).

Next we express the amplitudes for specific helicity states λ_p for the decay proton, in terms of the production amplitudes of Eq. (A1), e.g.,

$$M^{\lambda_p\lambda_b}_{\lambda_r\lambda_t}=\sum_{(i)}A^{\lambda_i\lambda_b}_{\lambda_r\lambda_t}(pp\to N_ip)\cdot F^{\lambda_p}(i;\Theta,\Phi,\theta,\phi)\ . \tag{A11}$$

Here (i) refers to all the properties of the produced $(p\pi^+\pi^-)$ partial wave N_i, which includes

$$\begin{aligned}
&J_i=\text{total angular momentum}\ ,\\
&\lambda_i=\text{production helicity}\ ,\\
&L_i=\text{orbital momentum for, e.g., } p\pi^+\text{-}\pi^-\text{ system}\ ,\\
&S_i=\text{total spin for, e.g., } p\pi^+\text{-}\pi^-\text{ system}\ ,\\
&j_i=\text{total } j \text{ for, e.g., } p\pi^+\text{ subsystem}\ ,\\
&l_i=\text{orbital momentum for, e.g., } p\pi^+\text{ system}\ ,\\
&\zeta_i=\text{exchange naturality (see below)}\ .
\end{aligned} \tag{A12}$$

The functions $F^{\lambda_p}(i,\ldots)$ in Eq. (A11) contain all the kinematical dependence on the four decay angles, and can be expressed for any isobar pairing. The pairing $p\pi^+$-π^- happens to give the simplest expression because we chose the Euler angles to obtain $\hat{\mathbf{z}}'$ along the direction $\hat{\mathbf{p}}_{p\pi^+}$. Note that for $p\pi^+$-π^- or $p\pi^-$-π^+ pairings, $S=j$ in the list of attributes, (A12); for p-$\pi^-\pi^+$ isobar pairings $S=j\pm\frac{1}{2}$.

For completeness, we give the general form of F^{λ_p} for the three possible isobar pairings (our conventions for the D functions are the same as Berman and Jacob):[57]

$$\begin{aligned}
&F^{\lambda_p}(N_i\to(p\pi^+-\pi^-))\\
&\quad=\sum_{\mu}D^{*J}_{\lambda_i\mu}(\Phi,\Theta,\phi)d^j_{\mu\lambda_p}(\theta)\\
&\qquad\times\langle j\mu L\,0\,|\,J\mu\rangle g^{j,l}_{\lambda_p}\left[\frac{(2L+1)(2j+1)}{2}\right]^{1/2},
\end{aligned} \tag{A13}$$

$$\begin{aligned}
&F^{\lambda_p}(N_i\to(p\pi^--\pi^+))\\
&\quad=\sum_{\mu,\mu'}D^{*J}_{\lambda_i\mu}(\Phi,\Theta,\phi)D^{*J}_{\mu\mu'}(0,\tilde{\Theta},0)\\
&\qquad\times\sum_{\lambda'_p}d^j_{\mu'\lambda'_p}(\tilde{\theta})d^{1/2}_{\lambda'_p\lambda_p}(\chi)\times\langle j\mu' L\,0\,|\,J\mu'\rangle g^{j,l}_{\lambda'_p}\\
&\qquad\times\left[\frac{(2L+1)(2j+1)}{2}\right]^{1/2},
\end{aligned} \tag{A14}$$

$$\begin{aligned}
&F^{\lambda_p}(N_i\to(p-\pi^-\pi^+))\\
&\quad=\sum_{\mu,\mu'}D^{*J}_{\lambda_i\mu}(\Phi,\Theta,\phi)D^{*J}_{\mu\mu'}(0,\tilde{\Theta},0)\\
&\qquad\times\sum_{\lambda'_p}d^j_{\mu'-\lambda'_p0}(\tilde{\theta})d^{1/2}_{\lambda'_p\lambda_p}(\chi)\langle S\mu L\,0\,|\,J\mu\rangle\\
&\qquad\times\langle\tfrac{1}{2}\lambda'_p j\mu'-\lambda'_p\,|\,S\mu\rangle[(2L+1)(2j+1)]^{1/2}.
\end{aligned} \tag{A15}$$

The factors $[(2L+1)(2j+1)]$ are inserted to obtain a common normalization for all waves i, e.g.,

$$\frac{1}{(4\pi)^2}\int\int d\Omega\,d\omega\,|F^{\lambda_p}(i)|^2=\tfrac{1}{2}\ . \tag{A16}$$

[Here $\Omega=(\Theta,\Phi)$, $\omega=(\theta,\phi)$.] Note that the dependence on the three Euler angles, which describe the overall orientation of the three-body plane, is common to all isobars; in particular, the Φ dependence is characterized only by the production helicity λ_i. For given $M_{p\pi^+\pi^-}$, two variables, which can be taken to be $M_{p\pi^+}$ and θ, are needed in addition to the Euler angles to specify the three-body Dalitz plot. For the $p\pi^+$-π^- pairing, Eq. (A13), $F^{\lambda_p}(i)$ does not depend explicitly on $M_{p\pi^+}$, only on θ; normally one would insert an isobar Breit-Wigner function, $B(M_{p\pi^+})$, into the production amplitude to complete the description. The angles $\tilde{\Theta}$, $\tilde{\theta}$, and χ in Eqs. (A14) and (A15) are rotations in the three-body plane (about $\hat{\mathbf{y}}'$) which depend explicitly on $M_{p\pi^+}$ and θ. We summarize these angles in terms of the corresponding rotations; first for $p\pi^-$-π^+ isobars,

$\tilde{\Theta}$ takes $\hat{\mathbf{p}}_{p\pi^+}\rightarrow\hat{\mathbf{p}}_{p\pi^-}$ in $(p\pi^+\pi^-)$ c.m. ,

$\tilde{\theta}$ takes $-\hat{\mathbf{p}}_{\pi^+}\rightarrow-\hat{\mathbf{p}}_{\pi^-}$ in $(p\pi^-)$ c.m. ,

χ takes $-\hat{\mathbf{p}}_{\pi^-}\rightarrow-\hat{\mathbf{p}}_{\pi^+}$ in p c.m.

For the p-$\pi^-\pi^+$ isobars, we adopt the leading-proton convention, and

$\tilde{\Theta}$ takes $\hat{\mathbf{p}}_{p\pi^+}\rightarrow\hat{\mathbf{p}}_{p}$ in $(p\pi^+\pi^-)$ c.m. ,

$\tilde{\theta}$ takes $\hat{\mathbf{p}}_{p}\rightarrow\hat{\mathbf{p}}_{\pi^-}$ in $(\pi^-\pi^+)$ c.m. ,

χ takes $-\hat{\mathbf{p}}_{\pi^+\pi^-}\rightarrow-\hat{\mathbf{p}}_{\pi^+}$ in p c.m.

The Stapp rotations χ restore the final proton helicity λ_p to a common axis for all isobars (given by $-\hat{\mathbf{p}}_{\pi^+}$ in the proton rest frame); having a common reference frame for λ_p is, of course, crucial for calculating interferences. The factors $g^{jl}_{\lambda_p}$ in Eqs. (A13) and (A14) are required to satisfy parity conservation in the $(p\pi^\pm)\rightarrow p\pi^\pm$ isobar decays. We take

$$g^{jl}_{1/2}=+1\ , \tag{A17}$$

$$g^{jl}_{-1/2}=(-1)^{l+j-1/2}\ . \tag{A18}$$

($g^{jl}_{\lambda_p}$ is proportional to $\langle\frac{1}{2}\lambda_p l0\,|\,j\lambda_p\rangle$.)

Thus, all of the isobar contributions factorize into an explicit dependence on the Euler angles, and a generally more complicated dependence on $M_{p\pi^+}$ and θ. The expressions Eqs. (A14) and (A15) can be cast into the same explicit form as (A13), with a sum over possible $(p\pi^+)$ isobars, the coefficients in the sum depending explicitly on $M_{p\pi^+}$. For example, including a Breit-Wigner function to describe the $(p\pi^-)\rightarrow p\pi^-$ isobar decay, we can rewrite (A14) quite generally as

$$B_i(M_{p\pi^-})F^{\lambda_p}(N_i\rightarrow p\pi^-\pi^+)=\sum_{\mu}D^{*}_{\lambda_i\mu}(\Phi,\Theta,\phi)\left[\sum_{L',j',l'}C^{j'l'}(M_{p\pi^+})d^{j'}_{\mu\lambda_p}(\theta)\langle j'\mu L0\,|\,J\mu\rangle g^{j'l'}_{\lambda_p}\left[\frac{(2L'+1)(2j'+1)}{2}\right]^{1/2}\right], \tag{A19}$$

where $C^{j'l'}(M_{p\pi^+})$ is computed by equating the right-hand sides (RHS's) of Eqs. (A14) and (A19), and L',j',l' include all $p\pi^+$-π^- waves consistent with the J^P of isobar N_i. Thus, the RHS of Eq. (A19) is just a sum over $p\pi^+$-π^- isobars, each having the angular dependence of Eq. (A14), and mass dependence given by $C^{j'l'}(M_{p\pi^+})$. Note that the kinematical dependence of the Breit-Wigner functions $B(M)$ must be consistent with the expression used for the differential phase space, e.g., $dM_{p\pi^+\pi^-}dM_{p\pi^+}dt\,d\Omega\,d\omega$.

In the remaining discussion, we will consider only isobars of the type $p\pi^+$-π^-, for simplicity. Parity conservation in the production amplitudes leads to

$$A^{\lambda_N\lambda_b}_{\lambda_r\lambda_t}=(-1)^{\Sigma+\lambda_b+\lambda_N-\lambda_t-\lambda_r}\eta_N A^{-\lambda_N-\lambda_b}_{-\lambda_r-\lambda_t}\ , \tag{A20}$$

where $\Sigma=\sum S_i=\frac{3}{2}+J$ is the sum over particle spins, and $\eta_N=(-1)^{L+l}$ is the intrinsic parity of the N system. Thus only half of the amplitudes are independent. It is convenient for physics purposes to recast these in terms of definite-naturality amplitudes N (for natural-parity exchange, $\zeta=+1$) and U (for unnatural-parity exchange, $\zeta=-1$):

$$N^{\lambda_N\lambda_b}_{++}=N^{\lambda_N\lambda_b}_{--}=A^{\lambda_N\lambda_b}_{++}+A^{\lambda_N\lambda_b}_{--}\ , \tag{A21}$$

$$N^{\lambda_N\lambda_b}_{-+}=-N^{\lambda_N\lambda_b}_{+-}=A^{\lambda_N\lambda_b}_{-+}-A^{\lambda_N\lambda_b}_{+-}\ , \tag{A22}$$

$$U^{\lambda_N\lambda_b}_{++}=-U^{\lambda_N\lambda_b}_{--}=A^{\lambda_N\lambda_b}_{++}-A^{\lambda_N\lambda_b}_{--}\ , \tag{A23}$$

$$U^{\lambda_N\lambda_b}_{-+}=U^{\lambda_N\lambda_b}_{+-}=A^{\lambda_N\lambda_b}_{-+}+A^{\lambda_N\lambda_b}_{+-}\ , \tag{A24}$$

where $++$ denotes $(\lambda_r,\lambda_t)=(+\frac{1}{2},+\frac{1}{2})$, etc. Because the observables are averaged over target and recoil helicities, there are no interferences between the four independent amplitudes N_{++}, N_{-+}, U_{++}, and U_{-+}. Equivalently, using Eq. (A20), we can write

$$N^{\lambda_N\lambda_b}_{\lambda_r\lambda_t}=[A^{\lambda_N\lambda_b}_{\lambda_r\lambda_t}+(-1)^{\Sigma+\lambda_N-\lambda_b}\eta_N A^{-\lambda_N-\lambda_b}_{\lambda_r\lambda_t}]\ , \tag{A25}$$

$$U^{\lambda_N\lambda_b}_{\lambda_r\lambda_t}=[A^{\lambda_N\lambda_b}_{\lambda_r\lambda_t}-(-1)^{\Sigma+\lambda_N-\lambda_b}\eta_N A^{-\lambda_N-\lambda_b}_{\lambda_r\lambda_t}]\ . \tag{A26}$$

The observables are expressed as

$$\sigma(\Phi,\Theta,\phi,\theta)=\sum_{\substack{\lambda_r,\lambda_t\\ \lambda_p,\lambda_b,\lambda_b'}}\sum_{\lambda_i\lambda_i'}[A^{\lambda_i\lambda_b^{*}}_{\lambda_r\lambda_t}(i)A^{\lambda_i'\lambda_b'}_{\lambda_r\lambda_t}(i')]\times[F^{\lambda_p}(i)^{*}F^{\lambda_p}(i')]\rho^{b}_{\lambda_b\lambda_b'}\ , \tag{A27}$$

where

$$\rho^{b}=\tfrac{1}{2}(1+P_b\sigma) \tag{A28}$$

is the beam density matrix. If we substitute N,U amplitudes into Eq. (A27) and carry out the spin sum, we obtain the desired expansion for the polarized observables. We choose a convenient overall normalization [the relative normalization of the individual waves is common, due to Eq. (A16)] such that

$$\int\int d\Omega\, d\omega \frac{d^4\sigma}{d\Omega\, d\omega} = (4\pi)^2 \sum_{(i)} [\,|N_{++}^{\lambda_i 1/2}(i)| + |N_{-+}^{\lambda_i 1/2}(i)|^2 + |U_{++}^{\lambda_i 1/2}(i)|^2 + |U_{-+}^{\lambda_i 1/2}(i)|^2\,] \,. \tag{A29}$$

Because of parity conservation, only $\lambda_b = \frac{1}{2}$ amplitudes need to be retained in any observables, and all observables take essentially the same form for N_{++}-, N_{-+}-, U_{++}-, and U_{-+}-type waves. Specifically, we can expand Eq. (A27) in the form

$$\begin{aligned}\frac{d^2\sigma}{d\Omega\, d\omega} = &\sum_{i,i'} \mathrm{Re}[N_{++}^*(i)N_{++}(i')]\mathrm{Re}[F^{+*}(i)F^{+}(i')+F^{-*}(i)F^{-}(i')] \\ &-P_z \sum_{i,i'} \mathrm{Im}[N_{++}^*(i)N_{++}(i')]\mathrm{Im}[F^{+*}(i)F^{+}(i')+F^{-*}(i)F^{-}(i')] \\ &+\zeta P_y \sum_{i,i'} \mathrm{Im}[N_{++}^*(i)N_{++}(i')]\mathrm{Re}[2F^{+}(i)F^{-}(i')] - \zeta P_x \sum_{i,i'} \mathrm{Im}[N_{++}^*(i)N_{++}(i')]\mathrm{Im}[2F^{+}(i)F^{-}(i')] \,.\end{aligned} \tag{A30}$$

With formally identical contributions from N_{-+}, U_{++}, U_{-+}, we have included the helicity, λ_i, with the overall index i, since $\lambda_b = +\frac{1}{2}$ is now redundant. Note the factor ζ ($+1$ for N amplitudes, -1 for U amplitudes) which appears in the P_x,P_y observables; it arises because of the sign difference of the (λ_N, λ_b) and $(-\lambda_N, -\lambda_b)$ contributes to N and U amplitudes in Eqs. (A25) and (A26). In principle, if we knew which partial waves were present, we could use the comparison of longitudinal and transverse polarization to separate the naturality contributions.

Finally, the products, $F^{\lambda_p}(i)F^{\lambda'_p}(i')$, appearing in Eq. (A30) involve products of d functions [cf. Eq. (A13)], and these can be expanded using closure relations to obtain the general form for the observables which we have used. Schematically, we can write

$$F^{+*}(i)F^{+}(i')+F^{-*}(i)F^{-}(i') = \sum_{l,L,m,n} e^{im\Phi+n\phi} d^l_{n0}(\theta) d^L_{mn}(\Theta) \times C_{Llmn} \tag{A31}$$

for the unpolarized and P_z terms, and

$$2F^{+}(i)F^{-}(i') = \sum_{l,L,m'n'} e^{im'\Phi+n'\phi} d^l_{n'0}(\theta) d^L_{m'n'}(\Theta) \widetilde{C}'_{Llm'n'} \tag{A32}$$

for the P_x,P_y observables. In these expansions

$$\begin{aligned} m &= \lambda_i - \lambda_{i'} \,, \\ m' &= \lambda_i + \lambda_{i'} \,, \\ n &= \mu - \mu' \,, \\ n' &= \mu + \mu' \,, \\ l &\le j + j' \,, \\ L &\le J + J' \,, \end{aligned} \tag{A33}$$

where μ, μ', λ_i, λ'_i, etc., are as given in Eq. (A13), and the C's are calculable from the closure relations. Note that λ_i,λ'_i are the production helicities for N_i,N'_i, and μ,μ' are the $(p\pi^+)$ subsystem helicities measured along $\tilde{z}'$, as per Eq. (A13). Since only $\lambda_B = +\frac{1}{2}$ amplitudes are used in Eq. (A30), $\lambda_i = \lambda'_i = +\frac{1}{2}$ is the condition for helicity conservation. Thus, $m=0$ is required for unpolarized or P_z terms, $m=1$ for P_x, P_y terms, if helicity is conserved. Furthermore, for each N_i,N'_i contribution, the sum over μ,μ' leads to simple relationships between $+n$ and $-n$ terms given by factors ± 1.

Finally, using

$$P_x = P_\perp \sin\Psi, \quad P_z = P_\perp \cos\Psi \,, \tag{A34}$$

we obtain the expansion for the $P_\perp$ observables of Eq. (11).

*Present address: University of Wisconsin, Madison, WI 53706.
†Present address: University of Arizona, Tucson, AZ 85281.
‡Present address: AT&T Information Systems, Denver, CO 80234.

[1]J. Biel *et al.*, Phys. Rev. D **18**, 3079 (1978) ($np \to p\pi^- p$).
[2]J. Biel *et al.*, Phys. Rev. Lett. **36**, 507 (1976) ($np \to p\pi^- p$).
[3]J. Biel *et al.*, Phys. Lett. **65B**, 291 (1976) ($np \to p\pi^- p$).
[4]G. B. Chadwick *et al.*, Phys. Rev. D **17**, 1713 (1978) ($\pi^\pm p \to \pi^\pm N\pi, \pi^\pm p \to \pi^\pm p\pi^+\pi^-$).
[5]H. Grässler *et al.*, Nucl. Phys. **B95**, 1 (1975) ($\pi^\pm p \to \pi^\pm N\pi$).
[6]G. Otter *et al.*, Nucl. Phys. **B130**, 349 (1977) ($\pi^\pm p \to \pi^\pm N\pi$).
[7]G. Goggi *et al.*, Nucl. Phys. **B161**, 14 (1979) ($pp \to p\pi^+\pi^- p$, $pn \to p\pi^- p$).
[8]H. deKerret *et al.*, Phys. Lett. **63B**, 477 (1976); **63B**, 483 (1976) ($pp \to pn\pi^+$).
[9]M. Derrick, B. Musgrave, P. Schreiner, and H. Yuta, Phys. Rev. D **9**, 1215 (1974) ($pp \to p\pi^+\pi^- p$).
[10]J. G. Rushbrooke *et al.*, Phys. Rev. D **4**, 3273 (1971)

($pp \to p\pi^+\pi^- p$).
[11]G. Kayas *et al.*, Nucl. Phys. **B5**, 169 (1968) ($pp \to p\pi^+\pi^- p$).
[12]J. LeGuyader *et al.*, Nucl. Phys. **B35**, 573 (1971) ($pp \to p\pi^+\pi^- p$).
[13]E. Colton, P. E. Schlein, E. Gellert, and G. A. Smith, Phys. Rev. D **3**, 1063 (1971); **6**, 95 (1972) ($pp \to p\pi^+\pi^- p$).
[14]G. Yekutieli *et al.*, Nucl. Phys. **B18**, 301 (1970) ($pp \to p\pi^+\pi^- p$).
[15]R. Webb *et al.*, Phys. Lett. **55B**, 331 (1975) ($pp \to p\pi^+\pi^- p$).
[16]J. W. Lamsa *et al.*, Nucl. Phys. **B37**, 364 (1972) ($\pi^\pm p \to \pi^\pm p\pi^+\pi^-$).
[17]Yu. N. Antipov *et al.*, Nucl. Phys. **B99**, 189 (1975) ($\bar{p}p \to \bar{p}\pi^+\pi^- p$).
[18]K. Boesebeck *et al.*, Nucl. Phys. **B33**, 445 (1971) ($\pi^\pm p \to \pi^\pm p\pi^+\pi^-, K^- p \to K^- p\pi^+\pi^-$).
[19]J. V. Beaupré *et al.*, Phys. Lett. **41B**, 393 (1972) ($\pi^\pm p \to \pi^\pm p\pi^+\pi^-$).
[20]P. Bosetti *et al.*, Nucl. Phys. **B103**, 189 (1976) ($\pi^\pm p \to \pi^\pm p\pi^+\pi^-$).
[21]V. Blobel *et al.*, Nucl. Phys. **B97**, 201 (1975) ($pp \to p\pi^+\pi^- p$).
[22]U. Idschok *et al.*, Nuovo Cimento **48A**, 395 (1978) ($pp \to p\pi^+\pi^- p$).
[23]T. C. Bacon *et al.*, Nuovo Cimento **42A**, 431 (1977) ($K^- p \to K^- p\pi^+\pi^-, \pi^\pm p \to \pi^+ p\pi^+\pi^-$).
[24]P. M. Heinen *et al.*, Nucl. Phys. **B122**, 443 (1977) ($K^- p \to K^- p\pi^+\pi^-$).
[25]J. N. Carney *et al.*, Nucl. Phys. **B110**, 248 (1976) ($K^+ p \to K^+ p\pi^+\pi^-$).
[26]G. Otter *et al.*, Nucl. Phys. **B139**, 365 (1978) ($K^- p \to K^- p\pi^+\pi^-$).
[27]R. T. Deck, Phys. Rev. Lett. **13**, 169 (1964).
[28]E. L. Berger, Phys. Rev. **179**, 1567 (1969); in *Three Particle Phase Shift Analysis and Meson Resonances Production, Proceedings of the Daresbury Study Weekend, 1975,* edited by J. B. Dainton and A. J. G. Hey (Science Research Council, Daresbury, England, 1975); Argonne Report No. ANL-HEP-PR-75-32, 1975 (unpublished); Phys. Rev. D **11**, 3214 (1975).
[29]R. T. Cutler and H. W. Wyld, Phys. Rev. D **12**, 1952 (1975).
[30]R. T. Cutler and E. L. Berger, Phys. Rev. D **15**, 1903 (1977).
[31]E. L. Berger and P. Pirilä, Phys. Lett. **59B**, 361 (1975).
[32]G. Cohen-Tannoudji, A. Santoro, and M. Souza, Nucl. Phys. **B125**, 445 (1977).
[33]R. S. Longacre and J. Dolbeau, Nucl. Phys. **B122**, 493 (1977).
[34]D. Herndon *et al.*, Phys. Rev. D **11**, 3183 (1975).
[35]R. Longacre *et al.*, Phys. Lett. **55B**, 415 (1978); Phys. Rev. D **17**, 1795 (1978).
[36]D. M. Manley, R. A. Arndt, Y. Goradia, and V. L. Teplitz, Phys. Rev. D **30**, 904 (1984).
[37]D. E. Novoseller, Nucl. Phys. **B137**, 445 (1978); **B137**, 509 (1978).
[38]R. Koniuk and N. Isgur, Phys. Rev. D **21**, 1868 (1980); N. Isgur and G. Karl, *ibid.* **18**, 4187 (1978).
[39]M. W. Arenton *et al.*, Phys. Rev. D **25**, 22 (1982).
[40]M. W. Arenton *et al.*, Phys. Rev. D **25**, 2241 (1982).
[41]M. W. Arenton *et al.*, Phys. Rev. D **28**, 657 (1983).
[42]S. Kooijman *et al.*, Phys. Rev. Lett. **45**, 316 (1980).
[43]I. Ambats *et al.*, Nucl. Instrum. Methods **174**, 427 (1980).
[44]H. Hinterberger *et al.*, Rev. Sci. Instrum. **41**, 413 (1970).
[45]G. C. Chew and F. E. Low, Phys. Rev. **113**, 1640 (1959); E. Ferrari and F. Selleri, Nuovo Cimento Suppl. **24**, 453 (1962).
[46]N. Sakai and J. N. J. White, Nucl. Phys. **B59**, 511 (1973); G. Kane, Acta. Phys. Pol. **B3**, 845 (1972); M. Jacob and R. Stroynowski, Nucl. Phys. **B82**, 189 (1974); S. Humble, *ibid.* **B76**, 137 (1974); **B86**, 285 (1975).
[47]R. Diebold, in *High Energy Physics with Polarized Beams and Targets,* Proceedings of the Argonne Symposium 1976, edited by M. L. Marshak (AIP Conf. Proc. No. 35) (AIP, New York, 1976); A. B. Wicklund *et al.* (unpublished).
[48]R. M. Edelstein *et al.*, Phys. Rev. D **5**, 1023 (1972).
[49]J. V. Allaby *et al.*, Nucl. Phys. **B52**, 316 (1973).
[50]Particle Data Group, Rev. Mod. Phys. **56**, S1 (1984).
[51]The pion-exchange amplitudes can, in principle, be calibrated using the reaction $pp \to p\pi^+ n$, as in Ref. 47; the amplitudes for $\pi^0 p \to \pi^+\pi^- p$ can be deduced from the formation studies of Refs. 34–36. Using formation cross sections and isobar couplings of Ref. 36, we estimate $\sim 5\%$ π^0-exchange contribution in the $N(1700)$ region.
[52]A. B. Wicklund, in *High Energy Physics with Polarized Beams and Targets* (Ref. 47).
[53]Particle Data Group, Rev. Mod. Phys. **52**, S188ff (1980).
[54]G. Ascoli, L. M. Jones, B. Weinstein, and H. W. Wyld, Phys. Rev. D **8**, 3894 (1973).
[55]The relative phase between an $N(1520)\pi^+$ wave and a $\Delta^{++}\pi^-$ wave can be expressed as $\Phi_R + \phi_N - \Phi_\Delta - \phi_\Delta$; here ϕ_N, ϕ_Δ are the N^* and Δ Breit-Wigner phases, Φ_R and Φ_Δ are the respective production phases. The quantity $\phi_N - \phi_\Delta$ depends on the average value of $M_{p\pi^+}$ at which the $N(1520)$ reflection occurs; because this overlap position increases with $M_{p\pi^+\pi^-}$, the quantity $\phi_N - \phi_\Delta$ decreases with $M_{p\pi^+\pi^-}$, mirroring the Δ^{++} phase. Thus any resonancelike advance in $\Phi_R - \Phi_\Delta$ would tend to be canceled by the behavior of $\phi_N - \phi_\Delta$.
[56]D. J. Herndon, P. Söding, and R. J. Cashmore, Phys. Rev. D **11**, 3165 (1975).
[57]S. M. Berman and M. Jacob, Phys. Rev. **139**, 1023 (1965).